Topology in
dynamical Lattice QCD simulations

DISSERTATION

zur Erlangung des Doktorgrades
der Naturwissenschaften (Dr. rer. nat.)
der Fakultät für Physik
der Universität Regensburg

vorgelegt von

Florian Gruber

aus Straubing

August 2012

Promotionsgesuch eingereicht am 20. August 2012

Die Arbeit wurde angeleitet von: Prof. Dr. A. Schäfer

Prüfungsausschuss: Vorsitzender: Prof. Dr. S. Ganichev
                      1. Gutachter: Prof. Dr. A. Schäfer
                      2. Gutachter: Prof. Dr. T. Wettig
                      weiterer Prüfer: Prof. Dr. I. Morgenstern

Contents

Contents

List of Publications

Peer-reviewed journals

[1] Falk Bruckmann, Nigel Cundy, Florian Gruber, Thomas Lippert and Andreas Schäfer. Topology of dynamical lattice configurations including results from dynamical overlap fermions. *Phys. Lett.*, B707:278–285, 2012.

[2] Falk Bruckmann, Florian Gruber and Andreas Schäfer. Filtered topological structure of the QCD vacuum: Effects of dynamical quarks. *Phys. Lett.*, B687:92–97, 2010.

[3] Falk Bruckmann, Florian Gruber, Karl Jansen, Marina Marinkovic, Carsten Urbach and Marc Wagner. Comparing topological charge definitions using topology fixing actions. *Eur. Phys. J.*, A43:303–311, 2010.

Conference proceedings

[4] Falk Bruckmann, Nigel Cundy, Florian Gruber, Thomas Lippert and Andreas Schäfer. Topology of dynamical lattice configurations including results from dynamical overlap fermions. *PoS*, LATTICE2011:258, 2011.

[5] Falk Bruckmann, Florian Gruber and Andreas Schäfer. Comparing the vacuum structure of quenched and dynamical configurations. *PoS*, LAT2009:224, 2009.

[6] Falk Bruckmann, Florian Gruber, Christian. B. Lang, Markus Limmer, Thilo Maurer, Andreas Schäfer and Stefan Solbrig. Comparison of filtering methods in SU(3) lattice gauge theory. *PoS*, Confinement8:045, 2009.

Introduction

On July 4, 2012, the CMS [7] and ATLAS [8, 9] experiments at the Large Hadron Collider announced independently that they had found a previously unknown elementary particle with a mass around 125 GeV, that is over a hundred times heavier than the hydrogen atom. From the decay products one knows that it has to be a boson and, hence, serves as a candidate for the long sought-after *Higgs boson*. Before a final result can be presented more data has to be gathered and analyzed, but both experiments are confident to present the final answer soon.

The Higgs boson is the last particle in the Standard Model of particle physics that has not been observed experimentally yet. It plays an important role in the electroweak interaction where it explains the masses of Z and W bosons through the so-called *Higgs mechanism* [10, 11, 12, 13]. Furthermore, it gives rise to the masses of leptons like quarks and electrons and, thus, it is often said that the Higgs boson is the "origin of mass".

This statement is, however, not entirely correct as almost 99 percent of the observed mass is due to the strong interaction called *Quantum Chromodynamics* (QCD) which governs the dynamics of quarks and gluons — the constituents of *hadrons* like the proton and the nucleon. The proton, for example, consists of two up and one down quarks with a total mass of around 10 MeV (gluons are massless), but the experimentally measured mass is 938 MeV [14].

QCD is a highly nonlinear theory and it turns out that the coupling of quarks and gluons depends on the energies of the interacting particles. For very high momentum transfers one has a weakly coupled theory and QCD can be treated perturbatively (in an expansion in terms of the coupling constant). This property is also called *asymptotic freedom* and its discovery awarded the Nobel prize in physics 2004 (Gross, Wilczek and Politzer).

The second fundamental property of QCD is *confinement*, which describes the experimental observation that there are no free color-charged (strongly interacting) particles in nature. They are all bound in color-neutral hadrons. There is, however, no rigorous mathematical proof that QCD is confining. This is related to the fact that the coupling is strong at low energies and perturbation theory is not applicable. Nonperturbative methods are needed instead.

Lattice QCD is such an nonperturbative approach. Thereby, space-time is replaced by a Euclidean hypercubic lattice. The quark fields reside on the lattice sites and the gluons are the links between the sites. Observables are then formulated on this lattice and their quantum mechanical expectation values can be evaluated. The great advantage of this approach is that it can be systematically improved by reducing the lattice spacing,

and, with a sufficient number of lattice spacings, it is possible to extrapolate the results to the continuum limit, i.e. to a vanishing lattice spacing. Lattice QCD has been applied very successfully. It provides us with numerical evidence for confinement and many other results, such as the mass spectrum of light hadron, which is in excellent agreement with experiment.

The main focus of this thesis are topological structures in the QCD vacuum — the nonperturbative ground state of QCD — as seen in Lattice QCD simulations. The topology is in this context not only an abstract mathematical concept. There is a deep relation to the underlying physics and confinement. Furthermore, it is strongly tied to chiral symmetry, one of the fundamental symmetries of the QCD Lagrangian. In particular, the spontaneous breaking of chiral symmetry can be traced back to the topology of the gauge fields. There is, however, a fundamental problem on a lattice: Any gauge field configuration can be continuously transformed to a trivial configuration and one would not have distinct topological structures. Nevertheless, there are remnants of the continuum topology if the lattice spacing is small enough and one of the main tasks is to identify these structures without introducing lattice artifacts or method-dependent ambiguities.

This thesis is structured as follows: In the first three chapters we introduce all concepts which are necessary to understand the relation of topology, chiral symmetry and the QCD vacuum. We start with a chapter on the foundations of QCD. Therein, we focus on the path integral formalism and chiral symmetry, which is one of the fundamental symmetries of QCD, and, furthermore, give a brief introduction to the topology of gauge fields. Then we show in the second chapter how QCD is formulated on a space-time lattice focusing, amongst other things, on the realization of chiral symmetry for different discretizations of the fermion action. This is followed by a chapter on topology in Lattice QCD, where basic definitions are presented and filtering methods to extract the relevant topological excitations from Lattice QCD configurations are introduced.

The main part is divided according to the various projects within this thesis. In Chapter 4 we compare different filtering methods and show how these could be matched to reduce ambiguities from a single filter. A cluster analysis of the topological charge density for this matched filtering has been carried out in Chapter 5. The latter two chapters are based on our publications Ref. [2] and Ref. [6]. In Chapter 6 we present the topological structure in lattice simulations with exact chiral symmetry. The configurations from this project are used in Chapter 7, where we compare various lattice discretizations of the fermion action. As chiral symmetry is realized quite differently in these simulations, we use our exactly chiral configurations as a benchmark. The outcome of this project has been published in Ref. [1] and Ref. [4]. In the last chapter we investigate the properties of the QCD vacuum under extreme conditions. To this end, we employ a very strong external magnetic field and measure its impact on the vacuum structure at zero and finite temperature. Finally, we give our conclusions.

1

Foundations of QCD

The following chapter gives a short introduction to the principles of *Quantum Chromodynamics* (QCD). The main focus is on the basic formulas and concepts which are necessary to understand the path integral formulation and the connection between chiral symmetry and the topology of gauge fields. The presented material has been chosen, such that all necessary quantities are defined. For a more pedagogical introduction, we refer to standard textbooks like Refs. [15, 16, 17].

Throughout this thesis the Euclidean formulation is used (see Appendix A.1). Furthermore, a summation over repeated indices is assumed if not explicitly written.

1.1. The QCD action

Quantum Chromodynamics describes the interaction of *quarks* and *gluons*. Quarks are massive fermions, which can be represented by Dirac spinors

$$\psi_f^{(\alpha,a)}(x) \qquad \text{and} \qquad \bar{\psi}_f^{(\alpha,a)}(x), \tag{1.1}$$

where $\bar{\psi}$ denotes the corresponding antiparticle to ψ. $f \in \{u, d, s, c, b, t\}$ is the flavor index, $\alpha = 1, 2, 3, 4$ is the spinor or Dirac index and $a = 1, \ldots, N_c (= 3$ for QCD) is the color index. Accordingly, each quark flavor has $4N_c$ field components at each space-time point x.

The quark flavors differ in mass and have electric charges $q_f = 2/3$ or $q_f = -1/3$ ($q_u, q_c, q_t = 2/3$ and $q_d, q_s, q_b = -1/3$). One finds in nature that there are two light flavors (up and down) and four heavier flavors with a very distinct hierarchy of masses. The mass difference of the two light quarks is very small compared to the typical hadronic scale. Thus, one can assume that they are mass-degenerate. For most calculations it is sufficient to take only the contributions of the two light flavors (and the

heavier strange quark) into account. In this case one speaks of $N_f = 2(+1)$ results. In many cases it is further justified to neglect electromagnetic effects, because the electromagnetic coupling is much smaller than the strong coupling and so there is an exact iso-spin symmetry between up and down quarks.

The interaction between quarks is mediated by massless, color-charged boson fields called gluons

$$\mathrm{A}_{\mu}^{ab}(x). \tag{1.2}$$

These fields carry a space-time index $\mu = 1, 2, 3, 4$ and two color indices $a, b = 1, \ldots, N_c$. For fixed μ and x they can be represented by hermitian traceless $N_c \times N_c$ matrices (This is also known as the adjoint representation). Consequently, we can express the gluon fields as a linear combination of the generators of the $\mathfrak{su}(N_c)$ Lie algebra

$$\mathrm{A}_{\mu}(x) = \sum_{a=1}^{N_c^2-1} \mathrm{A}_{\mu}^{a}(x) T^a, \tag{1.3}$$

with real-valued color components $\mathrm{A}_{\mu}^{a}(x)$. The generators obey the general commutator relation

$$[T^a, T^b] = i f^{abc} T^c, \tag{1.4}$$

where f_{abc} are the totally antisymmetric structure constants and they are normalized as

$$\mathrm{tr}\{T^a T^b\} = \frac{\delta_{ab}}{2}. \tag{1.5}$$

For $N_c = 3$ these matrices are the eight Gell-Mann matrices and for $N_c = 2$ the three Pauli matrices.

The dynamics of quarks and gluons are governed by the QCD action. This is a functional of the fields, consisting of two parts. The first one contains the quarks and their interaction with gluons and the second describes the dynamics of gluons only:

$$S_{\mathrm{QCD}}[\psi, \bar{\psi}, \mathrm{A}] = S_F[\psi, \bar{\psi}\,\mathrm{A}] + S_G[\mathrm{A}]. \tag{1.6}$$

The fermion part for a single flavor and mass m_f reads in a compact vector notation (color and spinor indices are suppressed) as follows

$$S_F[\psi, \bar{\psi}, \mathrm{A}] = \int d^4x\, \bar{\psi}_f(x)\big(\gamma^{\mu} D_{\mu} + m_f\big)\psi_f(x), \tag{1.7}$$

where γ_{μ} are the (Euclidean) γ-matrices (see A.2) and

$$D_{\mu} = \partial_{\mu} + i\,\mathrm{A}_{\mu}(x) \tag{1.8}$$

is the *covariant derivative*. Eq. (1.7) looks formally like the fermion part of the QED action, but it has additional color degrees of freedom in the fields A and ψ. Varying the above equation with respect to $\bar{\psi}$ leads to the QCD Dirac equation

$$(\gamma^{\mu} D_{\mu} + m_f)\psi_f(x) = 0. \tag{1.9}$$

The gauge principle of QED is generalized to QCD by requiring the action to be invariant under local rotations in color space. The fermions transform as

$$\psi(x) \rightarrow \psi'(x) = g(x)\psi(x) \qquad \text{and} \qquad \bar{\psi}(x) \rightarrow \bar{\psi}'(x) = \bar{\psi}(x)g(x)^{\dagger}, \tag{1.10}$$

where $g(x)$ is a unitary, hermitian $N_c \times N_c$ matrix with unit determinant $\det g(x) = 1$. Hence, $g(x)$ is an element of the special unitary group $SU(N_c)$. The gauge-invariance of the action S_F implies that the gauge fields transform in analogy to QED as

$$\mathrm{A}_{\mu}(x) \rightarrow \mathrm{A}'_{\mu}(x) = g(x)\,\mathrm{A}_{\mu}(x)g(x)^{\dagger} + i\big(\partial_{\mu}g(x)\big)g(x)^{\dagger}. \tag{1.11}$$

The gluonic part of the action is easily derived as a generalization of the QED gauge action. Correspondingly, the field strength tensor is defined as the commutator of two covariant derivatives

$$F_{\mu\nu} = \frac{1}{i}[D_{\mu}, D_{\nu}] = \partial_{\mu}\,\mathrm{A}_{\nu} - \partial_{\nu}\,\mathrm{A}_{\mu} - i[\mathrm{A}_{\mu}, \mathrm{A}_{\nu}] = \sum_a F^a_{\mu\nu}T^a. \tag{1.12}$$

The commutator term $[\mathrm{A}_{\mu}, \mathrm{A}_{\nu}]$ vanishes for QED but for $\mathfrak{su}(N_c)$-valued fields it does, in general, not. A gauge-invariant, scalar combination of the field strength tensor is needed for the action. The simplest way to achieve this is

$$S_G[\mathrm{A}] = \frac{1}{2g^2}\int d^4x \, \mathrm{tr}\left\{F_{\mu\nu}(x)F_{\mu\nu}(x)\right\} = \frac{1}{4g^2}\int d^4x \, F^a_{\mu\nu}(x)F^a_{\mu\nu}(x), \tag{1.13}$$

where the trace is taken over the color indices and g denotes the strong coupling constant. This expression formally looks like the QED photon action, but, due to the nonvanishing commutator, cubic and quartic terms in the gauge fields emerge. These terms give rise to gluon self-interactions and to the highly nonlinear nature of QCD.

1.2. Path integral formulation

So far we have only defined a classical field theory of quarks and gluons. Hence, we need a prescription to quantize this field theory. The path integral offers a very elegant way to make this transition from a classical theory to a quantum theory. (For a good introduction, see Ref. [15] or Ref. [16]).

The expectation value of a quantum mechanical operator $\hat{O}[\hat{\bar{\psi}}, \hat{\psi}, \hat{\mathrm{A}}]$, which can be any function of the field operators (quantum mechanical operators are denoted by hat), is given in the path integral formalism by (flavor, color and spinor indices suppressed):

$$\langle \hat{O}[\hat{\psi}, \hat{\bar{\psi}}, \hat{\mathrm{A}}_{\mu}]\rangle = \frac{1}{Z}\int [\mathcal{D}\,\psi][\mathcal{D}\,\bar{\psi}][\mathcal{D}\,\mathrm{A}]O[\psi, \bar{\psi}, \mathrm{A}_{\mu}]e^{iS[\psi, \bar{\psi}, \mathrm{A}_{\mu}]}, \tag{1.14}$$

where the *partition function*

$$Z = \int [\mathcal{D}\,\psi][\mathcal{D}\,\bar{\psi}][\mathcal{D}\,\mathrm{A}]e^{-S[\psi, \bar{\psi}, \mathrm{A}_{\mu}]} \tag{1.15}$$

has been introduced. The integration measure is formally defined as

$$[\mathcal{D}\,\psi] = \prod_{f,a,\alpha,x} d\psi_f^{(a,\alpha)}(x), \tag{1.16}$$

$$[\mathcal{D}\,\bar{\psi}] = \prod_{f,b,\beta,x} d\bar{\psi}_f^{(b,\beta)}(x), \tag{1.17}$$

$$[\mathcal{D}\,\mathrm{A}] = \prod_{\mu,a,x} d\,\mathrm{A}_\mu^a(x). \tag{1.18}$$

The r.h.s. of Eq. (1.14) contains only classical fields, whereas the l.h.s. is the expectation value of a quantum mechanical operator. Therefore, the path integral provides a transition to a quantum theory which enters through the integration over all possible field configurations weighted by the classical action.

The quark fields in the path integral cannot be represented by ordinary c-numbers. In order to obey Fermi statistics, one has to introduce anticommuting, Grassmann-valued fields (see Appendix A.3). It is hard do calculate with these numbers dirictly and, thus, is is better to integrate out fermionic degrees of freedom. By using the basic rules of Grassmann integration (see Appendix A.3) and the special structure of the fermion action, the so-called *fermion determinant* is obtained[1]

$$\int [\mathcal{D}\,\bar{\psi}][\mathcal{D}\,\psi] e^{-S_F[\bar{\psi},\psi]} = \int [\mathcal{D}\,\bar{\psi}][\mathcal{D}\,\psi] e^{-\bar{\psi}(\slashed{D}+m)\psi} = \mathrm{Det}(\slashed{D}+m) \tag{1.19}$$

and, therewith, the partition function reads

$$Z = \int [\mathcal{D}\,\psi][\mathcal{D}\,\bar{\psi}][\mathcal{D}\,\mathrm{A}] e^{-S[\psi,\bar{\psi},\mathrm{A}_\mu]} = \int [\mathcal{D}\,\mathrm{A}] e^{-S_G[\mathrm{A}_\mu]} \mathrm{Det}(\slashed{D}+m). \tag{1.20}$$

The common matrix identity $\log \det M = \mathrm{tr}\log M$ further yields

$$Z = \int [\mathcal{D}\,\mathrm{A}] e^{-S_{\mathrm{eff}}} \tag{1.21}$$

with the effective action

$$S_{\mathrm{eff}} = S_G[\mathrm{A}_\mu] - \mathrm{tr}\log\{\slashed{D}+m\}. \tag{1.22}$$

1.3. Chiral symmetry and the chiral anomaly

Symmetry is one of the fundamental concepts of physics. According to Noether's theorem every symmetry is connected to a conservation law and constrains the dynamics of a physical system.

It is not only the presence of a symmetry which is interesting, but also its breaking. Such broken symmetries can be found everywhere in physics from hydrodynamics to

---

[1] We write Det in order to distinguish this functional determinant from the usual determinant det for matrices.

magnetism. For QCD, in particular, the chiral symmetry and its spontaneous (and explicit) breaking is of central importance, as this effect is responsible for an overwhelming part of the hadron mass.

Before explaining chiral symmetry, we have a look at a related concept, namely helicity, which is defined for any particle with spin as the projection of the spin vector onto the momentum vector. A particle is called right-handed if this projection is positive and left-handed if it is negative. The problem of this definition is that it is not a Lorentz-invariant concept for massive particles. The helicity will flip sign after performing a transformation from the rest frame to a frame which moves faster than the particle.

Chirality, by contrast, is a Lorentz-invariant concept which uses the eigenstates of the γ_5-matrix.

$$\gamma_5 \psi = \pm \psi. \tag{1.23}$$

Both concepts coincide in the massless limit and, thus, one calls states with an eigenvalue $+1$ right-handed and with -1 left-handed.

A general Dirac spinor has left- and right-handed components which can be projected out by the projection operators

$$P_+ = P_R = \frac{1 + \gamma_5}{2} \qquad \text{and} \qquad P_- = P_L = \frac{1 - \gamma_5}{2}. \tag{1.24}$$

The quark and anti-quark fields can be decomposed due to their chirality eigenstates:

$$\psi = \begin{pmatrix} \psi_R \\ \psi_L \end{pmatrix} \qquad \text{and} \qquad \bar{\psi} = \begin{pmatrix} \bar{\psi}_R & \bar{\psi}_L \end{pmatrix}, \tag{1.25}$$

where

$$\psi_{R/L} = P_{R/L} \psi. \tag{1.26}$$

Inserting this representation into the action functional of QCD, it divides into three parts. One with only left-handed fields, one with only right-handed fields and the mass term which couples left- and right-handed fields:

$$S_{\text{QCD}}[\psi, \bar{\psi}, A] = S[\psi_L, \bar{\psi}_L, A] + S[\psi_R, \bar{\psi}_R, A] + S_{\text{mass}}[\psi, \bar{\psi}]. \tag{1.27}$$

In the absence of a mass term, transformations of the kind $R \to L$ and $L \to R$ do not alter the theory. This symmetry is called *parity* which is a special case of a global chiral rotation

$$\psi \to e^{i\gamma_5 \theta} \psi. \tag{1.28}$$

The massless QCD action is even invariant under a local (infinitesimal) chiral symmetry transformation:

$$\psi(x) \to \big(1 + i\theta(x)\gamma_5\big)\psi(x) \qquad \text{and} \qquad \bar{\psi}(x) \to \bar{\psi}(x)\big(1 + i\theta(x)\gamma_5\big) \tag{1.29}$$

for the flavor singlet and

$$\psi(x) \to \big(\mathbb{1} + i\theta^a(x)T_a\gamma_5\big)\psi(x) \qquad \text{and} \qquad \bar{\psi}(x) \to \bar{\psi}(x)\big(\mathbb{1} + i\theta^a(x)T_a\gamma_5\big) \tag{1.30}$$

for the flavor multiplet. In the latter, T_a denote the generators of flavor symmetry group $SU(N_f)$ and not the color symmetry group $SU(N_c)$. Accordingly, the action is invariant under a local $U(N_f)_L \times U(N_f)_R = SU(N_f)_L \times SU(N_f)_R \times U(1)_V \times U(1)_A$ symmetry.[2]

Mass terms break this symmetry explicitly, but there should be remnants of this symmetry which influence the observed hadron spectrum. The bare mass terms in the QCD action are small compared to the hadronic scale and thus only small effects are expected. It turns out, however, that many effects are not compatible with this small mass term. For example, the mass difference of the proton and its parity partner, the $N^\star$, is approximately $600\,\mathrm{MeV} \gg m_{u/d}$ [18]. Hence, other mechanisms are needed which prevent this symmetry of being realized in nature.

The solution to this problem is the *spontaneous breaking of chiral symmetry* (spontaneous χSB). Following the textbook of Peskin and Schroeder [16], one can qualitatively explain the spontaneous χSB in analogy to superconductivity: In a superconductor a small attractive force between electron pairs leads to the formation of Cooper-pairs which result in a nonvanishing condensate of bound electron pairs. In QCD we have a strong attractive interaction between quarks and anti-quarks. The energy cost of creating a quark anti-quark pair is small leading to a nonvanishing expectation value of those pairs. These pairs must have zero total momentum and zero angular momentum which can only be realized if a left-handed quark and right-handed anti-quark or left-handed anti-quark and right-handed quark are combined. Thus,

$$\langle 0|\bar{\psi}\psi|0\rangle = \langle 0|\bar{\psi}_R\psi_L + \bar{\psi}_L\psi_R|0\rangle \neq 0. \tag{1.31}$$

This ground state is, however, only symmetric under parity transformations and not under a general chiral transformation, and a nonvanishing expectation value mixes states with different chirality.

Therefore, the $U(3)_L \times U(3)_R$ symmetry[3] is broken to a $U(3)_{R=L}$ symmetry and, according to the Goldstone theorem, one has to have massless bosons. This role is played by pions, kaons and the η-particle, which are not massless, but much lighter than typical hadron masses. Hence, we call them pseudo-Goldstone bosons.

$U(3)$ has nine degrees of freedom and one expects nine pseudo-Goldstone bosons, but there are only eight found in nature. The ninth would-be Goldstone boson, the η', is much too heavy to be compatible with this symmetry breaking. The only possible explanation is that the theory does not possess the aforementioned $SU(3)_L \times SU(3)_R \times U(1)_V \times U(1)_A$ symmetry and one subgroup of this symmetry has to be broken in another way. It turns out that this is the $U(1)_A$ axial symmetry and the reason for the absence of this symmetry is the well-known chiral anomaly.

One talks about quantum anomalies if a symmetry of the classical action functional is not present in the corresponding quantum theory. The path integral formalism offers a simple interpretation of such anomalies: As the integrand containing the classical ac-

---

[2] $U(1)_V$ denotes the vector symmetry ($\psi_L \to e^{i\theta}\psi_L$ and $\psi_R \to e^{i\theta}\psi_R$) and $U(1)_A$ denotes the axial symmetry ($\psi_L \to e^{i\theta}\psi_L$ and $\psi_R \to e^{-i\theta}\psi_R$).

[3] At most the $N_f = 3$ lightest flavors can be taken as "massless".

tions functional will always obey the symmetries of the classical theory by construction, it can only come from the measure.

This is the gist of *Fujikawa's method* to derive the chiral anomaly [16, 19, 20, 21] (see Appendix A.4). In this elegant but elaborate calculation one carefully defines the integration measure in terms of eigenfunctions Φ_n of the Dirac operator, which leads to a nontrivial transformation

$$[\mathcal{D}\,\bar{\psi}'][\mathcal{D}\,\psi'] = \exp\left\{-2i\int d^4x\,\theta(x)\sum_n \Phi_n^\dagger(x)\gamma_5\Phi_n(x)\right\}[\mathcal{D}\,\bar{\psi}][\mathcal{D}\,\psi.] \qquad (1.32)$$

This looks almost like a unitary transformation, but it is not. It can immediately be seen for a global chiral rotation, where $\theta(x) = const.$, that the contributions of eigenvectors with nonzero eigenvalue vanish as ϕ and $\gamma_5\phi$ are orthogonal.[4] The zero modes, however, contribute with $\int d^4x\Phi_n^\dagger(x)\gamma_5\Phi_n(x) = \pm 1$ depending on the chirality of the mode. Thus, one gets

$$\int d^4x\sum_n \Phi_n^\dagger(x)\gamma_5\Phi_n(x) = n_R - n_L \equiv -\,\mathrm{index}(D), \qquad (1.33)$$

where $n_{L/R}$ counts the number of left-/right-handed zero modes which define the *index* of the Dirac operator.

For a local transformation the calculation is more tricky, as the sum over eigenstates has to be regularized in an appropriate manner (see Appendix A.4). The final result is

$$\sum_n \Phi_n^\dagger(x)\gamma_5\Phi_n(x) = -\frac{1}{16\pi^2}\,\mathrm{tr}\{F_{\mu\nu}\tilde{F}^{\mu\nu}\}, \qquad (1.34)$$

where

$$\tilde{F}_{\mu\nu} = \tfrac{1}{2}\epsilon_{\mu\nu\rho\sigma}F_{\rho\sigma}. \qquad (1.35)$$

is the *dual field strength tensor*. This equation also holds for a global chiral rotation and yields together with Eq. (1.33) a relation between the space of zero modes of the Dirac operator and the underlying gauge field:

$$\mathrm{index}(D) = n_L - n_R = \frac{1}{16\pi^2}\int d^4x\,\mathrm{tr}\{F_{\mu\nu}\tilde{F}^{\mu\nu}\} \equiv Q_{\mathrm{top}}. \qquad (1.36)$$

Accordingly, every gauge field configuration can be characterized by an integer number. Smooth deformations of the field cannot change this integer which is for that reason called topological invariant or topological charge Q_{top}. The relation between index and topological charge is the famous Atiyah-Singer index theorem [22].

In conclusion, one can interpret the chiral anomaly as an effect of the topology of the background field. Due to the anomaly we have less symmetries than the classical theory pretends to have. As a result the spontaneous chiral symmetry breaking does not prevent the η' from acquiring a large mass.

---

[4]ϕ and $\gamma_5\phi$ are eigenvectors of complex conjugated eigenvalues and, as a result, they are orthogonal.

1.4. Topology and the QCD vacuum

The Atiyah-Singer index theorem is a good example of how purely mathematical concepts enter physics. Topology, in particular, has a growing impact in many fields of physics including solid-state physics, cosmology and hydrodynamics. In this section we have a closer look on topological concepts in physics and QCD.

1.4.1. Topology in a nutshell

Topology is a branch of mathematics which deals with general properties of mathematical objects or spaces. It provides us with tools to characterize these objects and to classify them according to properties that are common or stable under continuous deformations. In this sense one can define topological equivalence classes and calls two objects topologically equivalent if there exists a continuous, invertible mapping between them. Such mappings are so-called *homeomorphisms*.

Before we discuss the situation in QCD, we start with a simpler example of a two-dimensional unit vector field in some domain D (all vectors can be represented by a phase $e^{i\alpha(x)}$). The Stokes' theorem ties the fields inside the domain to the fields on the boundary. Each possible field configurations can, then, be classified by the *winding number*:

$$\mu = \frac{1}{2\pi} \oint_{\partial D} dl \, e^{i\alpha(l)}. \tag{1.37}$$

This number counts how often the vector field is rotated when going around the boundary. Various examples, thereof, can be found in Fig. 1.1. The field has to be smooth to ensure finite action and it has to be periodic when going around the circle. (In principle, the periodicity follows also from the first condition.). Thus, trying to deform configurations with different winding number into the other fails because there will be at least one point that violates these conditions. Consequently, the winding number defines a topological equivalence class.

Topological equivalence classes of this kind play an important role in the theory of vortices, which occur in fluids, spin-glasses or magnets. The relation to Stokes' theorem enables a nice interpretation of the winding number: It counts the number
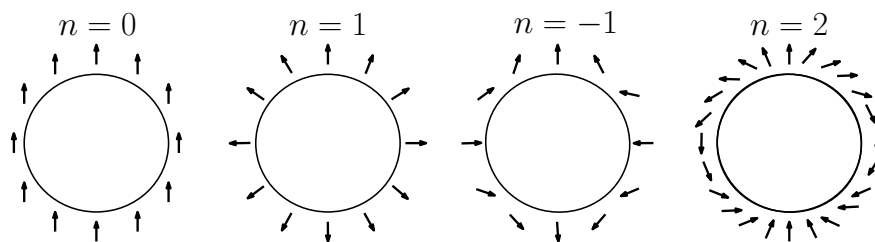

Fig. 1.1: Visualization of different winding numbers of a unit vector field at the boundary of a domain.

of field vortices inside the domain. This simple example will now be extended to a four-dimensional, non-Abelian gauge theory.

1.4.2. Instantons

In this section we introduce the prime example of a topological object in gauge theory: the instanton. Starting with a four-dimensional Euclidean Yang-Mills (or pure gauge) theory, based on the gauge group $SU(N)$, we demand that the action

$$S_{\text{YM}} = S_{\text{G}} \overset{(1.13)}{=} \frac{1}{2g^2} \int \text{tr}\{F_{\mu\nu}^2(x)\} \, d^4x \tag{1.38}$$

is finite, otherwise we do not have a physically meaningful theory. This requirement implies that the field strength has to vanish at infinity and therefore A_μ approaches a pure gauge field

$$A_\mu(x)\Big|_{|x|\to\infty} = i\big(\partial_\mu g(x)\big)g(x)^\dagger. \tag{1.39}$$

All elements at the boundary are group elements of the gauge group instead of algebra-valued fields and $A_\mu(x)$ changes smoothly around the boundary. Furthermore, one can rewrite the Yang-Mills action with the dual field strength tensor of Eq. (1.35) and gets [23, 24]:

$$S_{\text{YM}} = \frac{1}{2g^2} \int \underbrace{\frac{1}{2} \text{tr}\{\big(F_{\mu\nu}(x) \pm \tilde{F}_{\mu\nu}(x)\big)^2\}}_{\geq 0} \mp \text{tr}\{F_{\mu\nu}\tilde{F}_{\mu\nu}\}d^4x, \tag{1.40}$$

where it has been used that $F_{\mu\nu}^2 = \tilde{F}_{\mu\nu}^2$. The first term in the integrand cannot be negative due to the square and it vanishes if the gauge field is *(anti-)selfdual*

$$F_{\mu\nu} = \pm\tilde{F}_{\mu\nu}, \tag{1.41}$$

Therewith, a lower bound for the action can be derived

$$S_{\text{YM}} \geq \frac{1}{2g^2}\Big| \int \text{tr}\{F_{\mu\nu}\tilde{F}_{\mu\nu}\}d^4x\Big|, \tag{1.42}$$

which is also called *Bogomolnyi-Prasad-Sommerfeld bound*. Selfdual solutions saturate this bound and it can be shown with the aid of the Bianchi identities that the selfduality condition Eq. (1.41) is equivalent to the classical Yang-Mills equations of motion

$$D_\mu F_{\mu\nu} = 0. \tag{1.43}$$

The selfduality condition is only a first order differential equation and, thus, it is much simpler to solve than the equations of motion. Such a solution is fully nonperturbative, as $S \to \infty$ for $g \to 0$ and, hence, it serves as a starting point for studying nonperturbative phenomena.

Belavin, Polyakov, Shvarts and Tyupkin [25] found such a selfdual solution for the gauge group $SU(2)$.[5] It reads as follows:

$$A^I_{a,\mu}(x) = \frac{2(x-x_0)_\nu}{(x-x_0)^2 + \rho^2} \, \eta_{a\mu\nu}. \tag{1.44}$$

where x_0 is the center of the solution, ρ its size parameter and

$$\eta_{a\mu\nu} = \begin{cases} \epsilon_{a\mu\nu} & \mu, \nu = 1, 2, 3 \\ \delta_{a\mu} & \nu = 4 \\ -\delta_{a\nu} & \mu = 4 \\ 0 & \mu = \nu = 4 \end{cases} \tag{1.45}$$

is the so-called *'t Hooft tensor* [26], which determines the color structure of the field $A^a_\mu(x)$. This solution is called (BPST-)*instanton*.

An anti-selfdual solution can be obtained immediately by replacing $\eta_{a\mu\nu} \to \bar{\eta}_{a\mu\nu}$, where the entries in the temporal direction ($\nu = 4$ or $\mu = 4$) have flipped signs:[6]

$$A^A_{a,\mu}(x) = \frac{2x_\nu}{x^2 + \rho^2} \, \bar{\eta}_{a\mu\nu}. \tag{1.46}$$

Accordingly, this is called *anti-instanton*.

Let us further discuss some of the most important properties of (anti-)instantons. Eq. (1.44) implies that A_μ approaches indeed a pure gauge configuration for $|x| \to \infty$. Furthermore, using the definitions one gets the action density of an (anti-)instanton (cf. Ref. [27]):

$$S^{A/I}(x) = \frac{1}{4g^2}(F^a_{\mu\nu}(x))^2 = \frac{1}{g^2}\frac{48\rho^4}{(x^2 + \rho^2)^4}. \tag{1.47}$$

It decays as x^{-8} with distance x from center which means that the object is strongly located in space-time and this is why it can be considered as a pseudo-particle that represents an "instantaneous" space-time event.

Integrating the action density Eq. (1.47) yields a total action [28]

$$S^{A/I} = \frac{8\pi^2}{g^2} \tag{1.48}$$

for both instantons and anti-instantons. It is important to note that the total action does not depend on the size parameter or the location of the center. Using the saturated Bogomolny bound Eq. (1.42) together with Eq. (1.48) one gets the topological charge of an (anti-)instanton:

$$Q_{\text{top}} = \frac{1}{16\pi^2} \int d^4x \, \text{tr}\{F_{\mu\nu}\tilde{F}^{\mu\nu}\} = \begin{cases} 1 & F_{\mu\nu} = +\tilde{F}_{\mu\nu} \text{ (instanton)} \\ -1 & F_{\mu\nu} = -\tilde{F}_{\mu\nu} \text{ (anti-instanton)} \end{cases} \tag{1.49}$$

---

[5]In order to obtain a $SU(3)$ solution one can use the fact that there are $SU(2)$ subgroups embedded in $SU(3)$.

[6]Without loss of generality one can set $x_0 = 0$.

From the index theorem Eq. (1.36) one can further conclude that there exists at least one left-handed zero mode in the presence of an instanton.

Instantons play an important role in the nonperturbative approach to QCD. They have been proposed as building blocks of the QCD vacuum, using the instanton solution as a basis for a semiclassical expansions of the path integral.

1.4.3. Topology of gauge fields – a closer look

In this section we have a closer look at the mathematical framework of topology in gauge theories.

In the derivation of the index theorem and for the instantons one finds an integer number, which characterizes the gauge fields, namely the topological charge Q_{top}. It is obvious that an integer cannot change continuously if the underlying gauge field is smoothly transformed. This was the motivation to call it a topological quantity, but there is a much deeper relation to the gauge fields. To see this, one has to rewrite $\text{tr}\{F_{\mu\nu}\tilde{F}^{\mu\nu}\}$ in the definition of the topological charge as a total derivative of a four-current [24]:

$$Q_{\text{top}} = \frac{1}{16\pi^2}\int d^4x\, \epsilon_{\mu\nu\rho\sigma}(A_\nu^a\partial_\rho A_\sigma^a + \frac{1}{3}f_{abc}A_\nu^a A_\rho^b A_\sigma^c) \equiv \int d^4x\partial_\mu K_\mu(A), \qquad (1.50)$$

where we have defined the *Chern-Simons current* K_μ

$$K_\mu(A) = \frac{1}{16\pi^2}\epsilon_{\mu\nu\rho\sigma}(A_\nu^a\partial_\rho A_\sigma^a + \frac{1}{3}f_{abc}A_\nu^a A_\rho^b A_\sigma^c). \qquad (1.51)$$

The resulting integral can be reduced by virtue of Gauss' law to a surface integral over the boundary of $\mathbb{R}^4$, which is isomorphic to the three-sphere S_3:

$$Q_{\text{top}} = \int_{S_\infty^3} d^3\sigma K_\perp\big(A_\mu = ig(x)^\dagger\partial_\mu g(x)\big). \qquad (1.52)$$

Thus, Q_{top} depends only on the boundary gauge fields of our space, which are, due to the considerations from above, pure gauge fields and group elements of $SU(N)$. This integral is a generalization of the winding number and it is well studied in algebraic topology and differential geometry. It is known under many different names like *Pontryagin index*, *topological charge*, *second Chern class*, *winding number* or *instanton number*. An explicit calculation of this Pontryagin index can be quite difficult for a generic gauge group and goes far beyond the scope of this thesis. Thus, we just want to state that for $SU(N)$ it is always an integer number.

The topological charge is a global quantity characterizing the complete vacuum state, but one is also interested in the local topological charge density

$$q_{\text{top}}(x) = \frac{1}{16\pi^2}\text{tr}\{F_{\mu\nu}(x)\tilde{F}^{\mu\nu}(x)\}, \qquad (1.53)$$

because this quantity is strongly tied to chiral symmetry breaking through the local version of the Atiyah Singer index theorem and to confinement. Hence, if there ever will be a full solution to QCD, it has to predict how this density is distributed in space-time.

1.4.4. Models of the QCD vacuum

In the low energy regime of QCD there still exist many unsolved problems. This situation is rather subtle from the perspective of quantum mechanics, where one usually tries to solve the ground state first and on that basis more complicated states are tackled.

In QCD no analytic solution to the ground state, the QCD vacuum, has been found. This state is highly nonperturbative and one needs nonperturbative methods like Lattice QCD (see next chapter), which offers numerical results from first principles. Another approach is to start with a model of the QCD vacuum and try to explain the observed phenomena. Such models are often inspired by topological concepts and some are able to describe many aspects of confinement and chiral symmetry. A complete overview of all models is not possible and only a small selection thereof is presented. We focus on models based on instantons, as they provide direct access to the topological charge density. There are also other topological defects like center vortices or monopoles, for them we refer the reader to the standard literature.

The dilute instanton gas

One of the first "topological" models was the dilute instanton gas. Based on the localization property of instantons, one constructs an approximate ground state by a superposition of separated instanton and anti-instanton solutions. Such a solution is very close to the minimum of the classical action and, therefore, this model corresponds to a semi-classical expansion of the path-integral.

The success of this model lies in the fact that it provides a very intuitive explanation for chiral symmetry breaking [27]: A single (anti-)instanton is accompanied by a left-(right-)handed zero mode (see above). If N instantons and $N - Q_{\text{top}}$ anti-instantons are combined to state with topological charge Q_{top}, then all zero modes have to be arranged such that there are Q_{top} exact zero modes and $2N - Q_{\text{top}}$ near-zero modes. Therewith, a nonvanishing density of eigenmodes around zero is generated. This density is connected to the chiral condensate via the famous Banks-Casher relation [29]:

$$\langle \bar{\psi}\psi \rangle = \lim_{m \to 0} \frac{1}{V} \int d\lambda \rho(\lambda) \frac{m}{\lambda^2 + m^2} = -\pi \frac{\rho(0)}{V}, \tag{1.54}$$

where $\rho(\lambda)$ is the spectral density:

$$\rho(\lambda) = \langle \sum_n \delta(\lambda - \lambda_n) \rangle. \tag{1.55}$$

The dilute instanton gas has two major drawbacks. On the one hand, it has been shown by 't Hooft in one of his seminal papers [26] that it is not clear what suppresses arbitrary big instantons which would contradict the diluteness assumption, and, on the other hand, one cannot explain confinement in this model.

The instanton liquid

A further development of the instanton gas is the instanton liquid. In this model one replaces the diluteness condition by an interaction between instantons. Hence, it is

possible to avoid the infrared divergence of big instantons, while keeping the chiral symmetry-breaking mechanism. The instanton liquid model has been very successful in describing hadronic properties, but it also failed to explain confinement. Nonetheless, it still serves as a starting point for other models. For further reading and special instanton models see, e.g., Refs. [30, 31, 32, 28].

2

Lattice QCD

When calculating physical quantities in QCD, divergencies occur which make it necessary to introduce an upper momentum scale μ to get finite results. If a physical observable depends only on processes with momentum $q \ll \mu$, it should be independent of the cutoff and the limit $\mu \to \infty$ exists. This process goes under the name *regularization*.

A space-time lattice provides such a cutoff, as the lattice spacing $a \propto 1/\mu$. On a lattice one can in principle evaluate the path integral for any physical observable. Taking the continuum limit $a \to 0$ then corresponds to removing the cutoff.

In this chapter we introduce the basic formulations and notations of quarks and gluons on a lattice and show how the path integral is evaluated with Monte Carlo techniques. For an extensive introduction we refer to the classic textbooks [33, 34, 35, 36, 37].

2.1. Gluons on the lattice

The basic formulation of Lattice QCD or, more generally lattice gauge theory, goes back to the seminal work of Kenneth Wilson [38]. His starting point for a lattice regularized formulation of QCD is the so-called *parallel transporter* ($\mathcal{P}\exp$ denotes the path-ordered exponential)

$$ U(x,y) \equiv \mathcal{P} \exp \left\{ -i \int_{x,C}^{y} \mathrm{A}_\mu(s) ds^\mu \right\}, \qquad (2.1) $$

which connects the quark fields $\psi(x)$ and $\psi(y)$ along some contour C:

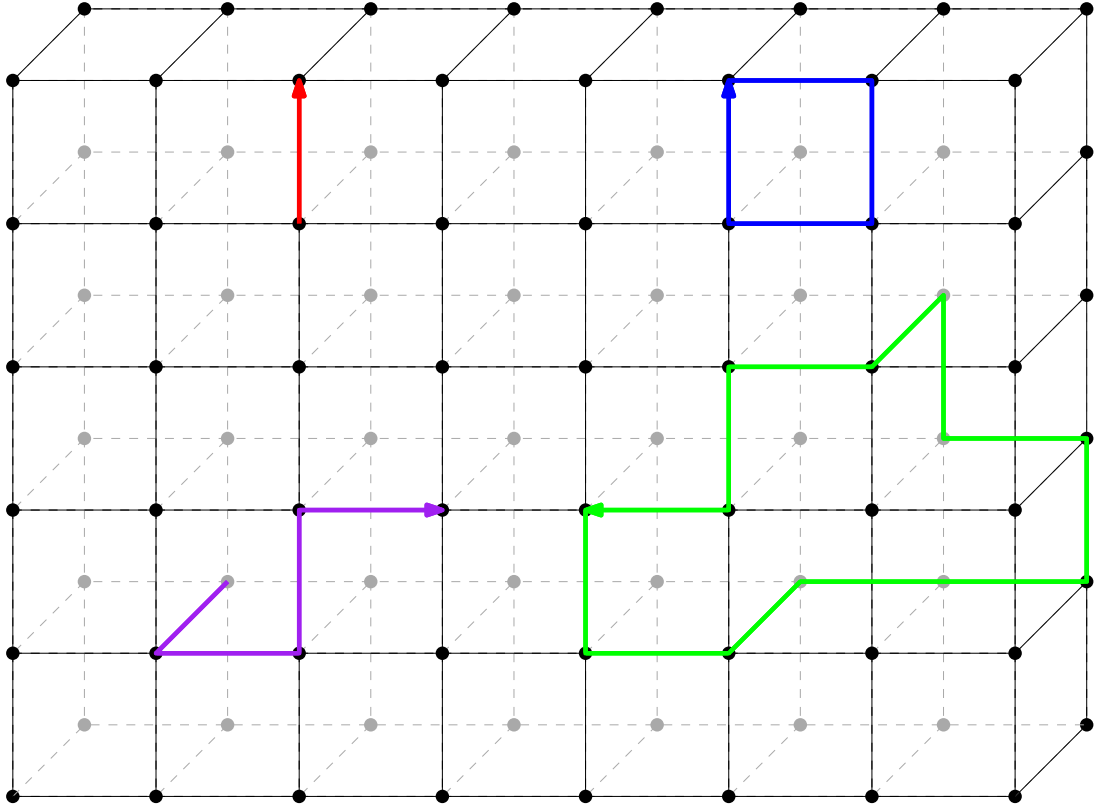$$ \psi(y) = U(x,y)\psi(x). \qquad (2.2) $$

Fig. 2.1: Illustration of the basic objects on the lattice (see text): gauge link (red), plaquette (blue), general parallel transporter (purple) and general Wilson loop (green).

The parallel transport will, in general, depend on the path C and the difference between two paths is obviously given by

$$U(x,x) \equiv \mathcal{P} \exp \left\{ -i \oint_C \mathrm{A}_\mu(s) ds^\mu \right\},\qquad(2.3)$$

where C is now a closed loop. Accordingly, this object is called *Wilson loop*.

A (Euclidean) space-time lattice with N_s spatial and N_t temporal sites and a lattice spacing a is introduced whose sites are labeled by the coordinates $x_\mu = a \cdot n_\nu$. The lattice spacing a does not have a physical meaning *a priori*, it can be determined from physical observables *a posteriori*. To this end, one evaluates a physical quantity like a hadron mass M on the lattice and relates it to the experimental value $M_{\mathrm{epx}} = Ma^{-1}$.

The quark fields reside on the lattice sites, which will be connected through the gauge fields by means of parallel transport between adjacent points (see also Fig. 2.1):

$$U_\mu(x) \equiv U(x, x+\hat{\mu}) = \mathcal{P} \exp \left\{ -i \int_x^{x+\hat{\mu}} \mathrm{A}(s) ds \right\} \approx e^{-iga\,\mathrm{A}_\mu(x+\frac{\hat{\mu}}{2})},\qquad(2.4)$$

where $\hat{\mu} = a \cdot e_\mu$ denotes the unit vector in μ-direction and the integral in the exponential has been approximated by its central value times the lattice spacing. This object is also called *(gauge) link*, because it connects two lattice sites. The integral can be approximated in other ways, but they will lead to the same result for $a \to 0$. From the definition it is easy to see that the hermitian conjugate of a link $U_\mu^\dagger(x)$ is just the parallel transporter in the opposite direction:

$$U_\mu^\dagger(x) = U(x + \hat{\mu}, x) \equiv U_{-\mu}(x + \hat{\mu}). \tag{2.5}$$

These links replace the gauge fields $\mathbf{A}_\mu$ as the fundamental degrees of freedom. This is advantageous because the links are members of the gauge group $SU(N_c)$ whereas the gauge fields are elements in the corresponding Lie-algebra. The gauge symmetry Eq. (1.11) takes a very simple form:

$$U_\mu(x) \to U_\mu'(x) = g(x)U_\mu(x)g^\dagger(x + \hat{\mu}), \tag{2.6}$$

where $g(x) \in SU(N_c)$. The fields transform in analogy to Eq. (1.10):

$$\psi(x) \to \psi'(x) = g(x)\psi(x) \qquad \text{and} \qquad \bar{\psi}(x) \qquad \to \bar{\psi}'(x) = \bar{\psi}(x)g^\dagger(x). \tag{2.7}$$

It is easy to see that the trace of a product of links along a closed contour on the lattice corresponds to the lattice version of the Wilson loops

$$W(C) = \frac{1}{N_c} \text{tr} \left\{ \prod_{(\mu,x) \in C} U_\mu(x) \right\}, \tag{2.8}$$

The factor $1/N_c$ is just conventional and normalizes the Wilson loop of $A_\mu = 0$ to 1.[1] According to the transformation property Eq. (1.11) and using the cyclicity of the trace, one easily sees that all Wilson loops are gauge-invariant. We want to remark, that we will also call the product of links itself Wilson loop, but it will be clear from context which object is meant.

A product of links along a square, is called *plaquette* $U_{\mu\nu}(x)$ (sometimes also $W_{\mu\nu}^{1\times1}(x)$ or $P_{\mu\nu}(x)$) and plays a very important role in the discretization of the gauge action Eq. (1.13). A simple exercise yields (cf. Ref. [37]):

$$U_{\mu\nu}(x) = U_\mu(x)U_\nu(x + \hat{\mu})U_\mu^\dagger(x + \hat{\nu})U_\nu^\dagger(x) = \exp\{ia^2 F_{\mu\nu}(x) + O(a^3)\}$$

$$\approx 1 + ia^2 F_{\mu\nu}(x) - \frac{a^4}{2} F_{\mu\nu}^2(x), \tag{2.9}$$

which allows for a lattice version of the gauge action:

$$S_G^W[U] \equiv \frac{2}{g^2} \sum_x \sum_{\mu > \nu} \text{Re} \, \text{tr}\{1 - U_{\mu\nu}(x)\}. \tag{2.10}$$

This is the famous *Wilson gauge action* or *plaquette action*. It can easily be shown that this action leads to the correct continuum expression of the gauge action

$$S_G^W[U] \overset{(2.9)}{=} a^4 \sum_x \frac{1}{2g^2} \sum_{\mu,\nu} \text{tr}\{F_{\mu\nu}^2(x) + \mathcal{O}(a^2)\} \overset{a \to 0}{\longrightarrow} \int d^4x \, \frac{1}{2g^2} \sum_{\mu,\nu} \text{tr}\{F_{\mu\nu}^2(x)\}. \tag{2.11}$$

---

[1]The trace of an element g of $SU(N_c)$ is bounded from above, $\text{tr}\{g\} \leq N_c$.

2.2. Quarks on the lattice

While it is straightforward to discretize gauge fields, we encounter a severe problem for the fermions. The term in the action containing the covariant derivative (in the μ-direction) can be written in terms of finite differences as

$$\bar{\psi}(x)D_\mu\psi(x) \rightarrow \frac{1}{2a}\Big(\bar{\psi}(x)U_\mu(x)\psi(x+\hat{\mu}) - \bar{\psi}(x)U_{-\mu}(x)\psi(x-\hat{\mu})\Big)$$

$$= \bar{\psi}(x)\Big(\frac{U_\mu(x)\delta_{x+\hat{\mu},y} - U_{-\mu}(x)\delta_{x-\hat{\mu},y}}{2a}\Big)\psi(y). \qquad (2.12)$$

This expression is obviously gauge invariant and leads to the lattice fermion action

$$S_F = \sum_{x,y}\bar{\psi}(x)\big[D(x,y,U) + m\delta_{x,y}\big]\psi(y) \qquad (2.13)$$

with the naive lattice Dirac operator (we will not use the Feynman slashed notation for lattice Dirac operators)

$$D(x,y,U) = \sum_{\mu=1}^{4}\gamma_\mu\frac{U_\mu(x)\delta_{x+\hat{\mu},y} - U_{-\mu}(x)\delta_{x-\hat{\mu},y}}{2a}. \qquad (2.14)$$

While this looks like a valid discretization it gives rise to 15 unphysical fermion modes.[2] As a consequence, the particle content is not correct and the continuum limit of the theory is spoiled. The reason for the fermion doubling is the absence of the chiral anomaly in the naive lattice discretization. We have seen in the previous chapter that the anomaly arises from chiral zero modes leading to a non-trivial Jacobian. For naive fermions each zero eigenvalue is 16-fold degenerate. Eight associated zero modes have positive chirality and the other eight have negative chirality [41]. Their contributions always cancel, leading to an anomaly-free theory.

Wilson circumvented the doubling problem by introducing an additional term in the action, which removes the unwanted poles in the propagator and is irrelevant in the continuum limit. His version of the massless lattice fermion action reads:

$$S_F^W[\overline{\psi},\psi,U] = a^4\sum_{x,y}\overline{\psi}(x)D_W(x,y,U)\psi(y) \qquad (2.15)$$

with the *Wilson Dirac operator*

$$D_W(x,y,U) = D(x,y,U) - \frac{a}{2}\sum_{\mu=1}^{4}\frac{U_\mu(x)\delta_{x+\hat{\mu},y} - 2\delta_{x,y} + U_{-\mu}(x)\delta_{x-\hat{\mu},y}}{a^2} \qquad (2.16)$$

The Wilson term is nothing but the discretization of the covariant Laplace operator Δ times $a/2$. This term vanishes in the continuum limit $a \rightarrow 0$ and gives the doublers a

---

[2]These modes occur as additional poles in the momentum space fermion propagator, that sit at each corner of the Brillouin zone. For a nice introduction we refer to Refs. [39, 40] or the standard textbooks.

mass of the order of the inverse cutoff. Thereby, the doubling modes get infinitely heavy and decouple from the theory. Unfortunately, we have to pay a high price for removing the doublers: We have to give up chiral symmetry for all finite lattice spacings. This issue will be addressed in Sec. 2.4.

These are all ingredients to write down a lattice regularized version of the QCD partition function

$$Z = \int [\mathcal{D}\,U_\mu][\mathcal{D}\,\bar\psi][\mathcal{D}\,\psi]\,e^{-S[\bar\psi,\psi,U]} \tag{2.17}$$

with the lattice action

$$\begin{aligned} S[\bar\psi,\psi,U] &= S_F^W[\bar\psi,\psi,U] + S_G^W[U] \\ &= \frac{2}{g^2}\sum_x\sum_{\mu>\nu}\mathrm{Re\,tr}\{1 - U_{\mu\nu}(x)\} + a^4\sum_{x,y}\bar\psi(x)D_W(x,y,U)\psi(y). \end{aligned} \tag{2.18}$$

2.3. Improved gauge actions

Many results obtained from Wilson's formulation of Lattice QCD are in a good qualitative agreement with experiment. If one wants to obtain quantitative results, one has to spend an enormous amount of computing time and make sure that all systematic uncertainties are under control. The quantitative differences result from lattice artifacts (especially finite lattice spacing) and explicit chiral symmetry breaking terms, which lead to large errors in the continuum extrapolation.

Regrettably, we are unable to simulate at an arbitrary small lattice spacing due to computational limitations. Therefore, we need ways to improve the original approach. One of the most successful approaches is the Symanzik improvement program [42, 43], which is standard in modern Lattice QCD. The idea is quite simple: One adds irrelevant operators[3] as counter-terms to remove $\mathcal{O}(a^n)$ contributions from the action and observables. The situation is very similar to higher order discretization schemes, which use more than just a nearest-neighbor finite difference. The counter terms can improve the scaling towards the continuum limit if they are determined properly. Better scaling enables a better extrapolation to the continuum limit and, hence, reduces the number of different lattice spacings one has to simulate.

The simplest irrelevant terms for the gauge actions have dimension six. These are Wilson loops made of six links, which are either planar 2×1 loops $W_{\mu\nu}^{2\times1}$ or out-of-plane parallelograms $W_{\mu\nu\rho}^{1\times1\times1}$ (see Fig. 2.2). The general form of such an action reads

$$\begin{aligned} S_G^{\mathrm{imp}} = \beta\sum_x\Bigg\{ &c_0\sum_{\mu<\nu}\Big(1 - \tfrac{1}{N_c}\,\mathrm{Re\,tr}\,W_{\mu\nu}^{1\times1}(x)\Big) + c_1\sum_{\mu,\nu}\Big(1 - \tfrac{1}{N_c}\,\mathrm{Re\,tr}\,W_{\mu\nu}^{2\times1}(x)\Big) \\ &+ c_2\sum_{\mu\neq\nu\neq\rho}\Big(1 - \tfrac{1}{N_c}\,\mathrm{Re\,tr}\,W_{\mu\nu\rho}^{1\times1\times1}(x)\Big)\Bigg\}. \end{aligned} \tag{2.19}$$

---

[3] An irrelevant operator in the action has mass dimension bigger than 4 and, therefore, it has to be multiplied by some power of the lattice spacing.
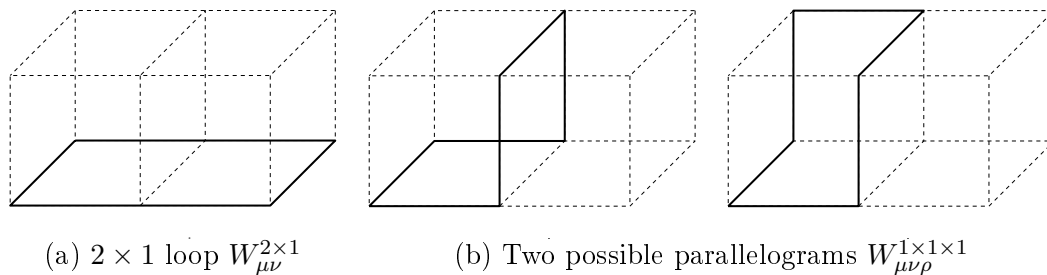
(a) 2×1 loop $W_{\mu\nu}^{2\times1}$ (b) Two possible parallelograms $W_{\mu\nu\rho}^{1\times1\times1}$

Fig. 2.2: Illustration of different types of Wilson loops contributing to the improved action of Eq. (2.19).

In principle, the three coefficients c_0, c_1 and c_2 are free parameters. They are not unique and depend on certain improvement criteria.

Let us first neglect the non-planar contribution by setting $c_2 = 0$. In order to get the correct coefficient of the leading order in a we demand the normalization

$$c_0 + 8c_1 = 1. \tag{2.20}$$

This normalization is, however, only a convention. Any other factor can be absorbed in the renormalization of the coupling $g^2 = \frac{2N_c}{\beta}$.

The *Symanzik action* [44, 45] and the *Iwasaki action* [46, 47] are of this type and their coefficients read:[4]

$$c_1 = \begin{cases} -\frac{1}{12} & \text{Symanzik} \\ -0.331 & \text{Iwasaki} \end{cases} \tag{2.21}$$

There are many other improved actions, like the *Lüscher-Weisz action* where also parallelogram terms are used. For the sake of brevity we refer to Refs. [44, 45, 48, 49].

A completely different approach is the so-called *tad-pole improvement* [50, 51, 52]. To understand its idea, one has to look at the lattice representation of the links

$$U_\mu(x) = e^{ia\,\mathrm{A}_\mu(x)} = 1 + ia\,\mathrm{A}_\mu(x) - \frac{a^2}{2}\,\mathrm{A}_\mu^2(x) + \ldots. \tag{2.22}$$

The term of $\mathcal{O}(a^2)$ seems to be harmless, but this is only true on a classical level. In a quantum theory it gives rise to divergent tadpole diagrams $\propto 1/a^2$. Accordingly, their contribution is $\mathcal{O}(1)$. In order to reduce the tadpole contribution, one can factor out an average link field u_0

$$U_\mu(x) \to \frac{1}{u_0} U_\mu(x). \tag{2.23}$$

The average of a link is not rigorously defined, but typically the expectation value of the link in Landau gauge or the expectation value of the plaquette are used

$$u_0 = \left(\frac{1}{N_c} \left\langle \mathrm{Re}\,\mathrm{tr}\{U_{\mu\nu}\} \right\rangle \right)^{1/4}. \tag{2.24}$$

---

[4]A detailed derivation of the coefficients can be found in the original publications.

The tad-pole coefficient u_0 has to be determined self-consistently for each action and coupling. Hence, extra work is needed before the final lattice simulation can be carried out. Nevertheless, a great advantage is that once the parameters are set, they lead to an improvement without additional computational effort.

Tad-pole and gauge action improvements are often used in combination, leading to a much better scaling towards the continuum limit than a single method.

2.4. Chiral symmetry on the lattice

2.4.1. No-go theorem

When deriving the Wilson fermion action, we had to sacrifice chiral symmetry in order to remove the fermion doublers. This is not an accident, but a fundamental problem of the lattice formulation. It can be traced back to the famous no-go theorem of Nielsen and Ninomiya [53], which will be briefly discussed in the following.

Let us consider the general form of the free action of a massless fermion on the lattice:

$$S_F = a^4 \sum_{x,y} \overline{\psi}(x) D(x-y) \psi(y). \tag{2.25}$$

The no-go theorem states that it is impossible for the translation-invariant Dirac operator $D(x-y)$ to fulfill the following conditions simultaneously on a torus:

1. D is a local operator, which means that

$$\|D(x-y)\| \leq A e^{-c|x-y|}. \tag{2.26}$$

    for A and $c > 0$ being constants.

2. The Fourier transform $\tilde{D}(p)$ has the correct continuum limit:

$$\tilde{D}(p) = i\gamma_\mu p^\mu + O(ap^2) \qquad \text{for} \qquad p \ll \frac{\pi}{a}. \tag{2.27}$$

3. There are no fermion doublers.

4. D is chirally symmetric and, accordingly, D and γ_5 anticommute:

$$\{D, \gamma_5\} = D\gamma_5 + \gamma_5 D = 0. \tag{2.28}$$

The first three conditions are essential properties of the theory and should hold in any case. Consequently, one has to give up the chiral symmetry. In the Wilson action Eq. (2.15) an additional $\mathcal{O}(a)$ term is introduced to remove the fermion doublers. At the same time this term breaks chiral symmetry at any finite lattice spacing and the no-go theorem does not apply. The price of the additional term is manifold, like an additive mass renormalization, which requires a lot of fine tuning to reach the physical point. Furthermore, the relation of chiral symmetry and topology is spoiled in its original sense and it is *a priori* not clear how harmful this is.

2.4.2. Ginsparg-Wilson relation

The no-go theorem raises the question if there is a lattice version of chiral symmetry, which keeps essential continuum properties and leads to a correct continuum limit. To this end, Ginsparg and Wilson suggested to modify the chiral symmetry condition of Eq. (2.28) as follows [54]:

$$\{D, \gamma_5\} = aD \, 2R \, \gamma_5 \, D, \tag{2.29}$$

where R is a local operator usually set to $\frac{1}{2}$ (for details see [39]). This Ginsparg-Wilson relation, however, implies that the fermion action is not invariant under the usual chiral transformation (cf. Eq. (1.29)):

$$\delta(\overline{\psi}D\psi) = (\delta\overline{\psi})D\psi + \overline{\psi}D(\delta\psi) = i\theta\overline{\psi}(\gamma_5 D + D\gamma_5)\psi \stackrel{2.29}{=} i\theta\overline{\psi}(aD\gamma_5 D)\psi \neq 0. \tag{2.30}$$

The remedy for this problem is to change the notion of chiral symmetry on the lattice and to make the transformation dependent on the gauge field by introducing an additional term $-\frac{a}{2}D[U]$ [55]. The modified chiral symmetry reads as follows:

$$\psi \rightarrow \psi + \delta\psi \qquad \text{and} \qquad \overline{\psi} \rightarrow \psi + \delta\overline{\psi}, \tag{2.31}$$

with the infinitesimal variations

$$\delta\psi = i\theta\gamma_5\left(1 - \frac{a}{2}D\right)\psi \qquad \text{and} \qquad \delta\overline{\psi} = i\theta\overline{\psi}\left(1 - \frac{a}{2}D\right)\gamma_5 \tag{2.32}$$

for the flavor singlet transformation and

$$\delta\psi = i\theta^a T^a \gamma_5\left(1 - \frac{a}{2}D\right)\psi \qquad \text{and} \qquad \delta\overline{\psi} = i\theta^a T^a \overline{\psi}\left(1 - \frac{a}{2}D\right)\gamma_5 \tag{2.33}$$

for the flavor multiplet (cf. Sec. 1.3). It is straightforward to show that the fermion action is invariant and that the usual chiral symmetry transformation is restored in the continuum limit.

Furthermore, the chiral anomaly is recovered in contrast to the naive fermion action. Like in the continuum, one finds that the fermion measure is not invariant under the modified chiral symmetry. According to Ref. [55] we get ($a = 1$):

$$\delta(d\overline{\psi}d\psi) = i\theta \operatorname{Tr}\{\gamma_5 D\}(d\overline{\psi}d\psi) + O(\theta^2)$$
$$= i\theta 2N_f \operatorname{index}(D)(d\overline{\psi}d\psi) + O(\theta^2), \tag{2.34}$$

where it has been used that solutions of the Ginsparg-Wilson relation hold [40, 55]:

$$\operatorname{Tr}\{\gamma_5 D\} = 2(n_L - n_R) \equiv 2 \cdot \operatorname{index}(D). \tag{2.35}$$

Hence, all Ginsparg-Wilson fermions satisfy an exact index theorem (see Sec. 3.2). The challenge is to find an explicit solution.

2.4.3. Overlap fermions

A very general solution of the Ginsparg-Wilson relation is

$$D = \frac{1}{a}(\mathbb{1} - V), \tag{2.36}$$

with a unitary matrix V.

The most prominent solution is the so-called *overlap operator D_{ov}*. It was first introduced by Neuberger [56, 57] and reads as follows:

$$D_{ov} = \frac{1}{a}\left(\mathbb{1} - \frac{A}{\sqrt{A^\dagger A}}\right) \qquad \text{with} \qquad A = \mathbb{1} - aD_{\text{ker}} \tag{2.37}$$

where the kernel Dirac operator D_{ker} has to be local and doubler-free, like the Wilson Dirac operator from Eq. (2.16) (This special choice is also called Neuberger operator).

The conceptual clarity of this formulation has a cost. The major drawback is the numerical expense, due to the need to calculate the inverse square root of a huge matrix or sign function ($\text{sign}(A) \equiv A/\sqrt{A^\dagger A}$). All known solutions of the Ginsparg-Wilson relation share this problem and lattice simulations with exactly chiral fermions are one of the biggest challenges in todays Lattice QCD.

2.5. More on fermion actions

In this section we give an overview of alternative formulations of lattice fermions. The selection in not complete and we will only focus on the actions which are used in this thesis.

2.5.1. Nonperturbatively improved clover Wilson fermions

Naive Wilson fermions break chiral symmetry at finite lattice spacing by an irrelevant dimension-five operator. This term is suppressed by one power of the lattice spacing and, therefore, we expect lattice artifacts to be of $\mathcal{O}(a)$.

The Wilson term is not the only possible dimension five term. One finds one further term which can be included in the action

$$S_{\text{SW}} = a^5 \, c_{\text{SW}} \frac{ig}{4} \sum_x \bar{\psi}(x)\sigma_{\mu\nu}F_{\mu\nu}(x)\psi(x) \tag{2.38}$$

The coefficient c_{SW} is called *Sheikholeslami-Wohlert coefficient* [58]. Correspondingly, the complete fermion action reads

$$S_F^{\text{clover}} = S_{\text{Wilson}} + S_{\text{SW}}, \tag{2.39}$$

which yields a modified Dirac operator

$$D^{\text{clover}}(x,y,U) = D^{\text{naive}}(x,y,U) - a\big(\Delta_{x,y} + c_{\text{SW}}\frac{ig}{4}\sigma_{\mu\nu}F_{\mu\nu}(x)\delta_{x,y}\big). \tag{2.40}$$

The term $F_{\mu\nu}$ is a suitable lattice discretization of the field strength tensor, which will be discussed in detail in the next chapter. This action is, due to the clover leaf pattern of this term, also known as the *clover Wilson action*. The main advantage of is that the additional term can be used to eliminate $\mathcal{O}(a)$ lattice artifacts, yielding results with a much nicer scaling towards the continuum limit.

The coefficient c_{SW} can be found in various ways. It can either be determined in (lattice) perturbation theory [58, 49] or nonperturbatively [59] by suitable measurements. The latter is even capable of removing all $\mathcal{O}(a)$ contributions from the action. Nonetheless, chiral symmetry is explicitly broken and all subtleties are inherited from the standard Wilson formulation.

2.5.2. Twisted mass fermions

An alternative formulation of QCD are *twisted mass fermions* [60, 61, 62], where an additional isospin-breaking mass term is introduced into the theory. The action of this theory for two flavors and in a compact vector notation (in flavor space) reads:

$$S_F^{\mathrm{tm}} = a^4 \sum_{x,y} \Phi(x)(D_W(x,y,U)\, \mathbb{1}_2 + m\, \mathbb{1}_2\, \delta_{x,y} + i\mu\gamma_5\tau^3\delta_{x,y})\Phi(y). \tag{2.41}$$

$\tau_3 = \left(\begin{smallmatrix} 1 & 0 \\ 0 & -1 \end{smallmatrix}\right)$ is the third Pauli matrix that acts in flavor space, and μ is a real and positive parameter which is also called the twisted mass parameter. Therefore, we can write the twisted mass Dirac operator in the form

$$D^{\mathrm{tm}}(x,y,U,m,\mu) = D_W(x,y,U)\, \mathbb{1}_2 + m\, \mathbb{1}_f\, \delta_{x,y} + i\mu\gamma_5\tau^3\delta_{x,y}. \tag{2.42}$$

The validity of this approach is not directly obvious and conceptual problems arise from isospin breaking, but there are some nice practical advantages of this approach. One can, for example, show that the resulting fermion determinant is strictly positive for any mass m. This is not necessarily true for conventional Wilson fermions, as one might find gauge configurations with a zero or negative determinant that lead to a non-positive probability distribution (such configuration are called exceptional configurations). The reason for this is that the twisted mass term acts as an infrared regulator which introduces a lower bound for the fermion determinant [37]

$$\det\{D^{\mathrm{tm}}\} > 2\mu > 0. \tag{2.43}$$

Furthermore, it has been shown that there is a very simple way to achieve $\mathcal{O}(a)$ improvement by tuning the twisted mass term to *maximal twist* (see Refs. [62, 63]).

In order explain this maximal twist, one has to change the parametrization of the action. The usual mass term and the twisted mass term can be combined as follows

$$m\, \mathbb{1}_2 + i\mu\gamma_5\tau^3 = Me^{ia\gamma_5\tau^3}, \tag{2.44}$$

where we have defined the *polar mass* $M = \sqrt{m^2 + \mu^2}$ and the *twist angle* $\alpha = \arctan(\mu/m)$. Maximal twist corresponds to $\alpha = \pi/2$ or setting $m = 0$ in the unrenormalized theory (in the renormalized theory one has to set the mass to some critical value). Doing so, one finds that the spectrum is automatically $\mathcal{O}(a)$-improved.

The combination of $\mathcal{O}(a)$-improvement, absence of exceptional configurations and the simple form of the action have made twisted mass simulation very popular. As a variant of Wilson fermions, they break chiral symmetry explicitly and, hence, one needs fine-tuning to reach the chiral limit. The major drawback is the additional breaking of isospin symmetry at finite lattice spacing. Some physical quantities are strongly affected, like the mass of the neutral and charged pseudo-scalar particle, others are not. Accordingly, this effect has to be studied empirically.

2.5.3. Staggered fermions

Staggered fermions, also known as *Kogut-Susskind fermions* [64], follow a completely different strategy. Instead of improving the finite-difference approximation, one can rewrite the naive fermion action to obtain a formulation which has only 4 doublers instead of 16, while keeping remnants of chiral symmetry. In the following we give a short introduction to staggered fermions. For more details we refer to standard textbooks on lattice field theory, e.g. Refs. [37, 34, 35, 36], or the detailed review article from the MILC Collaboration [65].

The construction of the staggered fermion action starts from the naive fermion action (cf. Eq. (2.14)):

$$S_F[\psi, \bar{\psi}] = a^4 \sum_x \bar{\psi}(x) \Big(\sum_{\mu=1}^4 \gamma_\mu \frac{\psi(x+\hat{\mu}) - \psi(x-\hat{\mu})}{2a} + m\psi(x)) \Big). \tag{2.45}$$

to which the following transformation is applied

$$\psi'(x) = \Gamma(x)\psi(x) \quad \text{and} \quad \bar{\psi}'(x) = \bar{\psi}'(x)\Gamma^\dagger(x), \tag{2.46}$$

with a space-time dependent matrix

$$\Gamma(x) = \gamma_4^{x_4} \gamma_3^{x_3} \gamma_2^{x_2} \gamma_1^{x_1}. \tag{2.47}$$

x_μ denote the components of the lattice coordinate vector $x = (x_1, x_2, x_3, x_4)$. It is straightforward to show that this transformation leaves the mass term invariant, but changes the finite difference expression

$$\bar{\psi}(x)\gamma_\mu\psi(x\pm\hat{\mu}) = \bar{\psi}'(x)\eta_\mu(x)\, \mathbb{1}\, \psi'(x\pm\hat{\mu}) \tag{2.48}$$

where the so-called staggered phases

$$\eta_\mu(x) = (-1)^{x_1+x_2+\ldots+x_{\mu-1}} \quad \text{and} \quad \eta_1(x) = 1 \tag{2.49}$$

have been introduced. The resulting Dirac operator is diagonal in spinor space and, thus, all four components of the transformed field are described by the same action functional. Hence, three components can be omitted, leading to the usual form of the staggered fermion action

$$S_F^{\text{stag}}[\chi, \bar{\chi}, U] = a^4 \sum_x \bar{\chi}(x) \Big(\sum_{\mu=1}^4 \eta_\mu(x) \frac{U_\mu(x)\chi(x+\hat{\mu}) - U_\mu^\dagger(x-\hat{\mu})\chi(x-\hat{\mu})}{2a} + m\chi(x) \Big), \tag{2.50}$$

where $\chi(x)$ and $\bar{\chi}(x)$ are Grassmann-valued fields without spinor structure (but with color components). Accordingly, the spin-diagonal staggered Dirac operator reads as follows

$$D^{\text{stag}}(x,y,U) = \sum_{\mu=1}^{4} \eta_\mu \frac{U_\mu(x)\delta_{x+\hat{\mu},y} - U_{-\mu}(x)\delta_{x-\hat{\mu},y}}{2a} + m\,\mathbb{1}\,\delta_{x,y}. \qquad (2.51)$$

Due to the fact that we keep only one of four spinor components, we reduce the number of doublers from 16 to 4, which is at least closer to the real particle content. In order to see the effect of this transformation on chiral symmetry, we apply the staggered transformation from above (Eq. (2.46)) to $\bar{\psi}\gamma_5\psi$:

$$\bar{\psi}(x)\gamma_5\psi(x) = \bar{\psi}'(x)(-1)^{x_1+x_2+x_3+x_4}\,\mathbb{1}\,\psi'(x). \qquad (2.52)$$

This implies to define

$$\eta_5(x) = (-1)^{\sum_\mu x_\mu} = (-1)^{x_1+x_2+x_3+x_4} \qquad (2.53)$$

as the staggered analog of the γ_5-matrix. The massless staggered action is obviously invariant under the transformation ($\theta \in \mathbb{R}$):

$$\chi(x) \to e^{i\theta\eta_5(x)}\chi(x) \qquad \text{and} \qquad \bar{\chi}(x) \to \bar{\chi}(x)e^{i\theta\eta_5(x)}. \qquad (2.54)$$

This is the staggered version of the global chiral symmetry transformation. The main problem of the formulation becomes clear if one reintroduces quark degrees of freedom in order to obtain the usual hadron interpolators. To this end, one has to use special combinations of the (staggered-)quark fields around a hypercube, which lead to four quark fields with different (lattice spacing dependent) mass terms. In order to distinguish these fields from the flavor degrees of freedom, one calls them *tastes*. The consequence of these tastes is that there is no one-to-one correspondence of the staggered particle spectrum to the continuum theory and we find four candidates for a single particle in the staggered spectrum which all have different masses. These differences can be very large. Even at small lattice spacings they can be of the order of the hadron mass and, thus, we would have a theory with a completely different mass spectrum. As a consequence, many improvements of the naive staggered action have been proposed to get a better agreement with the continuum theory.

The main idea behind these improvements is that the violations result from the distribution of the tastes on neighboring lattice sites. Therefore, they are strongly affected by gluon momenta of the order π/a, i.e., by ultraviolet modes. One strategy to reduce taste violations is to suppress the coupling to these ultraviolet modes. Examples for such improved actions are the asqtad ($\mathcal{O}(a^2)$ tad-pole improved) staggered action, the HISQ (highly improved staggered quark) action or stout smeared staggered action. For the sake of brevity we refer the reader to Ref. [65].

Staggered fermions have been the subject of a heated debate for many years. The main concern is a technical trick, which is used to get closer to the particle content in nature, i.e., two light quarks and one heavy quark. One replaces each fermion determinant, which occurs after integrating out the fermions in the path integral, by

its fourth root. This yields an effective action with the correct number of tastes, but the conceptual problems of this approach are manifold and we refer to some recent discussions in Refs. [66, 67, 68, 69, 70, 71, 72, 73, 74, 75, 76, 77, 78]. Many results are, nevertheless, in good agreement with experiment (see, e.g., [65]) and staggered fermions are used and promoted by several groups in the lattice community.

2.5.4. Chirally improved fermions

As already mentioned above, it is computationally very expensive to use Ginsparg-Wilson fermions. Therefore, one can try to find an approximated solution to the Ginsparg-Wilson relation to get an operator with nicer chiral properties, but less computational effort. These *chirally improved fermions* [79] are based on the most general form of a Dirac operator, which reads for the gauge group $SU(3)$ as follows:

$$D^{\text{CI}}(x, y, U) = \sum_{k=1}^{16} \alpha^k(x, y, U)\Gamma_k$$

$$\text{with} \quad \alpha^k(x, y, U) = \sum_{p \in \mathfrak{P}^k(x \to y)} c_p^k \prod_{\mu \in p} U_\mu, \tag{2.55}$$

where Γ_k are the 16 generators of the Dirac algebra (see Appendix A.2) and $\alpha^k(x, y, U)$ are the sums of link products along the paths $\mathfrak{P}^k(x \to y)$ connecting lattice site x and y. The operator of Eq. (2.5.4) can be inserted in the Ginsparg-Wilson relation and by solving the resulting algebraic equations for c_p^k, one can, in principle, construct an exactly chiral operator.

Obviously, it is impossible to include all paths, as there are infinitely many. One can, however, truncate the set of all possible paths and try to find a proper approximation respecting the first three properties of the no-go theorem. For a good introduction we refer to the textbook of Gattringer and Lang [37] and the original publication [79].

2.6. Monte Carlo simulations

So far, we have only presented the basic concepts and definitions of the discretized theory. The following section is dedicated to a more practical question: How do we evaluate the path integral in this lattice formulation?

Due to the lattice discretization, one has a finite number of group integrals, but the number of degrees of freedoms is too big to be tractable explicitly. Thus, one uses statistical methods to approximate the expectation values of observables. Given an ensemble of N gauge field configurations U_n, distributed according to

$$P(U) = \text{Det}(D[U] - m)\exp\{-S[U]\}, \tag{2.56}$$

one can estimate the expectation value of an observable O by a finite sum:

$$\langle O \rangle \approx \frac{1}{N} \sum_{U_n} O[U_n] + \mathcal{O}\left(\frac{1}{\sqrt{N}}\right), \tag{2.57}$$

where $O[U_n]$ is the value of the observable evaluated on a single configuration U_n. The weight ensures that those configurations which are close to a minimum of the action, are more likely and contribute more to the integral.

One of the main challenges is the generation of such ensembles U_n. This is where the main part of the computing time has to be spent. Especially the fermion determinant causes problems, as we have to deal with a computationally expensive inversion of a huge matrix. Hence, early Lattice QCD results have been obtained in the *quenched approximation*, where the determinant is set to a constant.

In order to justify this approximation in the case of Wilson fermions, one can use the hopping parameter expansion (see Ref. [34] or Ref. [37]). In doing so, one parameterizes $D_W \propto (\mathbb{1} - \kappa H)$, where H includes all nearest neighbor terms and $\kappa = (2am + 8)^{-1}$. This leads to an expansion of the fermion determinant of the form

$$\mathrm{Det}(\mathbb{1} - \kappa H) = \exp\left\{ \mathrm{tr}\log(\mathbb{1} - \kappa H) \right\} = \exp\left\{ -\sum_{n=1}^{\infty} \frac{1}{n}\kappa^n \, \mathrm{tr}\{H^n\} \right\}, \qquad (2.58)$$

for which a simple interpretation is possible: $\mathrm{tr}\{H^n\}$ includes all closed loops of links of length n (in lattice units). These are weighted by $\kappa^n \propto 1/m^n$ and, thus, suppressed for heavy, static quarks. Many features of QCD have been verified within the quenched approximation, but one has to deal with unavoidable systematic errors. Dynamical simulations are, therefore, essential.

This section shall give an overview over the algorithms used to generate quenched and dynamical ensembles. We will close with a short discussion of the autocorrelation of gauge configurations within an ensemble.

2.6.1. Quenched approximation

The basic algorithm for the generation of a gauge ensembles is the so-called *Metropolis algorithm* [80]. As all standard textbooks discuss this method in detail, we will give only a short summary and refer to, e.g., Ref. [37]. The Metropolis algorithm consists of subsequent Monte Carlo updates, which can be broken down into three steps:

Step 1: Replace one link variable with a random one respecting detailed balance, i.e., a symmetric probability:

$$P\big(U_\mu^{\mathrm{old}} \to U_\mu^{\mathrm{new}}\big) = P\big(U_\mu^{\mathrm{new}} \to U_\mu^{\mathrm{old}}\big) \qquad (2.59)$$

Step 2: Determine the change of the action $\Delta S = S^{\mathrm{new}} - S^{\mathrm{old}}$ and accept the new link if $e^{-\Delta S}$ is greater than a random number from the interval $[0, 1)$, otherwise reject it.

Step 3: Take the next link and repeat from step 1.

The second step is essential. Only accepting new links which lower the action, would continuously reduce the action and drive the fields to a classical solution. The random acceptance introduces noise, which correspond to quantum fluctuations.

The single update is used in the Metropolis algorithm to generate an ensemble of statistically independent configurations. The ensemble generation can be subdivided into different parts:

1. Start with an arbitrary configuration.

2. Perform Monte Carlo updates until thermal equilibrium is reached, i.e., all configurations have the correct probability distribution.

3. Save each (or every n-th) configuration for further measurements or calculate the desired observable "on-the-fly".

4. Calculate expectation values.

There are many variants of this algorithm, but the basic steps are common to all of them.

2.6.2. Hybrid Monte Carlo simulations

If one wants to go beyond the quenched approximation, the situation gets more complicated, as we have to deal with nonlocal fermion determinants. Algorithms based on local updates are not a good choice, because a local change of the gauge links involves an evaluation of a global quantity. Therefore, one prefers global updates. In the following we illustrate the basic algorithm, which became the standard solution to this problem.

Consider the Hamiltonian of a scalar field theory with action functional $S(\phi)$

$$H(\pi, \Phi) = \sum_x \frac{p^2(x)}{2} + S(\Phi(x)), \qquad (2.60)$$

which induces a field evolution in a fictitious time τ through the well known Hamilton equations (the "dot" denotes the τ-derivative):

$$\dot{\Phi}(x) = p(x) \qquad \text{and} \qquad \dot{p}(x) = -\frac{\partial S(\Phi)}{\partial p(x)}. \qquad (2.61)$$

Each set of initial values $\{p_0(x), \Phi_0(x)\}$ defines a unique *trajectory* and the set of all these trajectories describes the classical partition function

$$Z = \int [\mathcal{D}\,p][\mathcal{D}\,\phi]\,e^{-H(p,\Phi)} = \mathcal{N} \int [\mathcal{D}\,p][\mathcal{D}\,\phi]e^{-S(\Phi)}. \qquad (2.62)$$

An exact integration of the Hamilton equations conserves the Hamiltonian. Hence, the phase space is sampled corresponding to the canonical partition function if the momenta are refreshed periodically with Gaussian distributed random numbers. Expectation values are then obtained by averaging over a sufficient number of trajectories. In analogy to a system of molecules with a periodic external driving force one calls this a *(Hybrid) Molecular Dynamics algorithm* [81, 82].

As the Hamilton equations have to be evolved numerically (with a reversible integration scheme like the leapfrog integrator), finite step size errors are introduced. These errors would lead to a wrong sampling and, in turn, to wrong results. Therefore, one uses a Metropolis accept/reject step at the end of each trajectory, which accounts for the deviation of the final Hamiltonian from the initial one. The combination of these two ideas lead to the name *Hybrid Monte Carlo algorithm* (HMC) [83].

In the case of lattice gauge theory we need some further ingredients. On the one hand, the Hamilton equations have to be solved such that one remains in the gauge group and, on the other hand, one needs an efficient method to calculate the determinant for the change in the action. The latter can be achieved by the use of *pseudo-fermions*. Those are bosonic degrees of freedom that arise after rewriting the fermion determinant as[5]

$$\mathrm{Det}(D[U] + m) = \int [\mathcal{D}\,\bar{\Phi}][\mathcal{D}\,\Phi] e^{-\bar{\Phi}\frac{1}{D[U]+m}\Phi}, \tag{2.63}$$

yielding an effective action

$$S_{\mathrm{eff}} = S_G[U] - \ln\mathrm{Det}(D[U] + m) = S_G[U_\mu] - \bar{\Phi}\frac{1}{D[U]+m}\Phi. \tag{2.64}$$

At the beginning of each trajectory all pseudo-fermion fields are refreshed following the probability distribution Eq. (2.63) (pseudo-fermion heat-bath) and then one evolves the gauge fields with the resulting effective action. Accordingly, a matrix inversion has to be performed in every step of the molecular dynamics trajectory, which is the numerically most expensive part of the algorithm.

Today many variants of the HMC exist which try to improve on various parts of the algorithm. The central subjects of improvement is the autocorrelation of configurations, which is discussed in the next section.

2.6.3. Autocorrelation

The aforementioned algorithms are stochastic processes, that generate a sequence of gauge fields

$$U_1 \to U_2 \to U_3 \to \dots \tag{2.65}$$

Subsequent configurations, obtained from such a process, are not independent if they are generated in a computer, they are correlated. This, however, leads to biased expectation values of observables and wrong statistical errors. Correspondingly, it is of central importance to know the autocorrelation of the configurations, which can be defined for an observable O as (we follow Ref. [37])

$$C(O_i, O_{i+t}) = \Big\langle (O_i - \langle O_i \rangle)(O_{i+t} - \langle O_{i+t} \rangle) \Big\rangle, \tag{2.66}$$

---

[5]The integral converges only if $D[U] + m$ is positive definite. Therefore, one usually replaces it by the genuine two flavor operator $D^\dagger D$, which is always positive definite.

where $O_i = O[U_i]$ is the observable obtained in the configuration U_i. This correlation function is only dependent on the time separation between two configurations and, hence,

$$C(O_i, O_{i+t}) = C_O(t). \tag{2.67}$$

The correlation falls of exponentially with the computer time t (Monte Carlo time), which leads to the definition of the *exponential autocorrelation* time

$$C_O(t) \propto C_O(0) \exp \left\{ -\frac{t}{\tau_{O,\exp}} \right\}. \tag{2.68}$$

The autocorrelation times differ for each observable, but it is in general not easy to determine autocorrelation times accurately. One is forced to make more or less crude estimates and, in order to avoid unwanted statistical correlations, usually the longest autocorrelation time is taken and only configurations, which are separated by several autocorrelation times, are used for the final measurements. One finds empirically that the longest autocorrelation time is usually related to the topology of the underlying gauge field. This will be discussed in the next chapter.

3

Topology and Lattice QCD

Nonperturbative methods are needed to investigate the topology of gauge fields. One possibility is to develop phenomenological models of the QCD vacuum which are related to the topological structure. Lattice QCD, in turn, is based on first principles. The problem is, however, that one cannot uniquely define topology on a lattice because any configuration can be transformed to the trivial one without passing through forbidden configurations (e.g. configurations with infinite action).

Nevertheless, there are remnants of the continuum topology if the lattice spacing is small enough. In this case it is possible to classify the gauge configuration by a discretized version of the topological charge. Action barriers are found between configurations with different topological charges and one has to pass through configurations which are less likely in an importance sampling to overcome these barriers. With decreasing lattice spacing (and decreasing mass) these barriers grow and we approach a continuum-like situation with infinitely high barriers.

This chapter starts with a discussion of various definitions of the topological charge on a space-time lattice and the lattice version of the index theorem. Then we show some applications of topological concepts in Lattice QCD and close with filtering methods to extract the topological charge (density) from noisy Monte Carlo configurations.

3.1. Lattice definition of the topological charge

It is straightforward to obtain a formal expression for the topological charge density from Eq. (1.53) on a space-time lattice:

$$q_{\text{top}}^{\text{lat}}(x) = \frac{1}{16\pi^2} \operatorname{tr}\left(F_{\mu\nu}^{\text{lat}}(x)\widetilde{F}_{\mu\nu}^{\text{lat}}(x)\right), \qquad (3.1)$$

where $F_{\mu\nu}^{\text{lat}}(x)$ is a suitable discretization of the field strength tensor. The field strength tensor has already been mentioned when discussing the nonperturbative clover action. Now we have a closer look at it.

When deriving the Wilson gauge action in Sec. 2.1, we realized that the plaquette is related to the field strength tensor: $U_{\mu\nu}(x) = 1 + ia^2 F_{\mu\nu}(x) + \mathcal{O}(a^4)$. Therefore,

$$a^2 F_{\mu\nu}^{\text{lat}}(x) = \frac{i}{2} \left[(U_{\mu\nu} - U_{\mu\nu}^\dagger) - \frac{1}{N_c} \text{tr} \{ U_{\mu\nu} - U_{\mu\nu}^\dagger \} \right] + \mathcal{O}(a^2). \qquad (3.2)$$

The hermitian conjugate removes the unwanted constant on the r.h.s and the trace is subtracted to ensure the tracelessness of the field strength tensor.

Though being computationally very cheap, it is often impractical to use this definition for studying topological properties. Even for very smooth[1] configurations and fine lattices we often do not get values close to an integer total topological charge $Q_{\text{top}} = \sum q_{\text{top}}(x)$. Hence, we will use a more sophisticated definition, which was first introduced by Bilson-Thomson *et al.* [84]. In the spirit of the Symanzik improvement program (cf. Sec. 2.3) they suggested to add irrelevant operators which cancel $\mathcal{O}(a^n)$ contributions. The resulting field strength tensor can be written in a very general form as follows:

$$a^2 F_{\mu\nu}^{\text{imp}}(x) = \sum_i k_i C_{\mu\nu}^{m\times n} \Big|_{\text{herm. traceless}}, \qquad (3.3)$$

where we introduced the averaged *clover term* $C_{\mu\nu}^{m\times n}(x)$ of $m \times n$ Wilson loops starting at lattice site x:

and $|_{\text{herm. traceless}}$ denotes the hermitian traceless projection in analogy to Eq. (3.2). After choosing the desired order of improvement and the clover terms which should be included in the definition, one has to solve a system of algebraic equations to determine the coefficients k_i. A convenient choice is to use only symmetric 1×1, 2×2 and 3×3 Wilson loops in the sum of Eq. (3.3) which allows for an $\mathcal{O}(a^4)$-improved field strength tensor:

$$F_{\mu\nu}^{\text{imp}}(x) = k_1 C_{\mu\nu}^{1\times 1} + k_2 C_{\mu\nu}^{2\times 2} + k_3 C_{\mu\nu}^{3\times 3}, \qquad (3.4)$$

where the coefficients are determined to be [84]:

$$k_1 = 1.5, \qquad k_2 = -0.15 \qquad \text{and} \qquad k_3 = 1/90. \qquad (3.5)$$

The improved field strength $F_{\mu\nu}^{\text{imp}}$ defines an improved topological charge density

$$q_{\text{top}}^{\text{imp}}(x) = \frac{1}{16\pi^2} \text{tr} \left(F_{\mu\nu}^{\text{imp}}(x) \widetilde{F}_{\mu\nu}^{\text{imp}}(x) \right). \qquad (3.6)$$

---

[1]"Smoothness" is not uniquely defined in this context.

This definition is called the gluonic or field theoretic definition of the topological charge density. It can be calculated very effectively on a lattice, but there is still one drawback. Though giving almost integer topological charge $Q = \sum_x q(x)$ on smooth gauge configurations, one gets ambiguous results for Q on typical Monte Carlo configurations. Short-range fluctuations of the gauge field dominate the measurement and one needs efficient ways to remove these fluctuations. Some of these filtering methods will be discussed at the end of this chapter.

3.2. Index theorem on the lattice

The importance of the Atiyah-Singer index theorem has been discussed at length in Sec. 1.3. It relates the topological charge of the gauge fields to the index of the Dirac operator (difference of zero modes with positive and negative chirality):

$$Q_{\text{top}} = \text{index}(D) = n_L - n_R. \tag{3.7}$$

Both sides of this equation are, however, ambiguous on the lattice: The topological charge Q_{top} is not (exactly) equal to an integer, as discussed above, and there are no chiral zero modes for Wilson or staggered fermions or any other non-chiral fermion.

This conceptual problem does not occur for Ginsparg-Wilson fermions. Solutions of the Ginsparg-Wilson relation D_{GW} have either exact zero modes with definite chirality

$$D_{\text{GW}}\psi_0 = 0 \qquad \Rightarrow \qquad \gamma_5\psi_0 = \pm\psi_0, \tag{3.8}$$

or nonzero modes without chirality

$$D_{\text{GW}}\psi_\lambda = \lambda\psi_\lambda \qquad \Rightarrow \qquad \gamma_5\psi_\lambda = 0. \tag{3.9}$$

This property allows for a new definition of the topological charge [39]:

$$Q_{\text{top}}^{\text{ferm}} \equiv \text{index}(D) \overset{(2.35)}{=} \frac{1}{2}\,\text{Tr}\{\gamma_5 D\} = -\frac{1}{2}\,\text{Tr}\{\gamma_5(2-D)\} \tag{3.10}$$

where the trace (with capital "T") runs over spin, color and lattice indices and where we have used that $2-D$ has an index with opposite sign of D. This looks similar to the index theorem, but the gist is completely different: We define the fermionic topological charge via the index, which is strictly integer on any gauge configuration.

From the definition Eq. (3.10) it is straightforward to obtain an expression for the fermionic topological charge density if one takes the trace only over spinor and color indices [39]:

$$q^{\text{ferm}}(x) \equiv \frac{1}{2}\,\text{tr}\{\gamma_5(2-D(x,x))\} = \sum_\lambda (1-\frac{\lambda}{2})\langle\psi_\lambda(x)|\gamma_5|\psi_\lambda(x)\rangle. \tag{3.11}$$

While the global topological charge is entirely determined by the zero modes, the non-zero modes contribute to the local density, as $\langle\psi_\lambda(x)|\gamma_5|\psi_\lambda(x)\rangle \neq 0$. Moreover, it can be shown that [39]

$$q^{\text{ferm}}(x) = \frac{1}{16\pi^2}\,\text{tr}\left(F_{\mu\nu}(x)\widetilde{F}_{\mu\nu}(x)\right) + \mathcal{O}(a^2) \tag{3.12}$$

for sufficiently smooth configurations. Therefore, this provides an elegant definition of the topological charge in lattice simulations.

Though being a nice and well studied quantity, we want to close this section with some cautionary remarks on this definition. The Ginsparg-Wilson relation does not have a unique solution and, in general, each solution has a different spectrum. Accordingly, we will get consistent results only for sufficiently smooth configurations [39]. Even if we specify a certain solution, which is usually done by using the overlap operator, we are left with the freedom to choose the mass parameter in the kernel operator. Different mass parameters yield a different local structure and might change the global topological charge [85, 86]. This ambiguity will always be present as long as the configurations are not generated with a dynamical chiral Dirac operator, which would fix the remaining parameter.

As a side remark we want to add that any acceptable discretization of the Dirac operator with good chiral properties exhibits remnants of this index theorem. The zero eigenvalues of the continuum Dirac operator will only move slightly away from zero, but they remain real and no other near-zero eigenvalues will appear [39]. Thus, it is possible to identify these quasi-zero modes on the lattice with zero modes in the continuum. These modes have either positive or negative chirality, though not exactly $+1$ or -1 and, due to this property, we are able to relate them to the index and the topological charge.

For other Dirac operators one can find similar definitions which use some kind of projection of low lying modes to "chiral zero modes". The chirally improved Dirac operator, for instance, has complex eigenvalues, which come in conjugate pairs and real eigenvalues. The eigenvectors of the complex eigenvalues obey

$$\sum_{\lambda \neq 0, x} \langle \psi_\lambda | \gamma_5 | \psi_\lambda \rangle = 0, \tag{3.13}$$

while for real modes this quantity is approximately but not actually equal to ± 1. Correspondingly, one can achieve an integer topological charge by rescaling the contribution of the real quasi-zero modes to the sum in (3.11):

$$q_{CI}^{\text{ferm}}(x) = \sum_{\lambda, \text{ complex}} (1 - \frac{\lambda}{2}) \langle \psi_\lambda(x) | \gamma_5 | \psi_\lambda(x) \rangle + \sum_{\lambda, \text{ real}} \frac{1}{|\rho_{5,\lambda}|} \langle \psi_\lambda(x) | \gamma_5 | \psi_\lambda(x) \rangle, \tag{3.14}$$

where we have introduced the chirality of the eigenmodes

$$\rho_{5,\lambda} = \sum_x \langle \psi_\lambda(x) | \gamma_5 | \psi_\lambda(x) \rangle. \tag{3.15}$$

Rescaling of the eigenmodes with the latter ensures that each mode contributes either $+1$ or -1 to the topological charge, depending on the sign of its chirality. Other modes only modify the topological structure, but not the global charge.

The fermionic and the gluonic definition have both been used with great success in various research fields. Some of these are presented in the following.

3.3. Topology in Lattice QCD

There are many different research topics in Lattice QCD, which are related to topology. We will concentrate on those topics which are relevant for our work.

3.3.1. Autocorrelation in Monte Carlo simulations

The QCD vacuum is thought to be a superposition of distinct vacua with different topological charges, this is why a gauge field ensemble should sample the configuration space in an appropriate manner, which means that one should get a Gaussian distribution of the topological charge centered around $Q_{\mathrm{top}} = 0$.

Tunneling between two different topological sectors in a Markov chain is not easy. Small changes of the gauge field do not alter the global charge and large changes have a bad acceptance rate in the Metropolis accept/reject step. This situation becomes worse, when aiming for smaller lattice spacings and lighter fermion masses. In these cases one faces the problem that the simulation gets stuck in a topological sector. Accordingly, the autocorrelation time of the topological charge τ_{top} increases dramatically. This may lead to a wrong distribution of the topological charge and, hence, to incorrect results for physical observables which are not necessarily connected to topology. This effect is also known as the *critical slowing-down* of topological modes.

The origin of this slowing-down can be explained qualitatively in a very simple manner: In the continuum Q_{top} is invariant under smooth deformations due to an action barrier separating different topological sectors. At finite lattice spacing and for a finite volume we can overcome this barrier, but it increases for decreasing lattice spacing. As a consequence one has to pass through configurations with very large action to change the topological sector in a Monte Carlo update. This is, however, related to a large error of the numerical integration of the equations of motion and the new configuration is likely to be rejected.

An example for the evolution of the topological charge for the Wilson gauge action is shown in Fig. 3.1. The configurations are generated with a HMC algorithm with a relatively short trajectory length. The space of configurations is sampled in a rather slow manner, resulting in a step-like behavior of the topological charge. Physical observables could be biased in this situation, leading to wrong results. As a consequence it is of high importance to get a good estimate of the autocorrelation, not to underestimate the statistical errors [87].

The topological charge is among the observables with the largest autocorrelation times and serves as a good measure for the quality of an ensemble. This is the reason why modern simulation algorithms are designed to increase the transition probability between topological charge sectors.

3.3.2. Simulations at fixed topology

A rather new approach to Lattice QCD are simulations at fixed topology, i.e., simulations where the topological charge does not change at all. According to the arguments
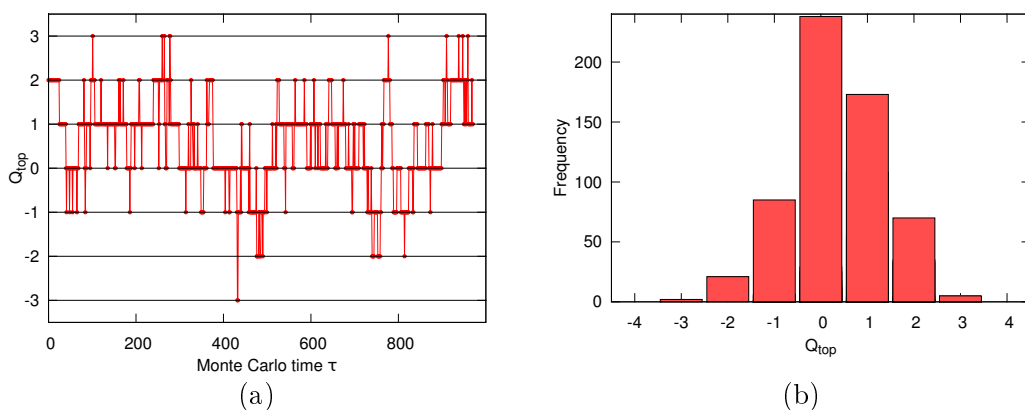
(a)

(b)

Fig. 3.1: Typical evolution of the topological charge during a Monte Carlo simulation (a) and its distribution in this ensemble (b). The configurations were generated with a HMC algorithm (16^4 lattice, Wilson gauge action, $\beta = 6.18$, which corresponds to $a \approx 0.07\,\text{fm}$). The topological charge has been measured by the index of the overlap operator. The step-like structure of the topological charge indicates a rather slow sampling of the configuration space. As a net effect one would measure a nonvanishing expectation value of Q_{top} and any measurement (of a physical observable) may be biased towards a wrong result.

in the previous section this seems quite odd, but one can show that the additional error for physical observables at fixed topology is proportional to the inverse volume and, hence, it will vanish in the infinite volume limit (see Ref. [88] and Ref. [89] for an explicit calculation). This effect can be qualitatively explained as follows: An infinite volume will include subvolumes with different net topological charge. Therefore, a spatial averaging includes also an average over topological sectors.

Many modifications of gauge actions have been proposed to fix topology (see, for instance, Refs. [90, 91, 92]), but to no avail. The first approach which could fix it completely was suggested by Fukaya *et al.* [93]. They introduced an additional determinant ratio in the path integral

$$\frac{\det\left(D_W^2(M)\right)}{\det\left(D_W^2(M) - \mu^2\right)}, \tag{3.16}$$

where $D_W(M) = D_W - M$. This factor corresponds to an additional heavy particle with mass M and an associated twisted mass ghost. It turns out that this determinant suppresses configurations with small eigenvalues. Topology on the other hand, can only change if a near-zero eigenvalue pair becomes an unpaired zero eigenvalue.

A very important effect of this suppression is an enormous speedup of Monte Carlo algorithms, as the condition number[2] of the Dirac operator is drastically improved. This results in a numerically much cheaper inversion of the Dirac operator which is need in the HMC algorithm. Although one has to spend some extra time to compute

---

[2] The condition number is the ratio of the largest and the smallest eigenvalue.

the determinant of a huge matrix, it is still less expensive than inverting an operator with small eigenvalues.

There are many open questions concerning ergodicity, autocorrelation and instanton physics in this approach. Nevertheless, fixed topology simulations draw more and more attention. Even reliable dynamical overlap simulations seem feasible within this approach [94, 95, 96]. First results are promising, but these studies do not yet include the crucial infinite-volume extrapolation.

3.3.3. Topological susceptibility and two-point function

Topology is not only of technical interest. There are physical quantities which are strongly related to it. As mentioned in Chap. 1, there is no ninth would-be Goldstone boson, the η', due to the chiral anomaly and topological excitations.

Witten and Veneziano [97, 98] found, under certain assumptions (e.g., large-N limit), that the topological susceptibility

$$\chi_{\text{top}} = \int d^4x \, \langle q(x)q(0) \rangle \tag{3.17}$$

of the quenched theory fulfills

$$\chi_{\text{top}}^{\text{quen.}} = \frac{f_\pi^2}{2N_f} \left(m_\eta^2 + m_{\eta'}^2 - 2m_K^2 \right), \tag{3.18}$$

where f_π is the pion decay constant. The masses of the kaon and the η-particle vanish in the chiral limit ($m_{u,d,s} \to 0$) and the r.h.s. of Eq. (3.18) reduces to

$$\chi_{\text{top}}^{\text{quen.}} = \frac{f_\pi^2}{2N_f} m_{\eta'}^2. \tag{3.19}$$

The strange thing about the Witten-Veneziano formula is that each side has to be evaluated in a different theory. The l.h.s. has to be determined in pure gauge theory (infinite quark mass limit), because the topological susceptibility vanishes for any number of massless flavors (cf. [30]), whereas, the r.h.s. is evaluated in the chiral limit.

Despite the conceptual problems of the interpretation of this relation, it has been shown that the Witten-Veneziano formula is in good agreement with experimental data. Taking the experimentally measured masses yields

$$\chi_{\text{top}} = \frac{f_\pi^2}{2N_f} \left(m_\eta^2 + m_{\eta'}^2 - 2m_K^2 \right) \Big|_{\text{exp}} \approx (180\text{MeV})^4. \tag{3.20}$$

This value has been confirmed in many Lattice QCD simulations using different actions and different definitions of the topological charge (cf. Tab. 3.1).

There are two basic strategies to measure the topological susceptibility. One can measure it directly according to Eq. (3.17) on each configuration followed by an ensemble average or one can use that

$$\chi_{\text{top}} = \frac{\langle Q^2 \rangle}{V}. \tag{3.21}$$

	$\chi_{\mathrm{top}}^{1/4}[\mathrm{MeV}]$
Dürr *et al.* (2007) [99]	193(1)(8)
Del Debbio *et al.* (2005) [100]	191(5)(8)
CP-PACS (2001) [101]	197(4)(12)
UKQCD (1998) [102]	187(14)(16)

Tab. 3.1: Results for the topological susceptibility from different publications. The first error contains all statistical errors and the second error is due to the uncertainty of setting the physical scale on the lattice.

Hence, it can also be determined directly from the distribution of the global topological charge in the ensemble. The latter option is usually preferred for its simplicity and precision.

Another quantity of interest is the two-point correlation function of the topological charge density $\langle q(x)q(0)\rangle$, which is the integrand of the topological susceptibility. This function is obviously related to the distribution of the topological charge and contains important information on the underlying structure of the QCD vacuum. The two-point function has some very special properties, which will be discussed in the following [103, 104]. It is well known that $q \propto F\tilde{F}$ is odd under time reversal, so $\langle q(x)q(0)\rangle$ has to be negative for $|x| > 0$ in order to satisfy reflexion positivity. Otherwise no valid continuum limit would exist (Osterwalder-Schrader condition [105, 106]). The topological susceptibility, in turn, is positive (or zero) and, correspondingly, a positive contact term (for $|x| = 0$) has to cancel the negative contribution to the space-time integral of Eq. (3.17). The shape of this correlator on the lattice and how to measure it will be discussed in Chap. 7.

3.3.4. Topological objects on the lattice

So far we have only discussed global properties of topological structures like the topological charge. While the concepts related to such global quantities are quite settled, we need more sophisticated methods for analyzing the local topological structure. There are two essential problems: First of all, the discretization on a lattice introduces multiple scales which limit the translation of continuum objects to the lattice. The $SU(2)$-instanton solution, for instance, depends on the size parameter ρ_{inst}:

$$\mathrm{A}_\mu^I(x) = \sum_a \mathrm{A}_\mu^a(x)\frac{\sigma_a}{2} = \sum_a \eta_{a\mu\nu}\frac{2x_\nu}{x^2 + \rho_{\mathrm{inst.}}^2}\frac{\sigma_a}{2}. \tag{3.22}$$

Translating this expression to a lattice by the usual parallel transporter

$$U_\mu(x) = \mathcal{P}\exp\left\{-i\int_x^{x+\hat{\mu}}\mathrm{A}^I(s)ds\right\} \approx e^{-ia\,\mathrm{A}_\mu^I(x)} \tag{3.23}$$

is only valid for $a \ll \rho_{\mathrm{inst.}} \ll L$. While this is the natural hierarchy of any observable on the lattice, an additional problem arises. The basic property of the instanton solution
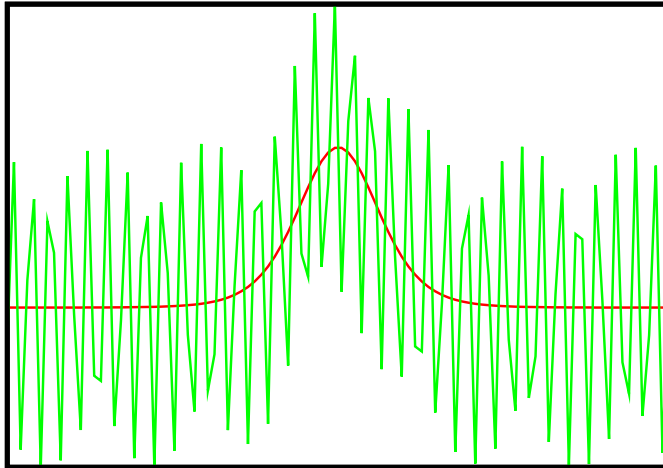
Fig. 3.2: Long-range structure, e.g. a topological object, hidden by short-range fluctuations (cf. [107]).

is lost: namely an integer topological charge. This is certainly not unexpected, as discretization errors will always be introduced, but these can be so big that the resulting object cannot be interpreted in terms of instantons. It can be seen best in the extreme case of $\rho_{\text{inst.}} = a$ (strongly localized object). If the object is placed at the center of a hypercube, we will "loose" it in the discretized version, yielding $Q_{\text{top}} \approx 0$ instead of approximately 1.

The second fundamental problem is related to the Monte Carlo simulation. The most natural thing would be to study the topological charge density directly with the lattice definition Eq. (3.1). The resulting density is, however, strongly affected by short-range fluctuations of the gauge field and, therefore, very large gluon momenta. These fluctuation make a direct identification of the underlying topological structure impossible. Thus, methods to filter out the relevant degrees of freedom are needed.

This issue has been nicely illustrated by de Forcrand [107] (see Fig. 3.2): The topological excitations are some kind of background excitations, which can be revealed after removing the ultraviolet noise. This is, however, much more complicated than the visualization suggests. A simple Fourier decomposition or wavelet transformation of the scalar density does not yield the correct result and more sophisticated methods are needed to do this filtering.

3.4. Filtering methods

It has been pointed out that we need some kind of filtering when analyzing the topological structures in Monte Carlo configurations. This section introduces some of the most common filtering algorithms, thereby covering all methods which have been used in this thesis.

3.4.1. Cooling

Cooling [108, 109] has been the first method to reduce short-range fluctuations from Lattice QCD configurations. The basic idea behind this procedure is to locally minimize the action. To this end, one replaces each link by an element of the gauge group that minimizes the action. In the case of the Wilson gauge action this corresponds to maximizing the plaquette:

$$U_\mu(x) \to \max_{U_\mu(x)} \left(\mathrm{Re}\,\mathrm{tr}\{U_\mu(x)\Sigma(x)\} \right), \qquad (3.24)$$

where $\Sigma(x)$, also known as *staple*, is made up of the links residing around the plaquette.

This update can be applied sequentially (sweeping through all links of the lattice) or in parallel (update of all links at the same time). If all links are replaced according to the above prescription, one speaks of a single cooling step. An iterative application of cooling reduces the action in every step and the configuration is driven to a classical minimum of the action.

Cooling has been widely used in lattice studies of the QCD vacuum. There are, however, some fundamental problems related to this procedure. Instantons, which are solutions of the classical equation of motion (and, hence, minima of the classical action), are not stable under cooling in the long run. It is easy to show that the finite lattice spacing artifacts of the gauge action cause instantons to shrink and fall through the lattice (see e.g. Ref. [110]). As a consequence, many variants have been proposed, which use different gauge actions or additional terms in $\mathrm{Re}\,\mathrm{tr}\{\ldots\}$, which reduce finite lattice spacing artifacts (cf. Refs. [111, 110]). In addition, there is a problem concerning short cooling runs, i.e., for only a few updates: If one throws away the original link variable, it is *a priori* not clear what information is lost and in this context cooling is a very drastic modification of the gauge fields. Cooling is not used in this thesis. Nevertheless, all methods, which are based on manipulating the links, share these problems to some extent. Such filtering procedures are usually referred to as "smearing" methods.

3.4.2. APE smearing

One of these link-based filtering methods is *APE smearing* [112, 113]. The main idea is to replace each link variable by a weighted sum of itself and the attached (forward) staples:

$$U_\mu(x) \longrightarrow U_\mu(x) + \gamma \sum_{\mu \neq \pm\nu} U_\nu(x)U_\mu(x+\hat\nu)U_\nu^\dagger(x+\hat\nu), \qquad (3.25)$$

where γ is a weighting factor. The new link is not a member of the gauge group anymore and so it has to be projected it back onto the group. Before we discuss this projection in more detail, we can write down the defining equation of a single APE smearing update:

$$U_\mu^{\mathrm{APE}}(x) \equiv P_{SU(N_c)}\left\{ (1-\alpha_{\mathrm{APE}})U_\mu(x) + \frac{\alpha_{\mathrm{APE}}}{6} \sum_{\mu \neq \pm\nu} U_\nu(x)U_\mu(x+\hat\nu)U_\nu^\dagger(x+\hat\nu) \right\}. \quad (3.26)$$

α_{APE} is called smearing parameter and determines the filtering strength and $P_{SU(N_c)}$ denotes the projection back to the gauge group. For this parameterization of the smearing parameter one has two special cases. If $\alpha_{\mathrm{APE}} = 0$, we get the original link and if $\alpha_{\mathrm{APE}} = 1$, we have no contribution of the old link.

We use the "standard parameter" $\alpha_{\mathrm{APE}} = 0.45$ throughout this thesis (this value corresponds to a ratio link-to-staple of $7 : 1$). It has been shown that this value provides the best matching to RG-cycling, a smoothing method based on renormalization group techniques [114, 115, 116]. Other choices are possible and the resulting configurations will depend on this parameter. It will also strongly depend on the number of sequential APE smearing steps and, consequently, one has to use this method with great care not to introduce method-dependent artifacts.

The main problem of APE smearing is the projection. For the special cases of $U(1)$ and $SU(2)$ a simple rescaling can be applied but, in general, there is no unique projection. One usually searches for the group element U, that satisfies

$$P_{SU(N_c)}\{W\} = \max_{U \in SU(N_c)} \left(\mathrm{Re}\,\mathrm{tr}\{U^\dagger W\} \right). \qquad (3.27)$$

This projection relates APE smearing to cooling: Taking $\alpha_{\mathrm{APE}} = 1$ we throw away the contribution of the original link and the projection minimizes the plaquette action locally. For a smaller smearing parameter, we will preserve information from the original link and, thus, APE smearing is less harmful than cooling.

3.4.3. Stout smearing

Stout smearing [117, 118] solves the problem of the projection in a more elegant manner. The construction of the smeared link is straightforward and we will present it for $SU(N)$-valued links. The starting point is the weighted sum over the staples attached to the link $U_\mu(x)$ denoted by $C_\mu(x)$:

$$C_\mu(x) \equiv \sum_{\pm\nu\neq\mu} \rho_{\mu\nu}\Sigma_\nu(x) = \sum_{\pm\nu\neq\mu} \rho_{\mu\nu}\left(U_\nu(x)U_\mu(x+\hat\nu)U_\nu^\dagger(x+\hat\nu) \right) \qquad (3.28)$$

The coefficients $\rho_{\mu\nu}$ are tunable parameters which determine the strength of the filtering. Defining $\Omega_\mu(x) \equiv C_\mu(x) \cdot U_\mu^\dagger(x)$, where no summation is performed, one can construct the matrix

$$Q_\mu(x) = \frac{i}{2}\left(\Omega_\mu^\dagger(x) - \Omega_\mu(x) \right) - \frac{1}{2N_c}\,\mathrm{tr}\left\{ \Omega_\mu^\dagger(x) - \Omega_\mu(x) \right\}, \qquad (3.29)$$

or in a rather symbolic notation:

This matrix is hermitian and traceless and in this case iQ is an element of the $\mathfrak{su}(N_c)$ algebra. Every element of the algebra can be uniquely mapped to a group element of $SU(N_c)$ via the exponential map $e^{iQ_\mu(x)}$ and accordingly, $e^{iQ_\mu(x)}U_\mu(x)$ remains in $SU(N_c)$. Finally, a recursive procedure for $n+1$ steps of stout smearing is defined by:

$$U_\mu^{(n+1)}(x) = \exp\{iQ_\mu^{(n)}(x)\}U_\mu^{(n)}(x) \qquad \text{and} \qquad U_\mu^{(0)}(x) = U_\mu(x). \tag{3.30}$$

It is not immediately obvious why this iteration leads to a smoothing of the fields, but one can show that stout and APE smearing are equal to lowest order in lattice perturbation theory for a single smearing step [119].

Another interpretation of the stout smearing algorithm is based on the so-called *Wilson flow* [120, 121, 122]. This flow defines an evolution of the gauge fields in an artificial time τ (the "flow time") according to the flow equation

$$\partial_\tau V_\mu(x,\tau) = -1/\beta\big(\partial_{x,\mu}S_W[V_\mu(x,\tau)]\big)V_\mu(x,\tau) \qquad \text{with} \qquad V_\mu(x,0) = U_\mu(x), \tag{3.31}$$

where S_W is the Wilson gauge action[3] with the plaquette replaced by 1×1 clover terms and $\partial_{x,\mu}$ its Lie-algebra-valued variation with respect to the link variable $V_\mu(x,\tau)$. Due to the minus sign, the action decreases monotonically with the flow time, leading to smoother and smoother gauge fields. Stout smearing can be obtained by solving the flow equations using the Euler method with a time step $\delta\tau = \rho_{\text{stout}}$. Successive iterations lead again to smoother gauge fields.

3.4.4. Improved stout smearing

Stout smearing and APE smearing behave very similar to cooling for a large number of iterations. It is well known that both smearing methods will destroy instantons for a sufficient number of iterations. Therefore, it has been proposed by the authors of [124] to modify the matrix Q in (3.30) by using larger 2×1 loops in addition to the usual 1×1 loops. The definition of their improved stout smearing reads as follows:

$$U_\mu^{\text{imp. stout}} = e^{iQ_\mu(U,\rho,\epsilon)}U_\mu, \tag{3.32}$$

where

---

[3]Other choices of the action, which are local and gauge invariant, lead to other flow definitions, coinciding with the Wilson flow in the continuum limit. See, for example [123], where the "Symanzik flow" has been proposed.

The additional smearing parameter ϵ determines the weight of the larger loops and, hence, the magnitude of the lattice artifacts. $\epsilon = 1$ yields the "usual" stout smearing and one can tune this parameter such that instantons are preserved in a wide range of their size parameter [124].

It has been found that the combination $\epsilon = -0.25$ and $\rho = 0.06$ yields the desired behavior. This is why we stick to these parameters throughout this thesis. A second reason to use this method (and the above parameters) is that there is a strong correlation of the field theoretic definition of the topological charge density after five steps of improved stout smearing and the fermionic definition including all eigenmodes of the overlap operator [125].

3.4.5. Laplace filtering

A substantially different method is *Laplace filtering* [126, 127, 128], which is based on a spectral decomposition of the links in terms of eigenmodes of the covariant lattice Laplacian

$$\Delta_{xy}^{ab} = \sum_{\mu=1}^{4} \left(U_\mu^{ab}(x)\delta_{x+\hat{\mu},y} + U_\mu^{ab\dagger}(y)\delta_{x-\hat{\mu},y} - 2\delta^{ab}\delta_{xy} \right), \tag{3.33}$$

where $a, b = 1, \ldots, N_c$ are color indices. The eigenvalue equation reads as follows:

$$-\Delta_{xy}^{ab} \cdot \Phi_n^b(y) = \lambda_n \cdot \Phi_n^a(x). \tag{3.34}$$

There are in total $N_{\text{total}} = N_x \times N_y \times N_z \times N_t \times N_c$ eigenvalues and eigenvectors. If all are known, the Laplacian can be written as:

$$-\Delta_{xy}^{ab} = \sum_{n=1}^{N_{\text{total}}} \lambda_n \Phi_n^a(x) \otimes \Phi_n^{b\dagger}(y). \tag{3.35}$$

This is nothing but the spectral decomposition of the Laplace operator, which always exists for a self-adjoint operator. Combining the definition (3.33) with Eq. (3.35) and using $y = x + \hat{\mu}$ yields

$$U_\mu^{ab}(x) = -\sum_{n=1}^{N} \lambda_n \Phi_n^a(x) \cdot \Phi_n^{b\dagger}(x+\hat{\mu}). \tag{3.36}$$

The eigenvalues are related to some energy scale (squared) and this is why the above relation can be used as a starting point for a low-pass filter in the sense of a Fourier decomposition.

If one truncates the sum in Eq. (3.36) at a small number of modes, one gets the filtered gauge fields U_μ^{Laplace}:

$$U_\mu^{\text{Laplace}}(x) = P_{SU(N_c)} \left\{ -\sum_{n=1}^{N} \lambda_n \Phi_n(x) \otimes \Phi_n^{\dagger}(x+\hat{\mu}) \right\} \quad \text{with} \quad N \ll N_{\text{Total}}. \tag{3.37}$$

In general, one does not get an element of the gauge group for the truncated spectral sum and so one has to project the resulting link onto an element of $SU(N_c)$. In the limit of all eigenmodes, no projection is needed because we recover the original link.

The problem of the definition Eq. (3.37) is that the weight for the lowest modes is quite small, while these modes are very important for the topological structure. We can cure this by using a symmetry of the lattice Laplacian, which connects the low and the high end of the spectrum. It has been found in Refs. [129, 130, 131] that

$$\Phi_{N_{\text{tot}}-n}(x) = (-1)^{\sum_\mu x_\mu} \Phi_n(x). \tag{3.38}$$

The prefactor is the staggered phase from Sec. 2.5. If we want to include the upper end of the spectrum in the filter, we have to reweight the links and replace:

$$-\lambda_n \to 16 - 2\lambda_n. \tag{3.39}$$

Although it seems quite odd to include also the highest modes for a low-pass filter, one gets better convergence properties of the filter, as the lowest modes will have the biggest weight. Finally, we get the defining equation for the Laplace filtered links:

$$U_\mu^{\text{Laplace}}(x) = P_{SU(N_c)} \left\{ \sum_{n=1}^{N} (16 - 2\lambda_n)\Phi_n(x) \otimes \Phi_n^\dagger(x + \hat{\mu}) \right\}. \tag{3.40}$$

These links can be used to measure any observable, such as the topological charge density.

3.4.6. Dirac filtering

Dirac filtering [132, 133, 134, 135, 136] is also based on a low-mode truncation. The fermionic topological charge density (cf. Eq. (3.10)) is defined as a sum over eigenmodes of a chiral Dirac operator. While zero modes determine the overall topological charge, the non-zero modes contribute to the local structure. It has been found that the lowest modes are localized and smooth. So it makes sense to truncate the sum over the eigenmodes in the fermionic definition of the topological charge (3.10) at the N-th lowest mode, to get a filtered topological charge density:

$$q_{\text{top}}^{\text{Dirac}}(x) = \sum_{n=1}^{N} \text{tr} \left(\frac{\lambda_n}{2} - 1 \right) \psi_n^\dagger(x) \gamma_5 \psi_n(x). \tag{3.41}$$

This fermionic filter has some crucial advantages. The total topological charge $Q = \sum_x q(x)$, for example, is always an integer and equal to the unfiltered charge. Moreover, there is a direct connection of topological objects to zero modes, which has been sketched in Sec. 1.3. While this is conceptually the "cleanest" definition of a filter, it faces an enormous computational challenge. The eigenmodes of a chiral Dirac operator, like the overlap operator, are very expensive to compute and one is limited to relatively small lattices and even then huge parallel computers are needed.

Fortunately, it has been found in Ref. [125] that there is a strong correlation of the local structures of the fermionic topological charge density (without filtering) and the improved gluonic charge density after 5 steps of improved stout smearing (for $\epsilon = -0.25$ and $\rho = 0.06$). As smearing is a local operation, we have only a linear scaling of the computational costs with the lattice volume and even state-of-the-art lattice ensembles are accessible with this method.

Finally, we want to remark that the global topological charge and the local (filtered) density depend on the mass in the kernel operator. This mass can be chosen freely (within certain bounds), which can influence the resolution of the overlap operator [39, 85]. This ambiguity can only be removed if the configurations are generated with dynamical overlap fermions, as the simulation fixes the mass parameter.

4

Comparison of filtering methods

In this chapter we systematically compare filtering methods used to extract topological structures from Lattice QCD configurations. Many different methods have been proposed since the advent of Lattice QCD. Among them are cooling, smearing, Laplace filtering and the fermionic definition of the topological charge via eigenmodes of a chiral Dirac operator (see Ref. 3.4 for an overview over filtering methods). Unfortunately, all these methods introduce ambiguities and new parameters, which may lead to wrong conclusions.

In order to get a coherent picture of the topological structure of the QCD vacuum, it is necessary to control or even remove these ambiguities. To this end, we use a systematical comparison of the topological charge densities resulting from different filtering methods. The analysis shows that APE and stout smearing yield very similar topological charge densities when the parameters are matched properly. To get a better control over the ambiguities of smearing, it is necessary to complement it by an independent filtering method. This is in our case Laplace filtering. The comparison clearly reveals that smearing has to be used with care not to destroy relevant topological objects.

Parts of this chapter have been published in Ref. [2] and Ref. [5].

4.1. Measure for the local similarity

For a quantitative comparison of the local topological structure resulting from different filtering methods a measure of the similarity is needed. To this end, we have applied the method of Bruckmann *et al.* from Ref. [137]. They introduced the following quantity as a measure of the local similarity of two topological charge densities:

$$\Xi_{\mathrm{AB}} \equiv \frac{\chi^2_{\mathrm{AB}}}{\chi_{\mathrm{AA}}\,\chi_{\mathrm{BB}}}. \tag{4.1}$$

	lat. size	lat. spacing [fm]	β_{LW}	$\mathbf{m}_\pi$[MeV]	$\mathbf{N_{conf}}$
quenched	$16^3 \cdot 32$	0.148	7.90	–	80
dynamical	$16^3 \cdot 32$	0.150	4.65	~ 500	30

Tab. 4.1: Details on the gauge configurations used for this comparison. Further information can be found in Ref. [138]

χ_{AB} is the correlator of two topological charge densities $q_\mathrm{A}(x)$ and $q_\mathrm{B}(x)$

$$\chi_{\mathrm{AB}} \equiv (1/V) \sum_x \left(q_\mathrm{A}(x) - \overline{q}_\mathrm{A} \right) \left(q_\mathrm{B}(x) - \overline{q}_\mathrm{B} \right). \qquad (4.2)$$

where the mean topological charge $\overline{q} = Q/V$ is subtracted for various reasons. One consequence of this subtraction is that one gets rid of (or at least minimizes) possible additive renormalizations of the lattice topological charge density. Furthermore, considering two charge densities one of which is strongly structured and one is flat ($q(x) = const. = \overline{q}$), an exactly vanishing correlation is achieved. Without the subtraction, one would get a nonvanishing correlation.

Ξ_{AB} is by definition a positive quantity and equals one if the densities differ only by a constant scaling factor. It deviates the more from one, the more the densities differ. The great advantage of this definition is that one does not have to know the (additive and multiplicative) renormalization factors of the topological charge densities, since these factors drop out in Eq. (4.1) and one is able to compare the relative difference at each lattice point.

For a further quantitative analysis of the local topological structure resulting from different filtering methods A and B, it is useful to define 'best matching' pairs of filter parameters, by maximizing Ξ_{AB} (cf. Ref. [137]). In order to find these maximal values, we keep the APE and stout smearing parameters constant ($\alpha_{\mathrm{APE}} = 0.45$ and $\rho_{\mathrm{stout}} = 0.075$; see above) and compute Ξ_{AB} for up to 50 smearing steps each. Moreover, we compare the filtered topological charge densities obtained with up to 500 Laplace modes and 50 APE smearing steps. More smearing steps have not been applied, as too much smearing will destroy the local topological structure, whereas more Laplace modes would be too expensive.

We do this measurement for a dynamical and a quenched ensemble which have been generated with the Lüscher-Weisz gauge action [44, 45, 48, 49] and a chirally improved Dirac operator with two mass degenerate light quarks (see Sec. 2.5) [79, 138]. Both ensembles have almost the same lattice spacing and the same physical volume (cf. Tab. 4.1), to make the results comparable.

4.2. APE vs. stout smearing

We first discuss the matching of APE and stout smearing, see Fig. 4.1. In the absence of smearing (lower left corner) one has $\Xi = 1$ as the configurations are identical. An interesting observation is that the maximal values of Ξ lie on some kind of ridge, where
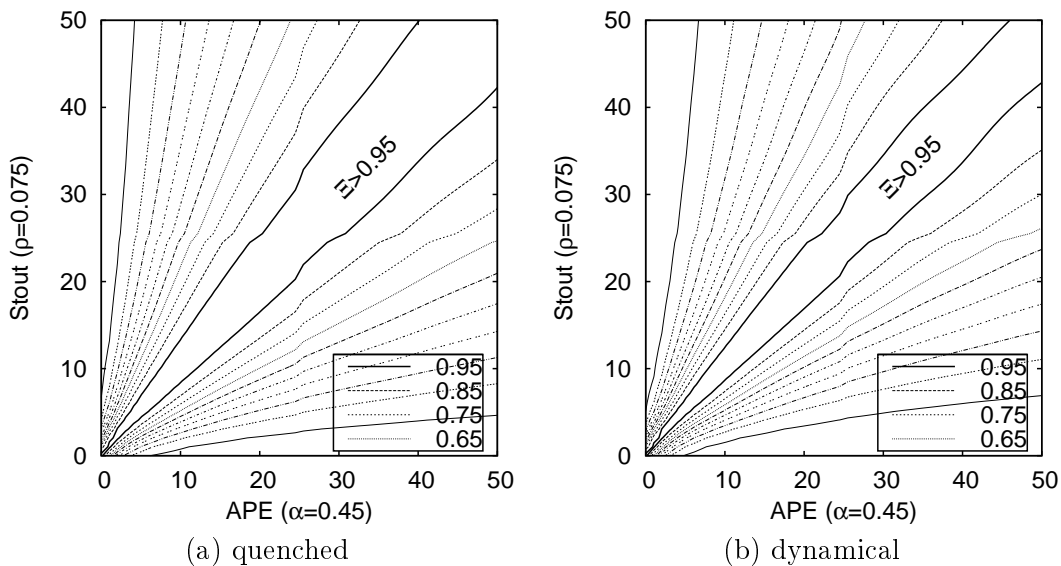
Fig. 4.1: Comparison of APE with stout smearing for quenched (left) and dynamical (right) configurations. The degree of similarity Ξ (see the definition (4.1) is given by contour lines. Both plots show a pronounced "ridge" of best matching pairs of smearing steps. Depicted are mean values of 80 quenched and 30 dynamical configurations, respectively (from Ref. [2]).

$\Xi > 0.95$ within our range of smearing steps. Thus, the different smearing techniques reveal almost the same structures. The slope of this line is determined by the ratio of the smearing parameters.

An almost one-to-one correspondence for the topological density after the same number of APE and stout smearing steps (i.e. a slope of 1) is achieved when the smearing parameters are related as $\alpha = 6 \cdot \rho$ [5]. This is consistent with the perturbative result of Ref. [119] and with the nonperturbative result from Ref. [139]. The latter focused on rather global observables, which are not related to topology, with up to three smearing steps. Our nonperturbative result reflects the local similarity of both methods and their strongly correlated topological charge densities up to 50 steps.

The described equivalence applies to both dynamical and quenched configurations. There are, however, quantitative differences. The ridge is slightly thinner in the dynamical case and, therefore, the structures seem to be more sensitive to the level of filtering. This can also be seen if we compare the values of Ξ for the best matching pairs of both methods (values of Ξ on the diagonal of both plots) as shown in Fig. 4.2. Within the first few smearing steps we find that the agreement gets worse. The reason for this is that the 3-loop definition of the field strength tensor needs sufficient smooth gauge fields in order to produce a stable result. Furthermore, both methods may remove UV contributions differently. Then the agreement gets better and after a few steps a plateau is reached where $\Xi \sim 0.995$. This plateau is quite stable for quenched
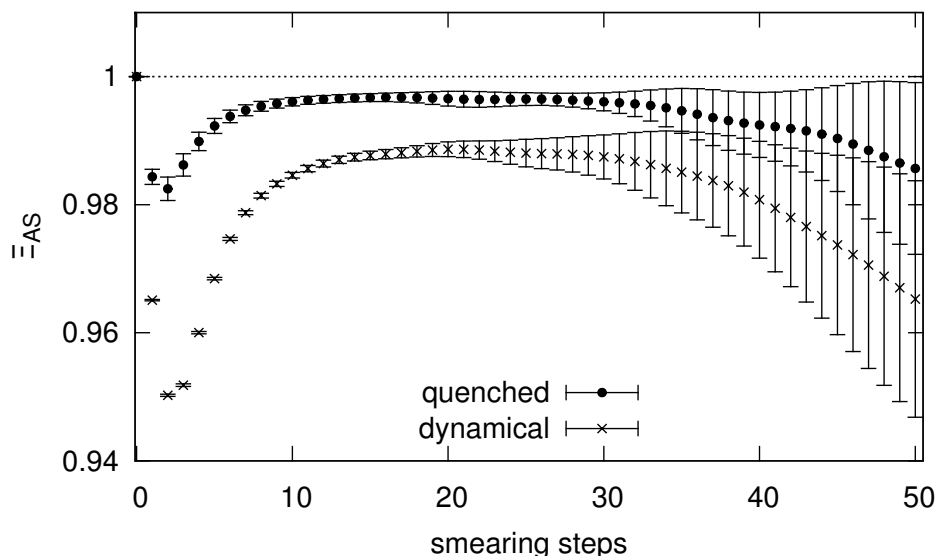
Fig. 4.2: Ξ for an equal number of APE and stout smearing steps. This corresponds to the values on the diagonal of Fig. 4.1. For the very weak and strong filtering case, the APE-stout smearing correspondence is slightly worse in the dynamical case and less stable for stronger filtering. Errors result from an ensemble average over 80 quenched and 30 dynamical configurations, respectively.

configurations until it starts to break down after 40 smearing steps. This behavior is very similar to the dynamical case. Nevertheless, the absolute values of Ξ are lower and the plateau breaks down after fewer steps (~ 30 steps).

This observation has some important practical consequence for the study of topological structures. If two almost equal methods like APE and stout smearing give different results, we cannot be sure which artifacts are introduced by the single method and so one should apply less than 20-30 smearing steps not to introduce too many artifacts, but more than 4 steps, in order to have a well-behaved improved field strength tensor. These numbers, however, might only hold for topological observables and can strongly differ for others.

4.3. Laplace filtering

APE and stout smearing are deeply related and this is why we need an independent method like Laplace filtering (see Sec. 3.4.5). Both methods are based on completely different principles and one could ask if they reveal similar structures at all. To this end, we show in Fig. 4.3 a slice of the topological charge density for a quenched configuration after 7 APE smearing steps and for 500 Laplace modes. Ξ is approximately 0.85 for these parameters and this means that both methods yield structures which are not only qualitatively but also quantitatively almost the same and it makes sense to do a
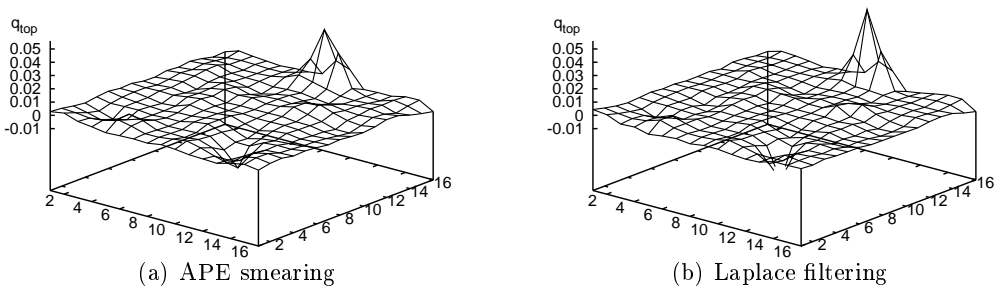
(a) APE smearing   (b) Laplace filtering

Fig. 4.3: Comparison of the same slice of the topological charge density resulting from 7 APE smearing steps (a) and 500 Laplace modes (b) (from Ref. [2])
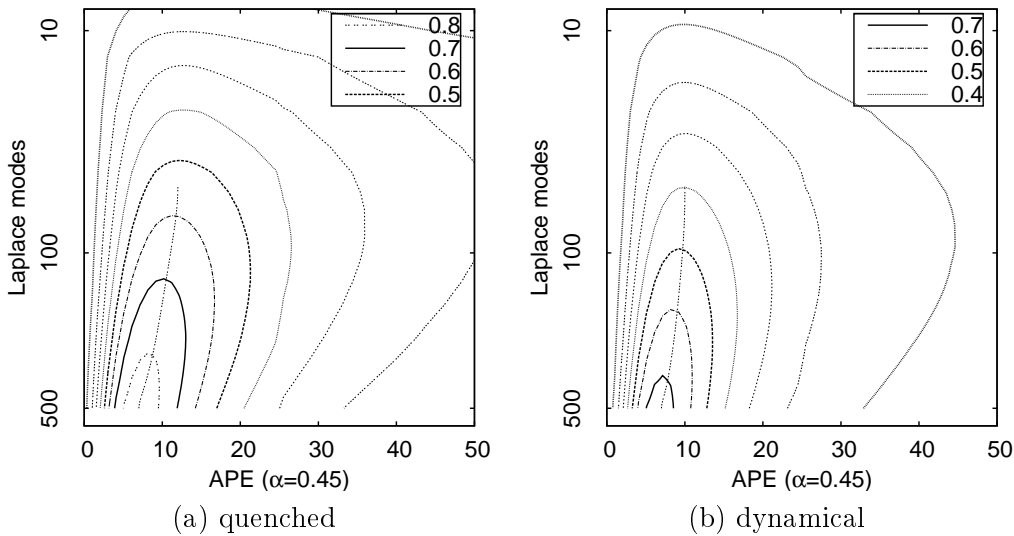

(a) quenched   (b) dynamical

Fig. 4.4: Comparison of APE smearing with Laplace filtering for quenched and dynamical configurations. The degree of similarity Ξ (see the definition (4.1)) is given by contour lines. The values of Ξ are in general lower than for the matching of APE and stout smearing in the previous section and the quantitative difference between quenched and dynamical configurations is bigger. For mild filtering we have plotted a line along the best matching parameter that will be used for the cluster analysis in the next chapter. Shown are mean values of 30 configurations each (from Ref. [2]).

systematic comparison.

We computed Ξ for up to 500 Laplace modes and 50 APE smearing steps ($\alpha_{APE} = 0.45$) on a dynamical and a quenched ensemble with 30 configurations each. The result can be found in Fig. 4.4. Again, we find some kind of ridge of the best matching values of Ξ. This ridge is quite pronounced for weak filtering, but it is hard to identify the best matching parameters in the strong-filtering regime, i.e. for less than 50 Laplace modes and more than 20 smearing steps. Furthermore, there is no set of best match-

modes	steps	$\Xi_{\mathbf{AL,quen}}$		modes	steps	$\Xi_{\mathbf{AL,dyn}}$
500	7	0.86		500	7	0.74
450	7	0.85		450	7	0.73
400	8	0.83		400	8	0.70
350	8	0.82		350	8	0.69
300	9	0.80		300	8	0.67
250	9	0.78		250	9	0.64
200	10	0.75		200	9	0.61
150	10	0.72		150	9	0.57
100	11	0.66		100	10	0.50
75	12	0.61		75	10	0.46
50	12	0.55		50	10	0.40

(a) quenched   (b) dynamical

Tab. 4.2: Best matching pairs of filter parameters for Laplace filtering and APE smearing ($\alpha_{\mathrm{APE}} = 0.45$). The values of Ξ have been rounded to two decimal places. The error from the ensemble average was below 0.006 in all cases.

ing parameters with $\Xi > 0.5$ in this regime and, thus, one can hardly say that both methods agree at all. The matching of quenched and dynamical configurations yields qualitatively the same result. The absolute values are, however, significantly lower in the dynamical case which could mean that there are more artifacts from a single method.

The cross-correlator Ξ_{AB} is just one method to characterize the similarity of two topological landscapes. In order to support our results we use an additional measure of the similarity: the *relative point overlap* (RPO) [137]. To this end, one cuts the densities such that the volume fraction[1] above the cutoffs are equal (in general, one needs different values for the cutoff for each method to get the same volume fraction) and then we identify those points that are common to both methods and have the same sign of the topological charge. This leads to the following definition of the RPO:

$$s_{\mathrm{AB}} = \sum_{\substack{x \in X_{\mathrm{A}} \cap X_{\mathrm{B}} \\ q_{\mathrm{A}}(x) q_{\mathrm{B}}(x) > 0}} 1 \Big/ \sum_{x \in X_{\mathrm{A}} \cup X_{\mathrm{B}}} 1 \,, \qquad (4.3)$$

where $X_{\mathrm{A/B}}$ is the set of lattice points x with topological density above the cutoff $|q_{\mathrm{A/B}}(x)|$. A value s_{AB} close to one signals a good agreement between q_{A} and q_{B}.

The values of the RPOs of APE and stout smearing (7 iterations each) as well as for APE smearing and Laplace filtering (7 iterations vs. 500 Laplace modes) are shown in Fig. 4.5. For APE and stout smearing we get a large RPO. This also stresses the similarity of the two methods. The RPO for APE smearing and Laplace filtering is

---

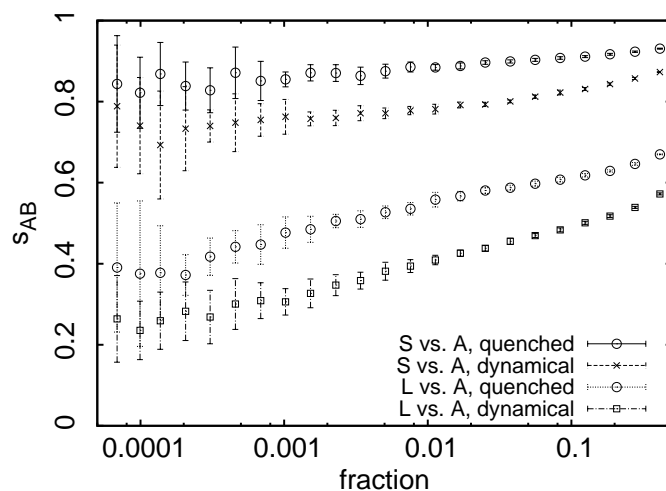[1]The volume fraction is the number of lattice points relative to the total number of points

Fig. 4.5: Relative point overlap s_{AB} (see Eq. (4.3)) of APE and stout smearing (7 iterations each) as well as for APE smearing and Laplace filtering (7 iterations vs. 500 Laplace modes) averaged over 10 configurations each (from Ref. [2]).

smaller and comparable to its values found for quenched $SU(2)$ configurations [137] and the tendency of less agreement in the case of dynamical configurations can be confirmed.

5

Cluster analysis of the topological charge density

In order to obtain information about the topological structure of the QCD vacuum, which can be compared to continuum models, we analyze the cluster structure of the topological charge density after mild filtering. To get rid of artifacts of a single filtering method, we use a combined analysis of smearing and Laplace filtering on both quenched and dynamical configurations. This combined analysis shows that the topological charge density is more fragmented in the presence of dynamical quarks.

The majority of this chapter has been published in Ref. [2].

5.1. Topological charge density clusters

In principle, there are many different ways to define a cluster on a lattice. We have chosen the following: Two lattice points belong to the same cluster if they are nearest neighbors and have the same sign of the topological charge density[1]. For such clusters Bruckmann *et al.* had found an interesting power-law dependence in quenched $SU(2)$ lattice gauge theory [137]. To that end, one cuts the absolute value of the topological charge density at a variable cutoff q_{cut} and determines the number of clusters $N_{\mathrm{cluster}}(q_{\mathrm{cut}})$ above this cutoff as a function of the total number of points above q_{cut}, $N_{\mathrm{points}}(q_{\mathrm{cut}})$. Fig. 5.1 shows a three-dimensional visualization of this procedure. One can distinguish three different phases when lowering the cutoff. First, the highest peaks of the topological charge density are found. In this case every new point either forms a separate cluster or belongs to a cluster of a very strong peak. This corresponds to the first three snapshots of Fig. 5.1. The number of revealed clusters depends strongly on

---

[1]Alternative definitions may also include lattice points at distances $\sqrt{2}a$ or $\sqrt{3}a$ (see, e.g., Ref. [140])

$N_{\text{points}} = 2 \; N_{\text{clust.}} = 2$ $\quad N_{\text{points}} = 15 \; N_{\text{clust.}} = 9$ $\quad N_{\text{points}} \approx 75 \; N_{\text{clust.}} \approx 50$

power law I $\qquad\qquad$ power law II $\qquad\qquad$ percolation

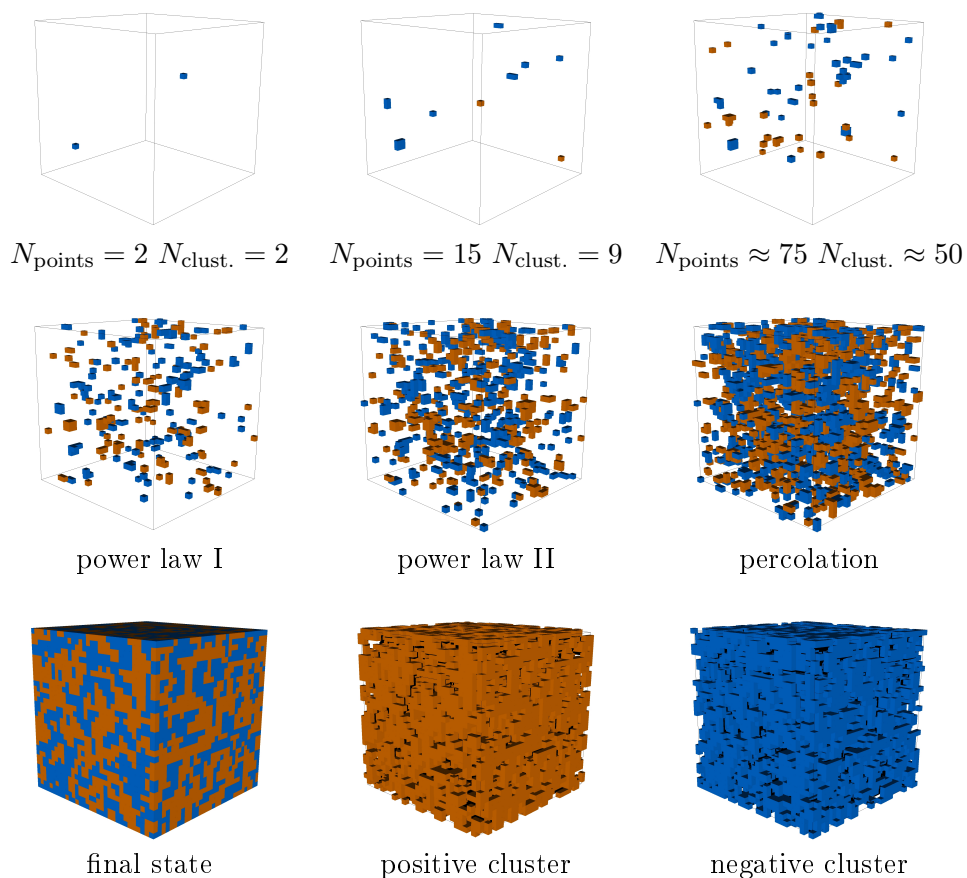final state $\qquad\qquad$ positive cluster $\qquad\qquad$ negative cluster

Fig. 5.1: Three-dimensional visualization of the cluster analysis with orange and blue representing positive and negative topological charge density. There a three different phases. For a high cutoff (first row) one finds the peaks, which depend on the single field configuration. At lower cutoff one has a phase which is governed by a power law for the cluster number and in the last stage at very low cutoff the clusters percolate, i.e., all positive and negative clusters merge and form two connected clusters with opposite charge (in four dimensions).

the considered gauge configuration. As a consequence, we have large deviations of the cluster number within an ensemble of gauge configurations. For a sufficiently large number of points above the cutoff, one is very sensitive to the general topological structure and the number of clusters follows a power law [2, 137]. In this regime one can extract the exponent with high accuracy. Finally, the clusters start to percolate and form two connected clusters with opposite sign of the topological charge (there are usually a few very small isolated clusters, consisting of 1-5 points which are just artifacts without any physical meaning). This behavior cannot be visualized in a three-dimensional scheme. In four-dimensional space with periodic boundary one can interpret this behavior as a sign of self-intersection and the fractal nature of the topological charge density (see
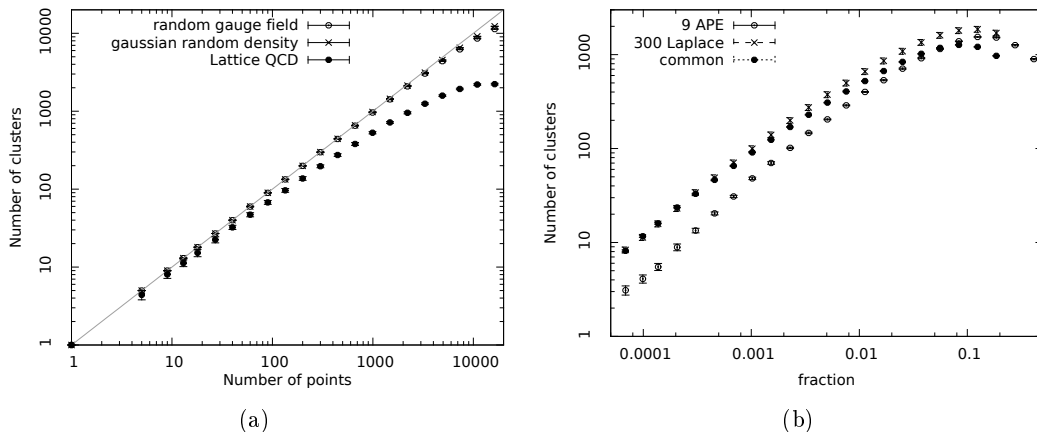
Fig. 5.2: (a) Number of topological clusters as a function of the number of points above a variable cutoff for a random gauge field, a random density and a typical Lattice QCD ensemble (The points for the random configurations lie on top of one another). While the random configurations show no clustering, we find deviations for Lattice QCD ensembles. (b) Number of clusters as a function of the fraction of all points above a variable cutoff for clusters after smearing and Laplace filtering as well as for clusters which are common to both methods (averaged over 30 dynamical configurations). The exponent of the underlying power law is highly characteristic for the topological structure and directly related to the size distribution of topological objects (from Ref.[2]).

Ref.[141] for a recent study of the fractal nature).

The exponent of the power law

$$\xi \equiv \frac{\mathrm{d}\big(\log N_{\mathrm{clust}}(q_{\mathrm{cut}})\big)}{\mathrm{d}\big(\log N_{\mathrm{points}}(q_{\mathrm{cut}})\big)}. \tag{5.1}$$

is highly characteristic for the topological structure of the QCD vacuum. Different models lead to different predictions. This allows for a sensitive test.

Some examples for the number of clusters as a function of the number of point above the cutoff can be found in Fig. 5.2(a). The result for the topological charge density of an ensemble of random gauge fields and a density with Gaussian distributed values has been included. Both yield an exponent very close to one, which corresponds to the solid line in Fig. 5.2(a). The reason for this behavior is quite obvious: Neighboring points are not correlated and, hence, every point forms its own cluster. Additionally, we included the result of a typical Lattice QCD configuration. Due to correlations in the QCD vacuum we get an exponent smaller than one. The size of the exponent depends on the topological structure in the vacuum, but also on the filtering method and the filtering strength and so it is essential to use these filters in a controlled way not to destroy the underlying structures.

The great advantage of a cluster analysis is that it allows to reduce ambiguities coming from a single filter. To this end, we take only those clusters into account which are
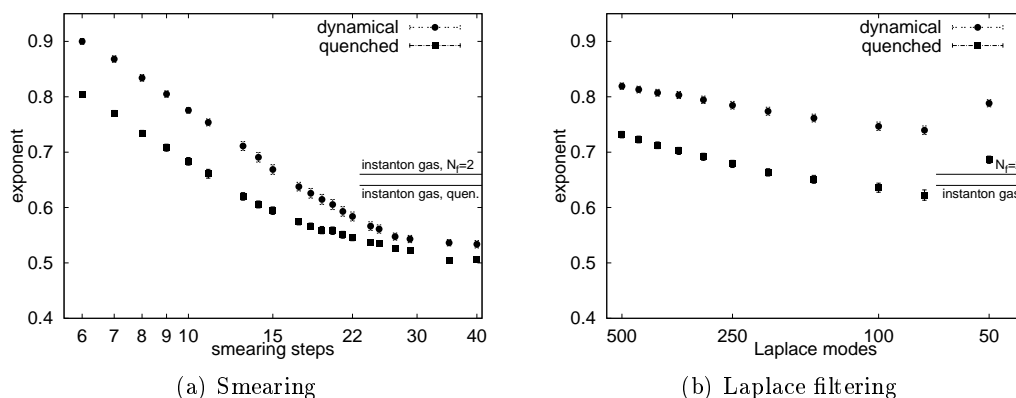
(a) Smearing   (b) Laplace filtering

Fig. 5.3: Exponent ξ for the clusters found by smearing and Laplace filtering. Both plots show the tendency of a higher exponent for dynamical configurations. The exponents predicted by the dilute instanton gas have been included in both plots. Errors from the ensemble average have been included, but are partly too small to be seen (from Ref. [2]).

common to different filters. If there is an artifact coming from one method, it is unlikely that this artifact will also be seen by the other one, such that the common structures are almost free of ambiguities. In order to increase the overlap of two methods, we perform this analysis after having matched the filtering parameters as described in the previous chapter. An example for the cluster analysis of different methods include a matched analysis can be found in Fig. 5.2(b).

The exponent can be further related to the size distribution $d(\rho) \sim \rho^\beta$ of topological objects with arbitrary shape function and dimensionality d. According to Ref. [137] one finds

$$\xi \equiv \frac{\mathrm{d}\big(\log N_{\mathrm{clust}}(q_{\mathrm{cut}})\big)}{\mathrm{d}\big(\log N_{\mathrm{points}}(q_{\mathrm{cut}})\big)} = \frac{1}{1 + d/(\beta + 1)}. \tag{5.2}$$

This expression enables a very simple comparison of model predictions and lattice simulations. For a dilute gas of instantons, for instance, one finds that $\beta = \frac{1}{3}(11N_c + N_f) - 5$ [26, 30] and $d = 4$, as instantons are four-dimensional objects. For the gauge group $SU(3)$ one gets $\xi = 0.64$ in the quenched case and $\xi = 0.66$ for two flavors of dynamical quarks.

Moreover, it is also possible to make a general statement on the topological objects without assuming any model: The closer the exponent is to one, the more suppressed are small objects. The average size of the objects, however, can shrink.

5.2. Cluster analysis for a single filter

First, we want to discuss the cluster analysis for smeared configuration. To this end, we use APE and stout smearing, where we have chosen the smearing parameters according

to the previous chapter. As we have shown, there is a deep relation between both methods and we can treat them as a single filtering method, although they are in principle two methods. The matching can easily be done, because of the one-to-one correspondence. We just have to take the same number of smearing steps and use those clusters/points which are found by both methods.

The exponent as a function of the smearing steps can be found in Fig. 5.3(a). The exponent decreases with increasing number of smearing steps, because the structures become smoother and, correspondingly, the correlation of neighboring lattice sites gets larger. Obviously, the exponents of the dynamical configurations lie above the quenched values at every step. This difference, however, vanishes for stronger smearing (~ 30 steps) and the exponents settle down to almost the same plateau. This is another indication that too much smearing destroys the impact of dynamical quarks on the vacuum structure.

In Fig. 5.3(b) the same analysis is done for Laplace filtering (only). The number of modes decreases from left to right and, hence, we have an increasing filtering strength. Again, stronger filtering leads to a smaller exponent. At first sight the value for 50 modes seems to be odd, as the exponents start to grow again, but this is an artifact of the incomplete reconstruction of the topological background. For a small number of modes, we get a very spiky structure. Lowering the cutoff reveals many new clusters and; as a result, a high exponent.

The difference of the exponents of dynamical and quenched configurations remains at every stage of filtering, but it is bigger than for smearing. Thus, we conclude that both methods have completely different artifacts and only a combined analysis gives results, which are almost free of ambiguities.

5.3. Matched cluster analysis

To get rid of the ambiguities of a single method, we perform a matched cluster analysis of APE smearing and Laplace filtering, i.e. we consider only those clusters, which are common to both methods. The result is shown in Fig. 5.4(a). We use the optimal set of filter parameters according to the maximal values of Ξ . These parameters correspond to points on the ridge of Fig. 4.4 and the values of Tab. 4.2, respectively. The best matching pairs are slightly different for dynamical and quenched configurations. In order to use a single plot, we use the Laplace mode number on the x-axis and give only the corresponding smearing steps for the quenched case.

The curves have a step-like behavior, as we have to match the same number of smearing steps to a large number of Laplace modes and the effect of using some modes more is much less than the effect of a single smearing step. In order to guide the eye, we interpolate the points with a smooth spline fit. This would correspond to a "continuous" smearing parameter.

As in Fig. 5.3 the values of the exponent in dilute instanton gases have been included. Generally, our measured values of the exponent are not far off the instanton gas values (which was not the case in $SU(2)$ [137]).
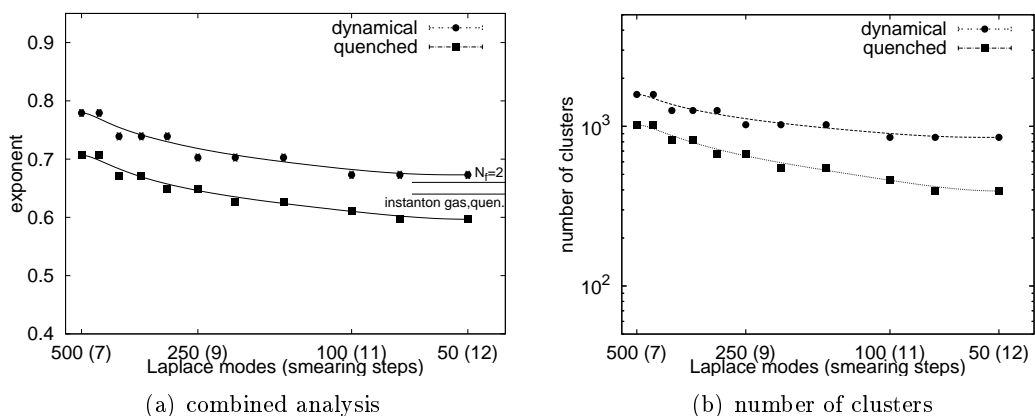
(a) combined analysis   (b) number of clusters

Fig. 5.4: Exponent ξ for the clusters found for a matched filtering of APE smearing and Laplace filtering. The measured exponents have a step-like behavior, because the number of smearing steps is an integer quantity and we have to match several numbers of Laplace modes to the same number of smearing steps. The smooth lines are interpolations corresponding to a "continuous" smearing parameter. The number of smearing steps (in parentheses) refers to the matching of quenched configurations and is slightly different for the dynamical case (cf. Tab. 4.2).(b) Total number of distinct clusters for a constant fraction $f = 0.0755$ of points lying above the cutoff with smooth interpolation (from Ref. [2]). Errors from the ensemble average are partly too small to be seen.

The main result of this analysis is that the cluster exponent is larger in the dynamical case. This can bee found in the analysis of a single filter as well as for a combined analysis of completely different filtering methods. According to the considerations from above, this implies a larger exponent β of the size distribution of the building blocks of the topological charge density. Hence, very small topological objects become suppressed when quarks are taken into account.

The power law itself contains only information on the size distribution of the objects and additional methods to quantify the topological structures have to be considered. One such quantity is the absolute number of clusters above a certain cutoff. To this end, one cuts the topological charge density such that the number of points above the cutoff is constant (We use 7.55 % of the total number of points) and counts the number of distinct clusters. This gives information on how the topological charge is distributed. In the dynamical case we find almost twice as many clusters at any level of filtering (see Fig. 5.4(b)). Hence, we observe a more fragmented topological structure in the presence of dynamical quarks.

Our findings can be compared to the results obtained by the Adelaide group [142]. They have observed an "increasing density of nontrivial field configurations" and a suppression of small instantons. Using a completely different approach, we come to the same conclusion. The advantages of our analysis are that our dynamical fermions have better chiral properties than the staggered ones. Moreover, we do not have to

postulate any shape function for the topological objects and, consequently, our method works for all topological building blocks and with our matched analysis we can obtain results which are almost free from ambiguities due to the filtering process.

This analysis was carried out at a single lattice spacing and with fermions possessing an approximate chiral symmetry. The question remains how chiral symmetry effects the topological structure and how the structures behave when we approach the continuum limit. This is our main focus in the following two chapters.

6

Dynamical overlap fermions

Simulations with chirally symmetric fermions are still one of the great challenges of Lattice QCD. The importance of chiral symmetry and its connection to topology has been discussed in the previous chapters. In the following we will give a short overview of the algorithmic details of our simulations with dynamical overlap fermions and discuss the topological properties of these configurations. We want to emphasize that there is a crucial difference with respect to other recent simulations with exact chiral symmetry [143]. These dynamical overlap simulations were carried out at fixed topology. We pursue a completely different strategy. The aim of our simulations is to reach the best possible tunneling rate between different topological sectors.

Parts of this chapter have been published in Ref. [1] and Ref. [4].

6.1. Details on the simulations

We have introduced in Sec. 2.4.3 the overlap Dirac operator which reads in a slightly different parametrization than before (and $a = 1$):

$$D_{\mathrm{ov}} = (1 + \mu) + (1 - \mu)\gamma_5 \operatorname{sign}(D_{\mathrm{ker}}), \tag{6.1}$$

where sign is the usual matrix sign-function and D_{ker} a suitable kernel operator like the Wilson Dirac operator and μ is a mass parameter.

The main algorithmic challenge of dynamical overlap simulations is the difficulty in changing the topological charge during the Monte Carlo history (cf. Sec. 3.3.1). The tunneling from one topological sector to another during the Monte Carlo history requires a discontinuous change in the action at all lattice spacings, which is in principle the same problem as in the continuum.

Changing topology becomes harder for most lattice discretizations as they approach the continuum limit. For overlap fermions, however, this challenge is present at any

lattice spacing. Therefore, new algorithms are needed in order to achieve the best possible tunneling rate between topological charge sectors.

Our configurations have been generated by using the transmission/reflection algorithm first proposed in Ref. [144] and refined in several subsequent papers [145, 146, 147, 148, 149, 150], together with the eigenvector differentiation algorithm proposed in Ref. [151], which is required to accurately differentiate near-degenerate pairs of eigenvectors whose eigenvalues lie close to a discontinuity.

The probability of changing the topological sector for this transmission/reflection algorithm depends on the discontinuity ΔS of the action. Unfortunately, a direct evaluation of ΔS is not possible and one usually uses pseudo-fermions to estimate the change in the action (see Sec. 2.6.2). Such an estimation is, however, not optimal and yields values which are much bigger than the actual change [145]. This problem gets even worse if we decrease the fermion mass as the estimated change of the action $(\Delta S_{\mathrm{pseudo-ferm.}} \sim \mu^{-2})$.

In order to improve the pseudo-fermion approach we factorize the determinant

$$\det D_{\mathrm{ov}} = \det \tilde{D}_{\mathrm{ov}} \det(D_{\mathrm{ov}}/\tilde{D}_{\mathrm{ov}}), \qquad (6.2)$$

where $\tilde{D}_{\mathrm{ov}}$ is the modified Dirac operator

$$\tilde{D}_{\mathrm{ov}} = (1+\mu) + (1-\mu)\gamma_5 \,\mathrm{sign}(D_{\mathrm{ker}} - \Lambda_0). \qquad (6.3)$$

Λ_0 is a real-valued parameter which is chosen according to a suitable probability distribution at the start of each HMC trajectory. The expression $\det \tilde{D}$ is continuous during the topological index change as there is no eigenvalue crossing zero for this operator. It can be estimated using pseudo-fermions[1], while the second term $\det(D_{\mathrm{ov}}/\tilde{D}_{\mathrm{ov}})$ can be calculated without pseudo-fermions

$$\det D = \det \tilde{D} \det(D/\tilde{D}) = \int [\mathcal{D}\,\phi][\mathcal{D}\,\phi^\dagger] e^{-\phi^\dagger(1/\tilde{D})\phi + \mathrm{tr}\log(D/\tilde{D})} \qquad (6.4)$$

The factorization leads to an exact estimate for the action discontinuity:

$$\Delta S = \Delta \log \det(D_{\mathrm{ov}}/\tilde{D}_{\mathrm{ov}}) = \Delta \log \det D_{\mathrm{ov}} = \Delta S_{\mathrm{exact}}. \qquad (6.5)$$

Therefore, we get the lowest possible discontinuity at a transition between different topological sectors and, in accordance, the optimal tunneling probability.

For the pseudo-fermion estimation of the determinant we need a positive definite operator D. The Dirac operator is not positive definite and, thus, one usually uses $D \to \sqrt{D^\dagger D}$ instead, at the cost of an expensive rational approximation for $(\sqrt{D^\dagger D})^{-1}$.

Using the Ginsparg-Wilson relation and γ_5-hermiticity one finds for overlap fermions with a mass parameter μ:

$$\det D_{\mathrm{ov}}[\mu] = \det A[\mu] \mu^{Q_{\mathrm{top}}^{\mathrm{ferm}}}, \qquad (6.6)$$

---

[1]We assume $\tilde{D}_{\mathrm{ov}}$ to be a positive definite operator.

Ensemble	trajectories	$\mathbf{a}[\,\text{fm}]$	$\mathbf{m}_\pi[\text{MeV}]$
A	>1000	$0.127(2)$	510
B	>400	$0.120(3)$	560
C	>600	$0.126(2)$	600

Tab. 6.1: Details on the dynamical overlap ensembles used in this thesis.

where $A[\mu]$ is the positive definite matrix

$$A[\mu] = \sqrt{2 + 2\mu^2} + \frac{1 - \mu^2}{2\sqrt{2 + 2\mu^2}}(1 + \gamma_5)\,\text{sign}(D_{\text{ker}})(1 + \gamma_5), \qquad (6.7)$$

and $Q^{\text{ferm}} = \text{index}(D)$ is the difference between the number of left- and right-handed zero modes of the corresponding Dirac operator. This definition makes it possible to run single-flavor simulations without the need of an expensive rational approximation.

The configurations used in this thesis result from three simulations of $12^3 \times 24$ lattices using a tadpole improved Lüscher-Weisz gauge action and a Wilson Dirac kernel with one step of improved stout smearing [124]. Though we can simulate individual quarks we choose two degenerate light quark masses. The strange quark mass in our 2+1 flavor simulation is tuned according to the QCDSF prescription [152].[2] The pion masses, which are restricted by the small lattice volume, were measured to be approximately 510 MeV, 560 MeV and 600 MeV, at lattice spacings of around 0.12 fm. Over 1000 trajectories were generated for the lightest pion mass and over 600 trajectories for the heavier pion masses. The details on the ensembles can be found in Tab. 6.1.

6.2. Autocorrelation

The autocorrelation of physical observables is one of the main issues of a Markov chain process. The topological charge is expected to have the largest autocorrelation time of all observables and this is why it is one of the central quantities to estimate the statistical significance of the measured data. As the autocorrelation increases strongly with decreasing fermion mass, we concentrate on the ensemble A which has the lightest fermion mass (cf. Tab. 6.1).

For this ensemble, there were on average 1.05 attempted topological index changes per trajectory, of which 37.5% resulted in a change of the topological index. This (naively) corresponds to one topological index change for every 2.8 trajectories of length $\tau = 0.5$. (This excludes trajectories where the topological charge changed twice or where the trajectory was rejected.) The Monte Carlo acceptance rate was around 85%. Values for the other $12^3 \times 24$ runs were similar.

This tunneling rate is, to the best of our knowledge, the highest ever achieved in this parameter region. However, the integrated autocorrelation time for the squared topological charge for the lightest mass ensemble was around 40 trajectories (of length

---

[2]Roughly speaking, we keep the sum of the three simulated quarks at their physical value.
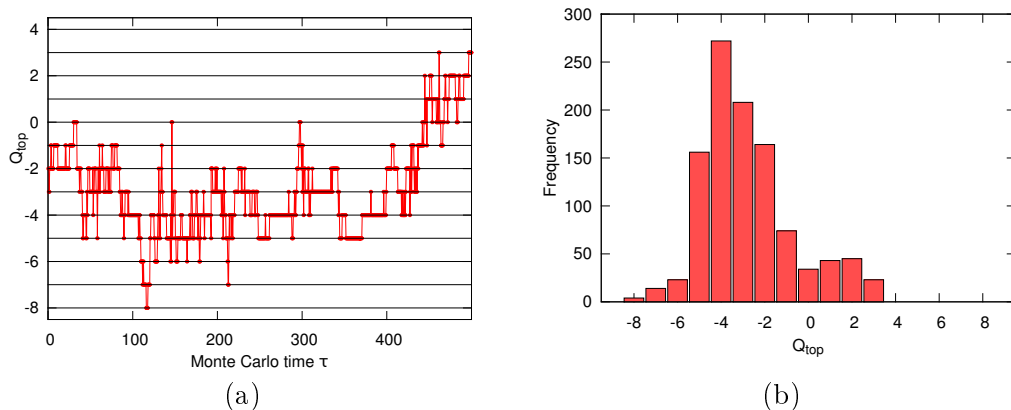
(a)

(b)

Fig. 6.1: (a) History of the index during the Monte Carlo evolution for ensemble A. (b) Distribution of the topological charge. Both plots show signs of inherent auto-correlation of the topological charge.

$\tau = 0.5$), compared to around 8 for the plaquette. This problem in global topological autocorrelation can be seen in Fig. 6.1. Although topological index changes occur commonly, the mean of the charge distribution is clearly negative. Accordingly, there are still problematic long term correlations for the topological charge.

The topological charge is a global quantity and it might be blind to local autocorrelations. Moreover, the definition of the integrated autocorrelation is ambiguous for short Monte Carlo histories [153, 37] and, thus, we introduce an additional measure of autocorrelation.

We use the cross-correlator of two charge densities Ξ which was defined in Eq. (4.1) and calculate it as a function of the trajectory number between subsequent configurations. The result for the ensemble A can be found in Fig. 6.2. The correlator falls off exponentially with increasing number of trajectories between two configurations. There are visible correlations for up to 80 trajectories and this correlation increases with increasing number of smearing steps. The dependence on smearing is just another indication of the relevance of topological modes in Monte Carlo simulations.

The correlations are visualized in Fig. 6.3 using isosurface plots of the topological charge densities for the same time slice after 20 steps of smearing. These plots show how the topological structures evolve as a function of the Monte Carlo time (configuration number). The good news is that we observe a weak autocorrelation of the structure for a large fraction of lattice points if there are more than 40 trajectories between the configurations. Nevertheless, there is one example of an object with a huge autocorrelation. A negative charged object appears in the bottom right corner of configuration 210 and persists for more than 100 trajectories. This structure seems to be very robust against (small) perturbations due to the pseudo-momentum field at the beginning of a molecular dynamics trajectory. We conclude from this observation that there are localized structures in the vacuum which dominate the autocorrelation of an
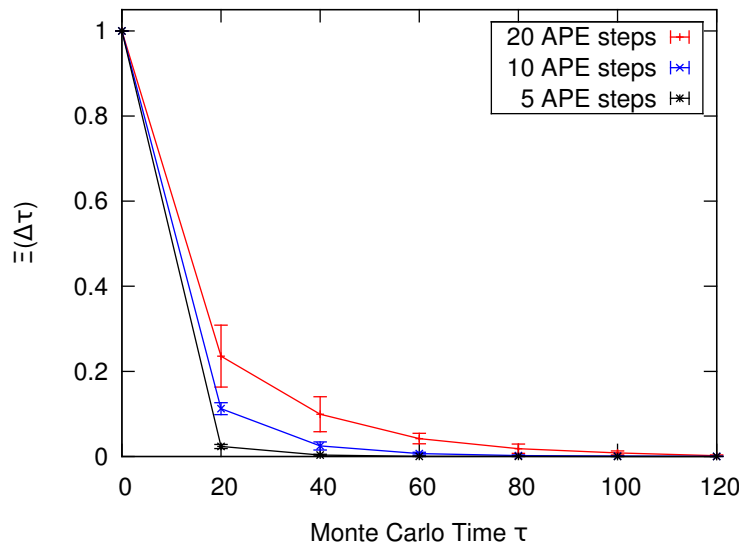
Fig. 6.2: Autocorrelation of the topological charge density for subsequent configurations in a Monte Carlo history. Ξ measures the local similarity of two topological charge densities. We find significant correlations for a separation of up 80 trajectories. For stronger filtering the correlation even increases. The errors result from an ensemble average.

ensemble.

Our new definition for the autocorrelation can also be a useful tool for lattice simulations at fixed topology. In this case we cannot use the integrated autocorrelation of the topological charge. Thus, we propose to use the local autocorrelation of the topological charge density, as defined above. This definition is straightforward to implement and yields much bigger values for the autocorrelation time than, e.g, the plaquette or large Wilson loops [3].

6.3. Index theorem

Dynamical overlap simulations have exact zero modes and an exact index. In previous studies of the index theorem on the lattice either would-be zero modes or overlap valence quarks have been used [154, 133, 155, 156]. The latter case seems to be free of ambiguities, but one has the freedom to choose the kernel operator which can result in a different index. Even different mass parameters for the same kernel operator can yield different results, as shown in Refs. [86, 85], where the effect of the mass parameter in the Wilson kernel has been studied. Only sufficiently smooth gauge configurations will have a consistent index (see Ref. [39] for a review).

Dynamical overlap configurations are free of this ambiguity. Only in that case one has an absolutely clean definition of the index as the mass parameter is fixed by the simulation. One can make use of this property in many different ways, like for the
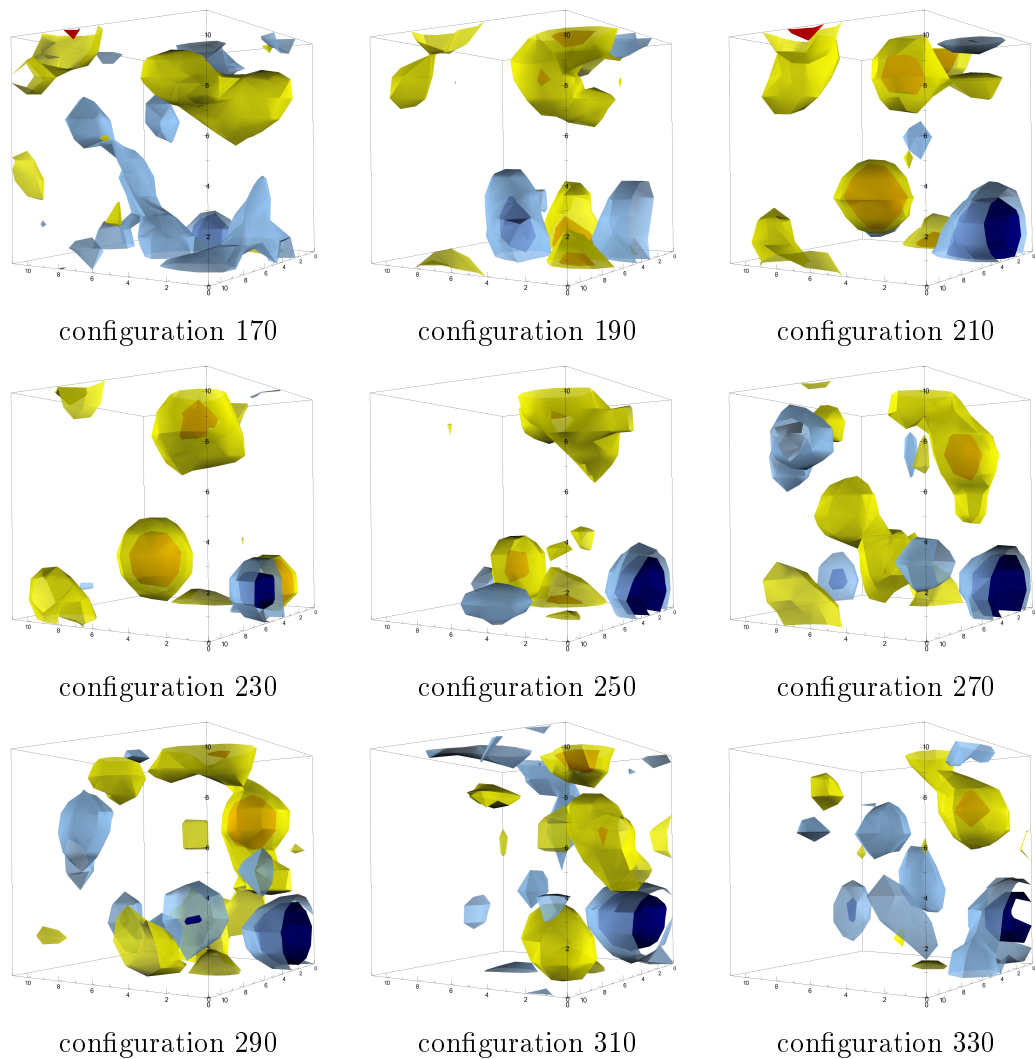
configuration 170   configuration 190   configuration 210

configuration 230   configuration 250   configuration 270

configuration 290   configuration 310   configuration 330

Fig. 6.3: The same time slice of the topological charge density after 20 APE smearing steps each for a sequence of configurations from ensemble A. The configurations show some local structures which have a very long autocorrelation within the Monte Carlo history. One example of such a structure is the negatively charged (blue) object in the bottom right which is created around configuration 210 and persists for many updates.

study of the index theorem for different smearing methods. To this end, we define the absolute deviation of the gluonic definition from the index as [3]

$$\Delta Q = Q_{\text{ferm}} - Q_{\text{top}}. \qquad (6.8)$$

Fig. 6.4 shows this quantity as a function of the smearing steps for APE, stout and improved stout smearing with the previously defined smearing parameters. Lines
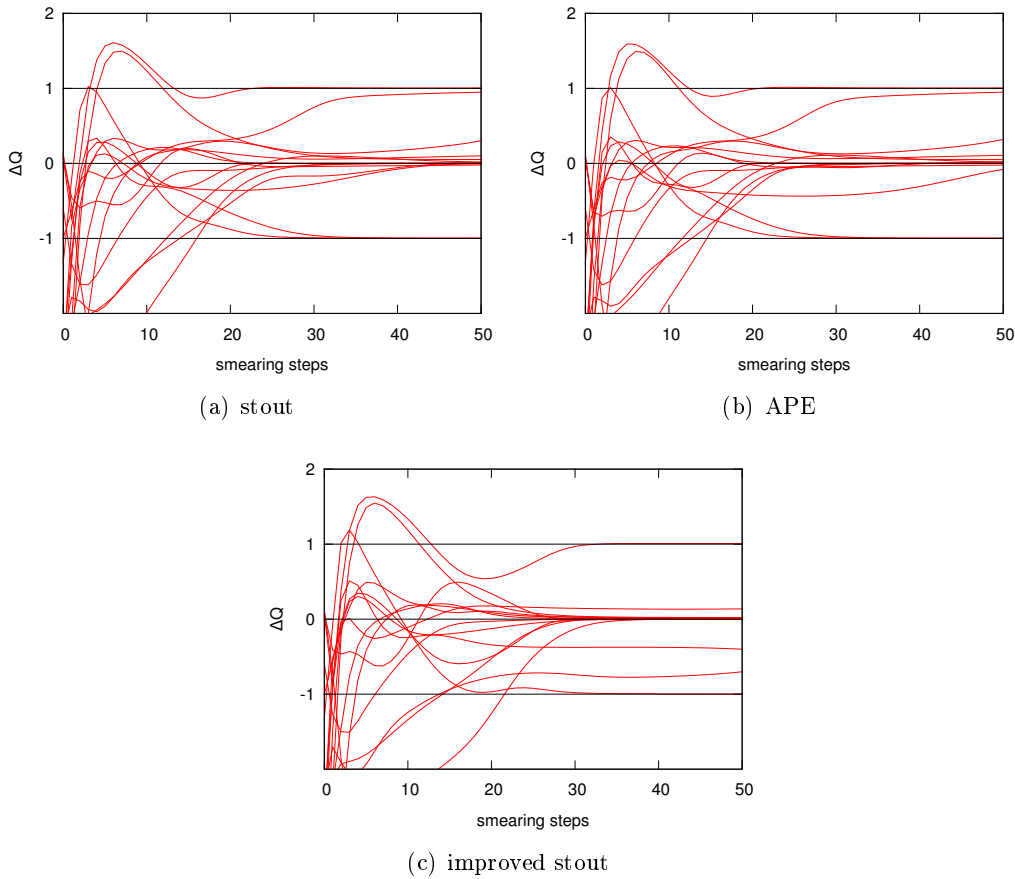
(a) stout

(b) APE

(c) improved stout

Fig. 6.4: Derivation of the improved gluonic definition of the topological charge from the exact index after different smearing methods. The lines should guide the eye, not to lose track of the single configuration. APE and stout smearing lead to very similar results, as expected from the results of the previous chapters. Improved stout smearing shows a very good agreement with the index theorem for the majority of configuration. There are, however, some outliers, which do not stabilize at an integer charge for up to 50 steps.

have been used in order to guide the eye and to keep track of the topological charge history of a single configuration and the same set of configurations has been used in all plots. An ideal filtering method would have $\Delta Q = 0$ for all filtering strengths, but this is not expected for our methods. Lattice artifacts spoil the results and topological objects can even be lost, which leads to large deviations from zero. The two obvious criteria for the quality of a filter are the absolute value of the deviation from zero for the single configuration and the number of configurations which miss the correct topological charge.

One finds in that improved stout smearing leads to the best agreement of both topological charge definitions, as it is designed to stabilize instanton-like solutions in the

long run. The number of configurations with an incorrect assignment of the topological charge does not show a significant difference between the methods, but more independent configurations are needed for a detailed analysis. Remarkably, one has more outliers which do not settle down to an integer charge within 50 smearing steps for the improved stout smearing. These configuration seem to be exceptional in some sense and it would be interesting to study these configurations in more detail.

Another possible application of our configurations would be to calibrate different filtering methods and their parameters in order to get the optimal agreement of the field theoretic and the fermionic definition of the topological charge. This could improve, for instance, the accuracy of the measurement of the topological susceptibility.

6.4. Status of the configurations

The available lattice spacings, lattice volumes and pion masses of our dynamical overlap configurations are still far from the values of conventional lattice simulations (for a review see, e.g., Ref. [157]), but these fermion actions spoil one of the fundamental symmetries of QCD and it is not known how harmful this is.

The tunneling rate between different topological sectors has improved a lot in the last few years and, as displayed in Fig. 6.3, the topological structure changes also locally. There are, however, structures with long autocorrelations and, therefore, one needs a large time separation in the Monte Carlo history to obtain independent configurations.

Taking everything into account, we can conclude that only a few really independent configurations are available to extract physics results. We have chosen a separation of 60 configurations as a compromise between getting a sufficient number of configurations and having small enough autocorrelation. Thus, we can only measure observables which do not need large statistics, we can qualitatively compare properties of single configurations and we can try to get information on phenomena, where even low-precision results could help, like for the axial vector coupling for negative parity nucleon states, where a discrepancy between Wilson fermions and chirally improved fermions has been found for the first excited states [158].

Fortunately, topology offers such observables, which have a high degree of self-averaging over a single configuration or a small ensemble (see next chapter). As a consequence, the available dynamical overlap simulations can serve as a benchmark for other simulations as long as the obtained data are interpreted with care.

7

Topology of dynamical lattice configurations

In this chapter we investigate how the topological charge density in Lattice QCD simulations is affected by the violation of chiral symmetry for different fermion actions. Topology is intimately connected to chiral symmetry, both through the $U(1)$ anomaly, giving mass to the η', and through the index theorem, linking fermionic zero modes to the topological charge. This is the reason why we believe that the topological charge density, although it is a purely gluonic quantity, is well-suited to test the effects due to violation of chiral symmetry for different fermion actions.

In this analysis we use the field theoretic definition of the lattice topological charge Eq. (3.6) and compare topological structures obtained after a few sweeps of improved stout smearing (cf. Sec. 3.4.4). This is applied to lattice configurations generated with a number of different actions including the dynamical overlap configurations from the previous chapter.

In a fist step we qualitatively compare visualizations of the topological profiles after mild smearing and then we compare the size of the positive core in the topological charge correlator and the amplitude of the contact term to reach more quantitative results.

The majority of this chapter can be found in our publications Ref. [1] and Ref. [4].

7.1. Lattice configurations

We use dynamical $N_f = 2$ and $N_f = 2 + 1$ flavor configurations from different fermion formulations. They are available through the International Lattice Data Grid (ILDG) [159] in a wide range of lattice spacings, lattice volumes and pion masses (more information on the ILDG can be found in the Appendix A.5.2).

fermion (gauge) action	N_f	$a[\,\mathrm{fm}]$	$V[a^4]$	$m_\pi[\mathrm{MeV}]$	N_{conf}	Ref.
twisted mass (Sym)	2	$0.10 - 0.063$	$24^3 48 - 32^3 64$	≈ 500	20	[160]
twisted mass (Sym)	2	$0.10 - 0.051$	$20^3 48 - 32^3 64$	≈ 280	20	[160]
np imp. clover (plaq.)	2	$0.11 - 0.07$	$24^3 48$	≈ 500	20	[161]
np imp. clover (plaq.)	2	$0.10 - 0.07$	$32^3 64$	≈ 250	20	[161]
asqtad staggered (LW)	2+1	$0.15 - 0.09$	$16^3 48 - 28^3 96$	≈ 500	5	[162]
chirally improved (LW)	2	0.15	$16^3 32$	≈ 500	20	[138]
top. fixed overlap (Iw)	2	0.12	$16^3 32$	≈ 500	20	[143]
dynamical overlap (LW)	2+1	$0.13 - 0.12$	$12^3 24$	≈ 500	15	[165]

Tab. 7.1: Configurations used in this chapter (abbreviations: Sym = Symanzik , plaq. = plaquette, LW = Lüscher-Weisz, Iw = Iwasaki).

The fermion actions in these simulations may be classified with respect to their chiral symmetry. Variants of Wilson fermions like twisted mass [160] and nonperturbative clover [161] break chiral symmetry explicitly (by a lattice artifact). Staggered fermion actions like asqtad [162] possess a remnant chiral symmetry. We also use chirally improved fermions[1], which are an approximate solution to the Ginsparg-Wilson relation [138], and as exact solutions we take overlap fermions with an extra topology fixing term [143] and the dynamical overlap fermions from the previous chapter. Additionally, we have generated quenched ensembles with the plaquette gauge action and the Iwasaki gauge action (cf. Chap. 2). The lattice spacings have been chosen to match those of the dynamical ensembles. To this end we have used the parameters according to the parametrization given in Ref. [163] and Ref. [164].

The details on the configurations can be found in Tab. 7.1. The pion masses for the configurations used vary between 250 and 500 MeV, which does not seem to be a major problem as little mass dependence is found. The lattice spacings range from 0.15 fm down to 0.051 fm for the finest lattices. For the asqtad staggered, the twisted mass and the nonperturbative clover fermions we had enough data to perform the limit $a \to 0$, while keeping the pion mass approximately constant. For the latter two we even had different sets at different pion masses.

7.2. Visualization

Before doing a quantitative comparison of the topological structures in different fermion simulations, we compare the structure in a more qualitative way. To this end, we plot three-dimensional slices of the topological charge density. A direct comparison of the profiles is only possible if the lattice spacings are similar because the densities strongly scale with a, namely as a^{-4}. Accordingly, we have a factor of almost two orders of magnitude between results for the coarsest and the finest lattice only from the lattice

---

[1]The chirally improved configurations are not available through the ILDG. They have been used in Chap. 4 and Chap. 5. Details can be found in Tab. 4.1.
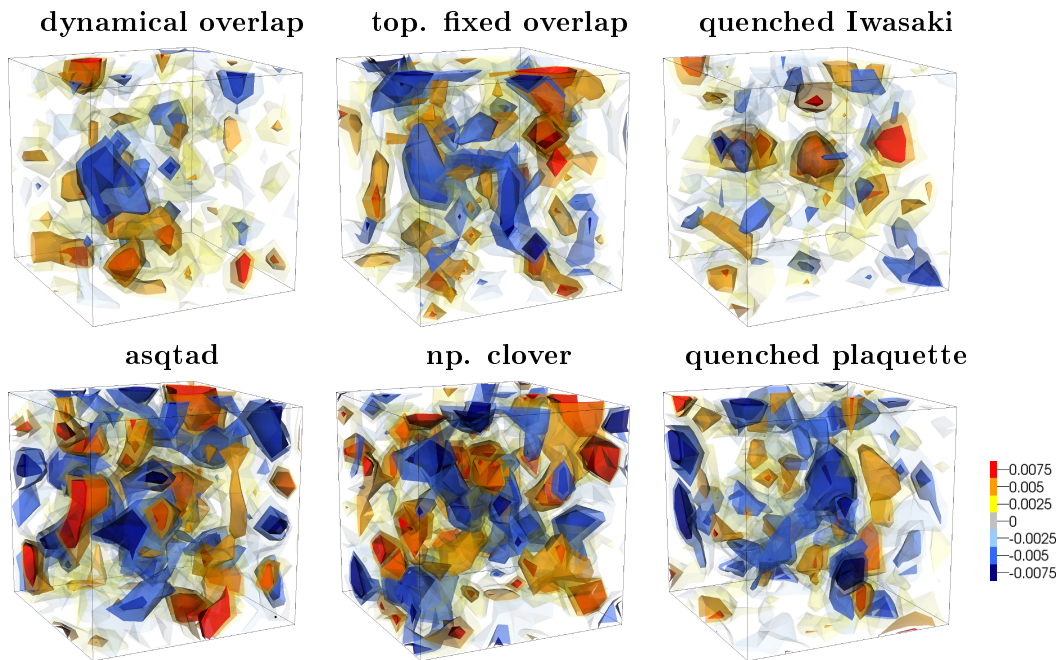
Fig. 7.1: Slices of the topological charge for dynamical overlap ($m_\pi = 600\,\text{MeV}$), asqtad staggered, dynamical overlap with topology fixing term ($m_\pi \approx 500\,\text{MeV}$ each) and nonperturbative improved clover (quite heavy $m_\pi \approx 1\,\text{GeV}$) fermions, all with the same lattice spacing $a = 0.12$ fm. The quenched counterparts of the latter two simulation algorithms are also depicted (Iwasaki $\leftrightarrow$ top. fixed overlap and plaquette $\leftrightarrow$ clover). The physical volume is $(1.44\,\text{fm})^3$ in all cases. The color scale is equal in all plots: Blue represents negative topological charge and red positive charge (cf. Ref. [1]).

spacing.

In Fig. 7.1 we show the topological structure of one sample configuration for different fermion actions after 5 steps of improved stout smearing. They all have the same lattice spacing of $a = 0.12$ fm and the same physical volume $V = (1.44\,\text{fm})^3$. The pion mass was around $500\,\text{MeV}$ except for the nonperturbative clover action, where it was around $1\,\text{GeV}$. The latter configurations have not been used in any of the quantitative analyses, because we expect big finite size effects for such heavy pion masses and small spatial volumes. In order to match the spatial volumes, we had to cut out a box of the corresponding size. Hence, we do not observe structures which extend over the periodic boundaries.

For comparison we have included samples of the topological profiles for the quenched ensembles in that figure. The plaquette and the Iwasaki gauge action have been used for the gauge action in the dynamical simulations with nonperturbative clover and the topology fixed overlap fermions, respectively. In accordance, they can be taken as the quenched counterparts to these dynamical simulations.
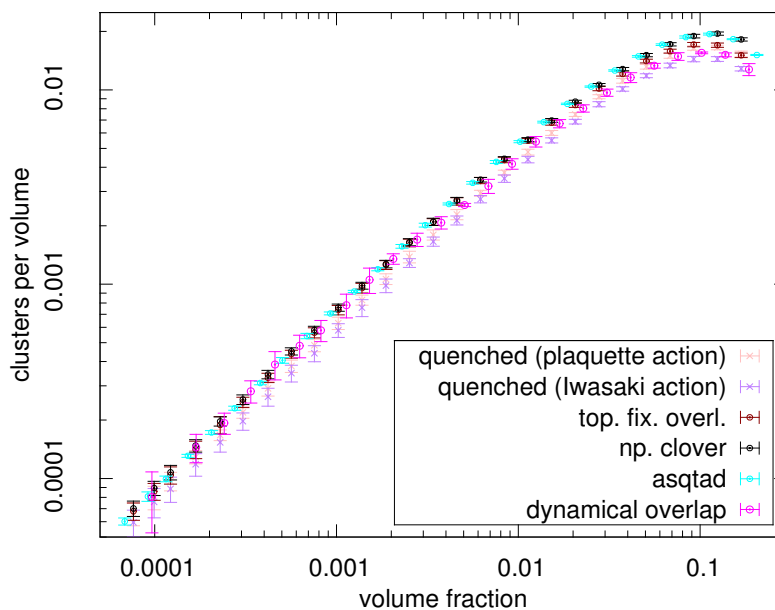
Fig. 7.2: The number of clusters per lattice volume as a function of the volume fraction above the cut-off, for the actions used in Fig. 7.1. Fitting a power law yields an exponent of ~0.85.

While we can only show a small fraction of the total four-dimensional volume, we see some of the main properties analyzed in detail below. Dynamical lattice simulations tend to give larger fluctuations of the topological charge density than quenched ones, as already pointed out in, e.g., Refs. [2, 142] (see also Chap. 5). This can be explained if we take into account that the gauge coupling g changes in dynamical simulations. In order to simulate at the same lattice spacing, we need a larger coupling constant and, hence, $\beta \sim 1/g^2$ decreases. As β enters the probability distribution of the gauge fields ($P[U] \propto e^{-\beta S[U]}$), larger fluctuations are permitted.

This effect can only be observed if we compare quenched and dynamical counterparts at the same lattice spacing. The dynamical overlap fermions lie between two quenched results. Hence, the statement that dynamical configurations exhibit larger fluctuations [142] is only correct if the gauge action for the dynamical simulation is the same as for the quenched one (see also Chap. 5).

7.2.1. Topological clusters

A cluster analysis of the topological charge density is a powerful tool to characterize the profile of the structure (cf. Refs. [2, 137] and Chap. 5). A cluster is defined as a set of neighboring lattice points with the same sign of the topological charge density.

In Fig. 7.2 we show this power law for the actions used in the previous section. We find that the power laws agree very well and that the exponents are all compatible with
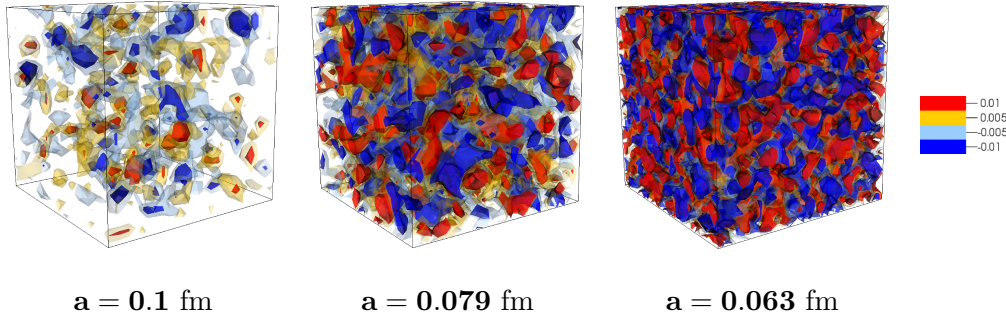
$\mathbf{a = 0.1}$ fm $\mathbf{a = 0.079}$ fm $\mathbf{a = 0.063}$ fm

Fig. 7.3: Three-dimensional slice of the topological charge density for twisted mass fermions at fixed physical volume $V = (1.9 \text{ fm})^3$ after 5 steps of improved stout smearing. We see an increasing laminar structure for finer lattices (cf. Ref. [1]).

each other. Therefore, the topological profiles are similar and the apparent difference in the three-dimensional visualizations in Fig. 7.1 originates from a difference in the absolute values of the densities.

7.3. Two point correlation function of the topological charge density

It is important to note that a qualitative comparison with visualizations is very limited. On the one hand, we are always restricted to lower dimensional cuts of the four dimensional volume, which do not capture all features of the structures. One should not over-interpret such results. On the other hand, we usually do not have configurations with the same lattice spacing and, aforementioned, the topological charge density scales with a^{-4}.

To stress the importance of the lattice constant a we show in Fig. 7.3 the topological charge density for different lattice spacings but fixed physical volume for twisted mass fermions. Two main effects in the continuum limit are clearly visible. First, the structure becomes more and more fine-grained and, second, the magnitude of the density in physical units increases.

We quantify the topological structures by the two-point correlation function of the topological charge density. To this end, we compute the "all-to-all" correlator of the density $\langle q(x)q(y)\rangle$ after 5 steps of improved stout smearing. The number of smearing steps and the filtering method is, in principle, ambiguous. Nevertheless, there are some good reasons for this choice. First, we need a "minimal" amount of smoothing to be able to apply the 3-loop improved field strength tensor in the field theoretic definition of the topological charge. Second, we do not want too much smearing, not to destroy the structure or to produce unwanted artifacts and, last but not least, we want to recall that the resulting density is very similar to the fermionic topological charge density [125]. Accordingly, we should find the same qualitative behavior for the two-point function as in Ref. [166]. The big advantage of the field theoretic definition is, that we can in
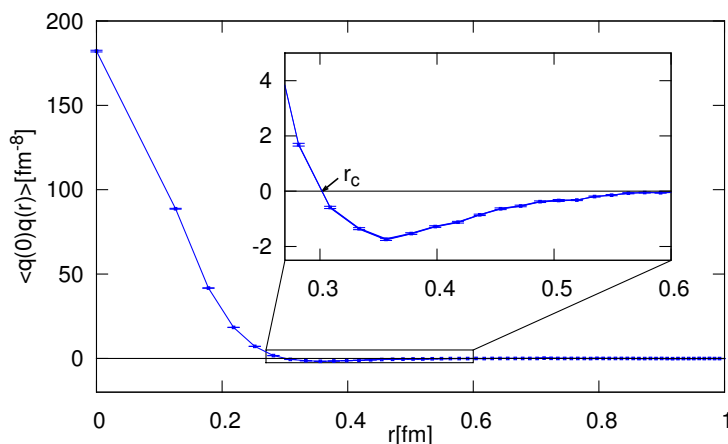
Fig. 7.4: Two-point function of the topological charge density after 5 improved stout smearing steps for an ensemble of dynamical overlap configurations (from Ref. [1]).

principle calculate the topological charge density for a lattice of arbitrary size. The fermionic definition is limited to very small lattices and, hence, not suited for studying the continuum limit at sufficiently large physical volumes.

We show an example of the correlator as a function of the distance $r = |x - y|$ between two lattice sites for the dynamical overlap ensemble in Fig. 7.4. At short distances the correlator develops a positive core of radius r_c, for large distances the correlator is compatible with zero and in between it is slightly negative [166]. This behavior is characteristic for all fermion actions and quenched ensembles [125].

7.3.1. Size of positive core

The radius of the positive core r_c is given by the (first) zero of the correlator. To this end, we interpolate the correlator between adjacent data points with a linear function. Although, there are many potential sources of errors, the position of this zero seems to be rather robust and has an excellent signal-to-noise ratio. We have also tried other than linear interpolations, e.g. spline fits, but they do not change the result significantly.

We measured the core size for the ensembles of Tab. 4.1 and plotted r_c in units of the lattice spacing versus the lattice spacing . Fig. 7.5 is the main result of this study from which we will primarily draw our conclusions on the relevance of chiral symmetry for topological properties (The errors result from an average over each ensemble). For the asqtad, nonperturbative clover and twisted mass action we had enough data to perform the limit $a \to 0$, while keeping the pion mass approximately constant.

In order to extrapolate to vanishing lattice spacing, we want to motivate the functional form of our fit. On the one hand, we expect errors which are independent of the action. These may result from the filtering method or the filtering strength. On the other hand there will be errors related to the action. As all actions are $\mathcal{O}(a)$-improved
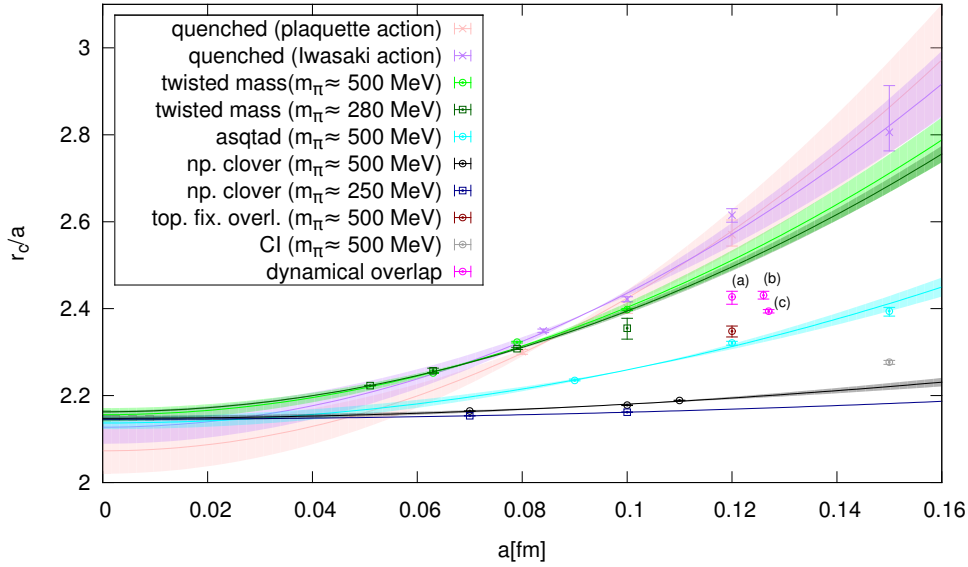
Fig. 7.5: Core size of the two-point function of the topological charge density. The errors − which are partly to small to be visible − result from the interpolation between the points of the correlator. We included fits and error bands for twisted mass, staggered and clover action. There are three different points from the overlap ensembles at different pion masses: (a) 600 MeV, (b) 560 MeV and (c) 510 MeV. Note that the twisted mass results for $m_\pi = 280$ MeV and 500 MeV nearly fall on top of one another (from Ref. [1]).

fermion action	m_π[MeV]	C	B[fm^{-2}]
twisted mass	≈ 500	2.16(2)	25(3)
twisted mass	≈ 280	2.163(2)	23.2(8)
np imp. clover	≈ 500	2.148(6)	3.2(6)
np imp. clover	≈ 250	2.146(-)	1.6(-)
asqtad staggered	≈ 500	2.14(1)	12(1)
quenched Iwasaki	-	2.13(5)	35(7)
quenched plaquette	-	2.07(4)	31(4)

Tab. 7.2: Parameters of the single fits. Only two lattice spacings were available for the light nonperturbative clover ensembles and, hence, no fit error can be given (from Ref. [1]).

the latter should only set in at $\mathcal{O}(a^2)$. This is why a function of the form

$$r_c/a = C + B \cdot a^2 \tag{7.1}$$

is fitted to the data.

We find indeed that the coefficients C are for all actions compatible with approximately $C = 2.15$ and that the B's differ, see Tab. 7.2. We did not fit higher-order
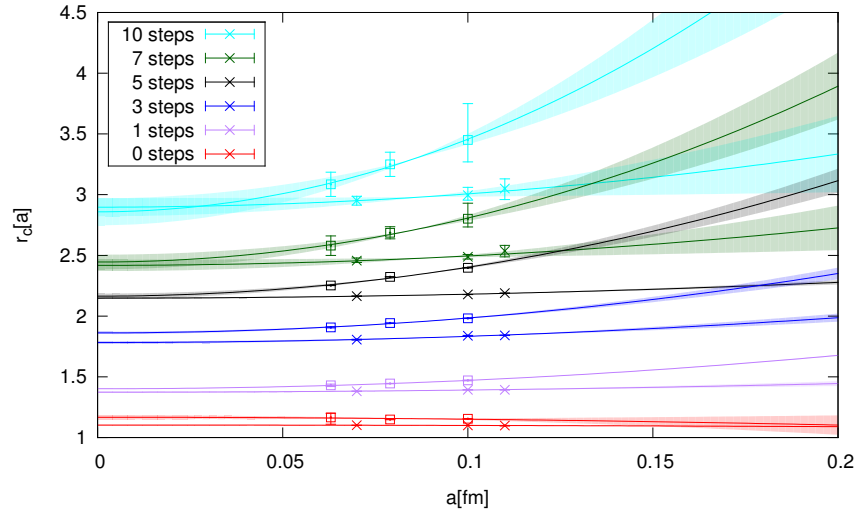
Fig. 7.6: Core size of the two-point function for different smearing steps for twisted mass (squares) and clover fermions (crosses) with $m_\pi = 500\,\text{MeV}$ after 0, 1, 3, 5, 7 and 10 smearing steps. The core size is roughly proportional to the square root of the step number $\sqrt{n_{\text{steps}}}$.

terms in the universal part, because our data points were not sufficient to do so and because we are only interested in the differences between the actions. We expected that actions with better chiral properties should give results which are markedly closer to the dynamical overlap ones than actions with strong violation of chiral symmetry.

We also included two quenched results for comparison. The extrapolations yield a consistent value for the constant C with a slightly larger error than for the dynamical configurations. The quenched results are in accordance with the results of Horváth *et al.* [166] who used the full fermionic definition of the topological charge density (not truncated in Dirac modes) and found a core size $r_c \approx 2a$ for the Iwasaki gauge action. Fig. 7.5 also includes the results for dynamical overlap fermions with and without topology fixing term at similar lattice spacings. There are three different points from the dynamical overlap configurations with different pion masses and lattice spacings. Due to the mass difference we cannot fit this data.

Let us further discuss the universality of this scaling behavior. First of all, if we compare the curves for twisted mass and clover fermions at $m_\pi \approx 500\,\text{MeV}$ and $m_\pi \approx 250\,\text{MeV}$, we find a relatively weak dependence on the mass. The ensembles with the lighter pion mass have smaller B factors, but within the errors the same constant term C. One reason for the smaller errors is that the negative dip increases with decreasing pion mass and, thus, we get a better signal for the core size. For a more detailed study of the mass dependence, we would need a set of configurations with smaller pion mass, which were not available from the ILDG at the time of this study.

Furthermore, we have found that the constant C depends on smearing. In Fig. 7.6 the data and fits for the twisted mass and the clover action at a pion mass of $m_\pi = 500\,\text{MeV}$
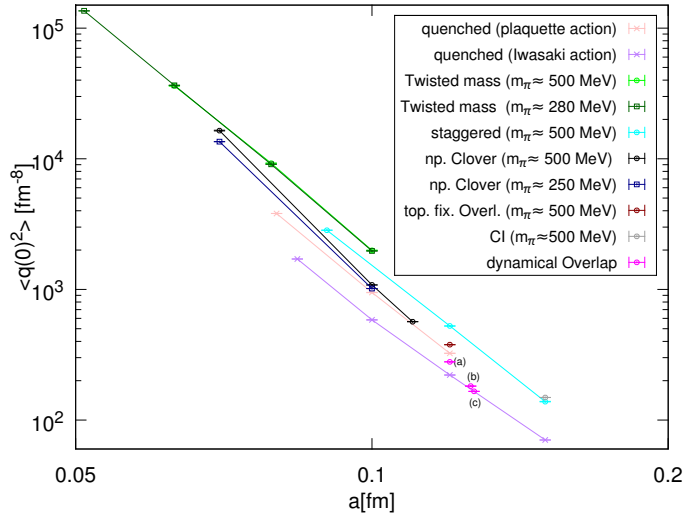
Fig. 7.7: Maxima of the two-point function of the topological charge density. The linear behavior in this double logarithmic plot indicates a divergence of the maximum for $a \to 0$. The dynamical overlap results are labeled according to the pion mass m_π as: (a) 600 MeV, (b) 560 MeV and (c) 510 MeV. Note that the twisted mass results for $m_\pi = 280$ MeV and 500 MeV fall on top of one another (from Ref. [1]).

after 0, 1, 3, 5, 7 and 10 smearing steps is shown. As one might expect, we find that the core size in lattice units grows with the number of smearing steps. The constant C is roughly proportional to the square root of the smearing steps $\sqrt{n_{\text{steps}}}$ (for $n_{\text{steps}} > 2$) and, hence, to the effective smearing radius [119, 139]. For more than 10 smearing steps no core size according to the above definition is found, as the negative part of the correlator vanishes.

The non-universal term Ba^2 measures how r_c/a from different actions converges towards C. The spread at current lattice spacings $a \leq 0.15$ fm is of the order of 10%. The overlap data lie in the middle of that range and even the quenched results are not far off. Our conclusion is that the different actions with different treatment of chiral symmetry do not differ much with respect to this important topological observable. Consequently, all of them can be used to study topological quantities. To the extent that topological properties are relevant for hadron properties, this observation also ties in with the fact that quite often the differences between quenched and dynamical results for these are not huge (typically of the order 10-30%).

7.3.2. Contact term

The two-point function has to develop a positive contact term in the continuum limit (see Sec. 3.3.3). Therefore, the mean-square value of the topological charge density $\langle q(0)^2 \rangle$ has to be divergent. Fig. 7.7 shows a double logarithmic plot of $\langle q(0)^2 \rangle$ in physical units versus the lattice spacing. The linear behavior indicates a power-like

divergence for $a \to 0$ for all actions:

$$\langle q(0)^2 \rangle \propto a^{-c} \tag{7.2}$$

for some positive number c.

This exponent is similar for the different actions and its value is around -6. Only the nonperturbative clover action deviates from this value with an exponent around -7.

As the contact term is highly divergent in the continuum limit, we do not expect the fitted values to agree and, thus, we do not present them here. There are also big differences in the absolute value of this maximum if one compares configurations at the same lattice spacing. These differences do not seem to have a systematic behavior and we have not found a good explanation for these differences.

The contact term of the dynamical ensembles is bigger than for their quenched counterparts, but it is also important to note that the contact term for dynamical overlap configurations at $a = 0.12$ fm lies between that for the two quenched simulations (plaquette and Iwasaki). This confirms the qualitative result of Fig. 7.1. Thus, we can conclude that dynamical fermions generate indeed larger fluctuations in the vacuum at finite lattice spacing, as argued in Ref. [3] and Ref. [142], if we compare dynamical configurations to their quenched counterparts. However, the differences between different actions can be as large as those between quenched and dynamical simulations.

Summarizing this study, we have investigated the topological charge density for state-of-the-art lattice actions with dynamical fermions and found that different fermion actions do generate different topological landscapes. This has been visualized in Fig. 7.1 and quantified through the topological charge correlator.

The change in the topological observables is not very large. The radius of the positive core of the topological correlator r_c approaches zero with the same slope C for all actions. In next-to-leading order r_c differs, but the spread is below 10% and even quenched simulations do not produce markedly different results. In particular, simulations with exact overlap fermions give results which are quite similar to those obtained with topology-fixed overlap fermions. The differences between quenched and dynamical simulations are not larger than those between different dynamical fermion actions. Also, the topological charge density seems to be little affected by changes in pion mass. In contrast, the effects for $\langle q(0)^2 \rangle$ are large but unsystematic.

These results are very sensitive to the lattice spacing a, implying that one should be very careful not to jump to conclusions when comparing topological properties of different configurations.

If we use our dynamical overlap results as benchmark for the quality of the other actions with respect to chirality, we have to conclude that all of them are reasonable successful and none of them seems to be clearly superior. The differences between results for dynamical overlap fermions and topology-fixed overlap fermions are especially small, as one might have expected.

8

QCD vacuum in external magnetic fields: zero and finite temperature

The effect of electromagnetic fields on hadronic matter is usually neglected in the context of Lattice QCD. The accessible fields are much smaller than the typical hadronic scales and only high-precision measurements can resolve their contribution to, e.g., hadron mass splittings.

There are, however, various physical systems where the electromagnetic fields are so strong that they generate physical effects. Prominent examples are cosmological models of the electroweak phase transition [167], magnetars [168] and non-central heavy ion collisions [169]. All these cases demand nonperturbative methods and, hence, they are best studied in Lattice QCD.

There is a fast increasing number of lattice studies related to the chiral magnetic effect [170, 171, 172], dressed Polyakov loops [173] or the QCD phase transition in an external magnetic field [174, 175, 176]. It has turned out in recent years that the finite temperature regime of Lattice QCD in external Abelian magnetic fields is very sensitive to the quark masses and the simulation parameters. The transition temperature, for example, increases for increasing external field if one uses heavy quarks, coarse lattices or unimproved fermion actions [174]. However, our group found a decreasing transition temperature for simulations with physical quark masses in the continuum limit [176].

In order to shed more light on these effects, we focus in this chapter on the impact of an external magnetic field on the QCD vacuum structure, in particular, the effect on the distribution of the gluonic fields and the topological charge density. To this end, we analyze results of a large-scale simulation at the physical quark mass for a wide range of temperatures, lattice spacings and lattice volumes.

As gluons do not carry electric charge, any effect of the magnetic field has to be mediated by quarks resulting in highly nonlinear effects. We find that the magnetic

field induces a highly significant anisotropy of the chromoelectric and chromomagnetic components of the gauge action which persists even above the phase transition. The change of gluonic part of the interaction measure in the external field, by contrast, is very sensitive to the transition and shows a behavior that is closely related to that of the quark condensates. Last but not least, the impact of the external field on topological structures is considered using the two-point correlation function of the topological density. It turns out that the effect of the magnetic field on these structures is only small.

In order to explain these results, we employ a one-loop Euler-Heisenberg action that accounts for both QED and QCD. The results of this calculation is in accordance with our numerical findings. It implies the correct tendency of the electric and magnetic components of the gluon field strength tensor. Furthermore, we find no contribution to the topological charge density on this one-loop level if there is no additional external electric field.

8.1. Excursus: finite temperature

Before we discuss how the external field is implemented, we want to introduce the notion of temperature. For this one has to go back to the continuum path integral (cf. Sec. 1.2), where an integration over an infinite time extent was assumed. At finite temperature T, this is replaced by an integration over a compact time direction with a time extent $\beta = \frac{1}{k_\mathrm{B}T}$ (this should not be confused with the gauge coupling)

$$\int_{-\infty}^{\infty} dx_4 \int d^3\mathbf{x} \to \int_0^{\beta} dx_4 \int d^3\mathbf{x}, \tag{8.1}$$

and the fermion fields in the path integral have to be anti-periodic in the time direction.

The discretization is done as usual (see Chap. 2). The main difference to the zero temperature case is the way one takes the continuum limit. For a temperature

$$T = \frac{1}{\beta} = \frac{1}{a \cdot N_t} \tag{8.2}$$

one has to to keep $a \cdot N_t$ fixed when sending $a \to 0$.

It is important to note that every lattice configuration has a certain temperature due to the limited temporal extent. In order to reduce temperature effects when analyzing single lattice spacings, one uses lattices with much larger temporal than spatial extent. These configurations will be referred as "zero temperature" configurations. For a comprehensive introduction to finite temperature Lattice QCD, we refer to Refs. [37, 177].

8.2. External magnetic field

Without loss of generality, we consider a constant external field in z-direction $\mathbf{b} = b_z = b\hat{e}_z$. The corresponding four-vector potential is not unique and one has to choose a

specific form. We use for simplicity

$$a_\mu(x) = (\mathbf{a}, a_4) = (0, b\,x, 0, 0). \tag{8.3}$$

In a finite box with periodic boundary conditions the magnetic flux perpendicular to the magnetic field is quantized [178, 179] according to

$$qbA = 2\pi N_b, \tag{8.4}$$

where q is the charge of the particle and A is the total area orthogonal to the field. This area is given on the lattice by $A = N_x N_y \cdot a^2$, so we can write the possible magnetic field strengths as:

$$qb = \frac{2\pi N_b}{N_x N_y \cdot a^2} \tag{8.5}$$

One can implement the above vector potential in a Lattice QCD simulation by multiplying all $SU(3)$-valued gauge links $U_\mu(n)$ at lattice site $n = (n_x, n_y, n_z, n_t)$ by a complex-phase $u_\mu(n) \in U(1)$:

$$u_\mu(n) = \begin{cases} e^{ia^2 qbn_x} & \text{if} \quad \mu = y, \\ e^{-ia^2 qbN_x n_y} & \text{if} \quad \mu = x \text{ and } n_x = N_x - 1, \\ 1 & \text{else.} \end{cases} \tag{8.6}$$

The first and the last line of this expression are straightforward to derive. The middle one corresponds to a twisted boundary condition, which is needed to restore the periodicity of the gauge fields. With this definition, every plaquette in the x-y plane is multiplied by $e^{ia^2 qb}$. From this one can see that $N_b = N_x N_y$, i.e. $a^2 qb = 2\pi$, is equivalent to no field. Hence, the magnetic field is bounded and due to the periodicity of the lattice one has $0 \le N_b \le N_x N_y/4$.

8.3. Details on the configurations

We used a large-scale simulation from Bali *et al.* [176, 180]. The configurations have been generated with a tree-level improved Symanzik gauge action and a stout smeared staggered fermion action [181]. The magnetic field has been implemented, as described in the previous section, by multiplying the smeared links with the complex phase from Eq. (8.6). The simulations cover a wide range of lattice spacings, volumes and temperatures. The quark masses in this $N_f = 2 + 1$ simulations are set to their physical values along the line of constant physics (LCP) which has been fixed by fixing the values f_K/m_π and f_K/m_K at their experimental values.[1]. The lattice spacing has been determined from f_K. This procedure is described in more detail in Ref. [182].

---

[1]This is achieved by tuning the bare mass parameters am_q

8.4. Induced anisotropy of the gluonic field strength

An external magnetic field alters the fermion determinant in the partition function and, accordingly, changes the weight of the gluonic field configurations. Symmetry considerations suggest that the magnetic field breaks the spatial symmetry (similar to finite temperature, which breaks the space-time symmetry in Euclidean space). Therefore, we expect an anisotropy of gluonic observables parallel and perpendicular to the magnetic field.

To check this, we measure the field strength tensor corresponding to our tree-level improved Symanzik action. The field strength tensor $F^a_{\mu\nu}$ contains information on the chromomagnetic and chromoelectric components of the gauge fields, which are defined in analogy to that of electromagnetism

$$F_{0i}(x) = F^a_{0i}(x)t^a = E^a_i(x)t^a \qquad \text{and} \qquad F_{ij}(x) = F^a_{ij}(x)t^a = \epsilon_{ijk}B^a_k(x)t^a. \qquad (8.7)$$

The QCD field strength tensor and its components are not gauge-invariant but the trace of the squared components is:

$$\text{tr}\{E^2_i\} = \tfrac{1}{2}(E^a_i)^2 \qquad \text{and} \qquad \text{tr}\{B^2_i\} = \tfrac{1}{2}(B^a_i)^2. \qquad (8.8)$$

These observables can be interpreted as the chromoelectric and chromomagnetic contributions to the gluonic action

$$S_G = \frac{1}{2g^2} \int d^4x \, \text{tr}\{\mathbf{E}^2(x) + \mathbf{B}^2(x)\}, \qquad (8.9)$$

where $\mathbf{E} = (E_x, E_y, E_z)$ and $\mathbf{B} = (B_x, B_y, B_z)$, respectively.

Due to space-time symmetry, one finds for zero temperature and zero external field that the expectation values of all individual components are equal. Finite temperature and external fields break this symmetry and induce an anisotropy of these components (temperature and magnetic field will induce different anisotropies).[2]

As a measure of the anisotropy, we use the differences of the components parallel to the external field ($E^2_\parallel = E^2_z$ and $B^2_\parallel = B^2_z$) and the average of the perpendicular components ($E^2_\perp = \tfrac{1}{2}(E^2_x + E^2_x)$ and $B^2_\perp = \tfrac{1}{2}(E^2_x + E^2_x)$) and subtract their values at zero external field (subscript 0)

$$\Delta_E = \left(\langle E^2_\perp \rangle - \langle E^2_\perp \rangle_0\right) - \left(\langle E^2_\parallel \rangle - \langle E^2_\parallel \rangle_0\right) \qquad (8.10)$$

and

$$\Delta_B = \left(\langle B^2_\perp \rangle - \langle B^2_\perp \rangle_0\right) - \left(\langle B^2_\parallel \rangle - \langle B^2_\parallel \rangle_0\right). \qquad (8.11)$$

The subtraction of the zero magnetic field result has two advantages. First, it removes the finite temperature contribution from the observable and, therefore, contains only the contribution due to the external field. Second, it cancels additive renormalization factors.

---

[2]First results of two-color QCD with unrooted staggered quarks [175] showed such an anisotropy for the plaquette, which corresponds to the simplest discretization of the field strength tensor.
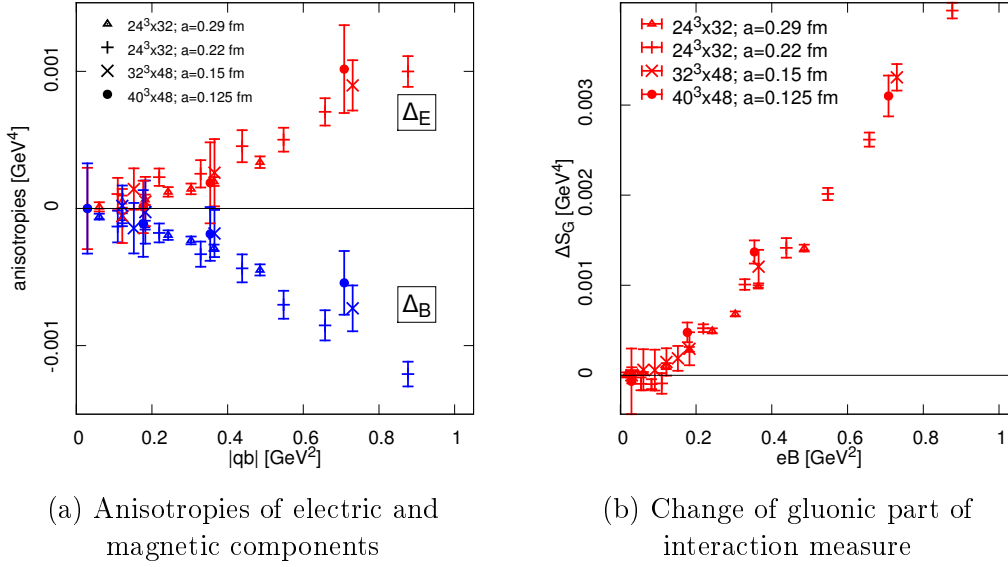
(a) Anisotropies of electric and
magnetic components

(b) Change of gluonic part of
interaction measure

Fig. 8.1: (a) Anisotropies of the chromomagnetic and chromoelectric components of the
action Δ_E and Δ_B (see Eq. (8.10) and Eq. (8.11)) as a function of the external
magnetic field $|qb|$ for different lattice spacings at $T = 0$. The electric component
parallel to the external field gets suppressed, while the magnetic component is
enhanced. (b) The gluonic part of the interaction measure $-\Delta I_G(b_{\mathrm{ext}})$ increases
in an external field at $T = 0$. Both quantities have a good scaling behavior, but
a precise extrapolation towards the continuum limit is not possible due to an
increasing error for decreasing lattice spacing (see text).

We are also interested the total change of the gluonic part of the interaction measure
with the external Abelian magnetic field b_{ext}:

$$- \Delta I_G(b_{\mathrm{ext}}) = -a \frac{\partial \beta}{\partial a} \big(S(b_{\mathrm{ext}}) - S(0)\big). \tag{8.12}$$

This quantity is the gluonic contribution to the trace anomaly. We determined the lat-
tice beta function $-a\frac{\partial \beta}{\partial a}$ nonperturbatively and measured the total Symanzik-improved
gauge action. In order to reduce the error from the subtraction of the zero external
field contribution, we had to fit the values for the smallest external fields to a constant,
a linear function and a cubic function and took the result with the best χ^2-value. The
differences between these fitting functions is, however, negligible and do not change the
final result.

8.4.1. $T = 0$

At zero temperature we use four different lattice spacings and external magnetic fields
up to $|qb| = 1\,\mathrm{GeV}^2$. The result can be found in Fig. 8.1. We find an anisotropy of
the parallel and perpendicular components which increases with the magnetic field as

expected from the above considerations. Moreover, an opposite effect for (chromo)magnetic and (chromo)electric components can be observed: While the magnetic component in the parallel direction gets enhanced, the electric component is suppressed for an increasing external field.

The anisotropy shows a good scaling behavior for different lattice spacings and we could not observe any finite volume effects (not shown). Nevertheless, it is not yet possible to reliably extrapolate to the continuum limit, as finer lattice spacings have larger errors. The reason for this behavior is the fact that we have to measure the difference of the action at zero and nonzero external field, which both grow as the lattice spacing decreases ($\propto 1/a^4$). As a consequence, it is not possible to constrain a fit sufficiently and more configurations, resulting in smaller statistical errors, are needed.

We further show the change of the gluonic part of the interaction measure in Fig. 8.1 and find that $-\Delta I_G$ increases with the external field. Again, we observe a good scaling of the results and an increasing error for smaller lattice spacings.

8.4.2. $T \neq 0$

Finite temperature results in an additional breaking of the symmetry between the magnetic and electric components of the field strength tensor. We find that the magnetic components are almost unchanged if one increases the temperature while the electric components strongly decrease when the phase transition is crossed. This is in accordance with the behavior of the gauge-invariant field strength correlator [183], for which such a behavior has been found first.

Our definition of the anisotropy does not account for this effect. It measures the difference of the parallel and perpendicular components induced by the magnetic field.

In Fig. 8.2 three different temperatures (114 MeV, 135 MeV and 163 MeV) for three lattice volumes each are presented. The anisotropy does not change across the phase transition, which for the chiral susceptibility occurs at around 150 MeV. Only the errors increase due to the finer lattice spacing (see above).

The interaction measure $-\Delta I_G$, however, shows a completely different picture. While it increases below the phase transition, it decreases above the transition and in the transition region we observe a rather non-monotonous behavior. This is very similar to the behavior of the quark condensates as observed in Refs. [176, 184].

8.5. Topological charge density in an external magnetic field

We have seen that the interaction measure is strongly affected by the external field. This raises the question if there is also an effect on the topological charge density $q(x)$.

The topological charge density, unlike the action density, is not strictly positive and the expectation value $\langle q(x) \rangle$ vanishes in the continuum limit and so it does for all its components. The anisotropy, as defined in the previous sections, is not applicable in this
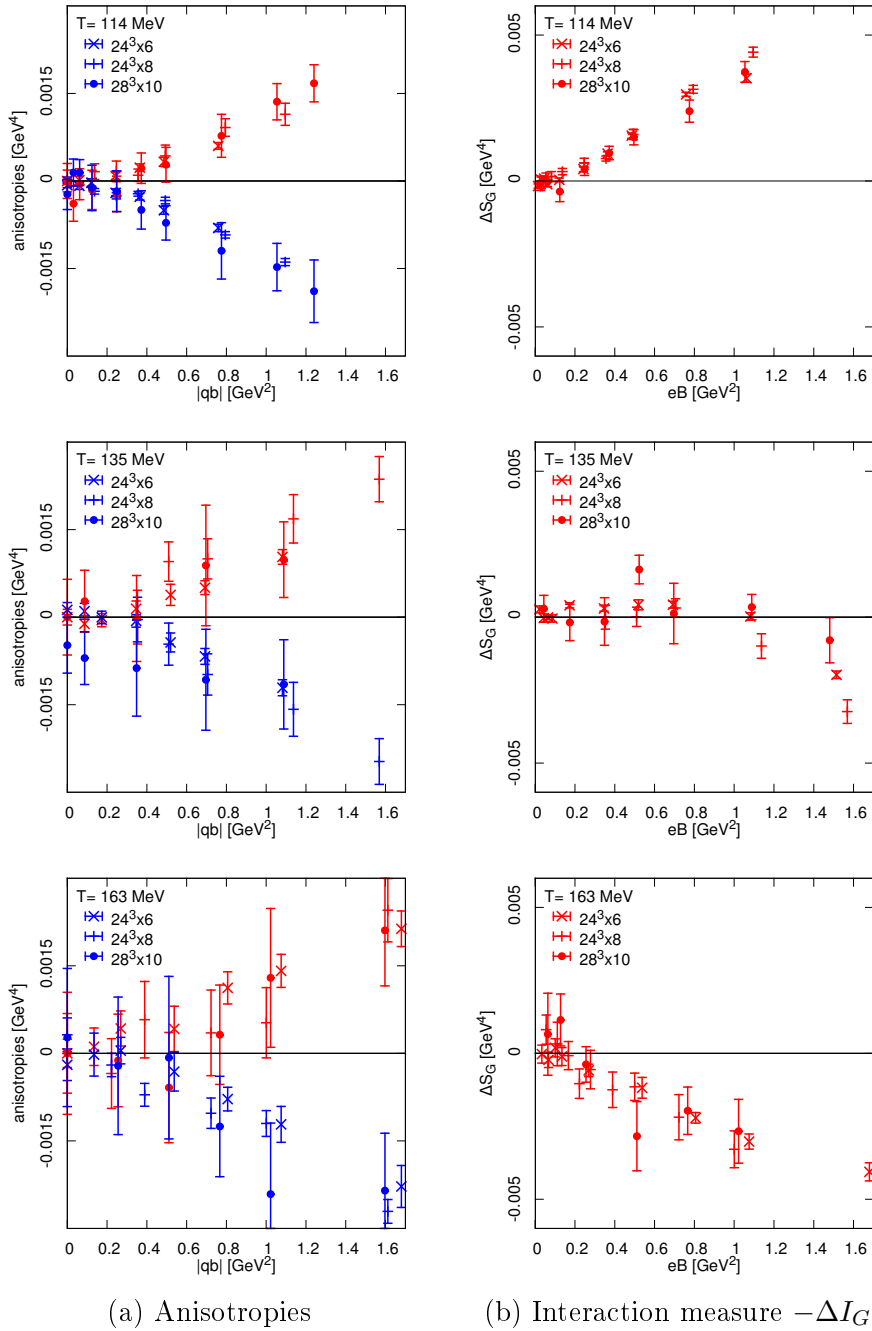
(a) Anisotropies   (b) Interaction measure $-\Delta I_G$

Fig. 8.2: Anisotropies Δ_E (red) and Δ_B (blue) and change of the gluonic part of the interaction measure $-\Delta I_G$ as a function of the external field $|qb|$ at three temperatures around the critical temperature. While the anisotropies do not change across the phase transition, one observes a drastic change for the gluonic part of the interaction measure. Its behavior is similar to that of the quark condensates as found in Ref. [184].
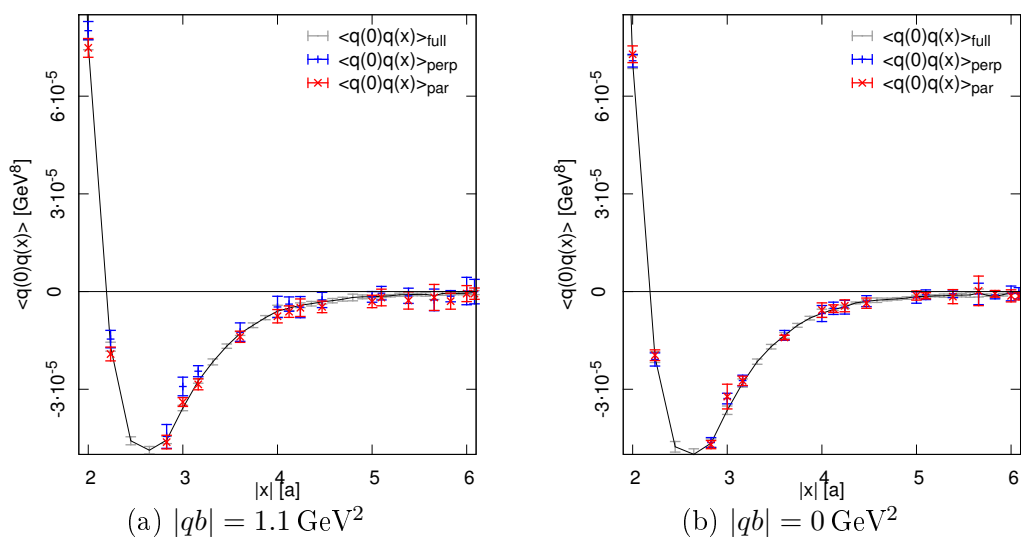
(a) $|qb| = 1.1 \, \mathrm{GeV}^2$ (b) $|qb| = 0 \, \mathrm{GeV}^2$

Fig. 8.3: The topological charge density correlator for the ensemble with the finest lattice spacing ($a = 0.099$ fm) at zero temperature and an external field of $\sim 1.1 \mathrm{GeV}^2$ and without external field. Splitting the correlator in contributions parallel and perpendicular to the external field shows no anisotropy and yields consistent results with the full correlator.

case and this is why we consider the two-point correlation function of the topological charge density $\langle q(0)q(x) \rangle$. This correlator carries information on the spatial form of the density.

In order to define a measure of anisotropy, we split the definition of the two-point function into a part where the vector x lies in the x-y plane ("perpendicular")

$$\langle q(0)q(x) \rangle_{\mathrm{perp}} \qquad \text{where} \qquad x \in \text{x-y plane} \tag{8.13}$$

and a part in the z-t plane ("parallel")

$$\langle q(0)q(x) \rangle_{\mathrm{par}} \qquad \text{where} \qquad x \in \text{z-t plane} \tag{8.14}$$

If there were any anisotropy in the distribution of the topological charge density, it would result in a difference between these correlators.

Before we measure the the topological charge density, Eq. (3.1) and the "all-to-all" correlation function, we apply 5 steps of improved stout smearing with the standard parameters (cf. previous chapters). In Fig. 8.3 the result for one ensemble with our finest lattice spacing ($a = 0.099$ fm) and an external field of around $1.1 \, \mathrm{GeV}^2$ is shown. The parallel correlator shows no deviation from the perpendicular one and both are compatible with the full two-point function (This observation has been made for all our configurations, but we show only the result for a single ensemble for reason of clarity.). In conclusion, there is no measurable deformation of the vacuum structure in the presence of an external field.

8.6. Euler-Heisenberg Lagrangian

In order to gain a quantitative understanding of the observed phenomena, we will employ a generalization of the QED Euler-Heisenberg action. QED and QCD degrees of freedom are distinguished by using capital letters for the QCD fields and small letters for the Abelian QED fields.

We start out with the Euclidean partition function in an external Abelian field

$$Z^{\text{ext}} = \int [\mathcal{D}\,\mathrm{A}_\mu][\mathcal{D}\,\bar\psi][\mathcal{D}\,\psi] \exp\left\{ -\int d^4x \left[\tfrac{1}{4}G_{\mu\nu}G_{\mu\nu} + \bar\psi(\slashed{D}^{\text{ext}}_\mu + m)\psi \right] \right\}, \qquad (8.15)$$

where $G_{\mu\nu}$ is the generalized field strength tensor consisting of the non-Abelian field strength tensor $F_{\mu\nu}$ and the Abelian one $f_{\mu\nu}$ (see below) and $D^{\text{ext}}_\mu = \partial_\mu + g\,\mathrm{A}_\mu + qa_\mu$ is the Dirac operator in the external $U(1)$ gauge field a_μ.

Integrating out the fermionic degrees of freedom yields an expression containing a functional determinant (cf. Eq. (2.64)) and hence the effective action

$$S_{\text{eff}} = \int d^4x \left[\tfrac{1}{4}G_{\mu\nu}G_{\mu\nu} + \ln\det(\slashed{D}^{\text{ext}} + m) \right]. \qquad (8.16)$$

The functional determinant can be expanded in powers of $(G/m^2)^n$ ($G^a_{\mu\nu}/m^2 \ll 1$ for all a, μ and ν) and according to Ref. [185], one gets the following renormalized effective action in an external field

$$S_{\text{eff}} = \frac{1}{32\pi^2} \int d^4x \,\mathrm{tr} \left\{ \frac{2}{3}g^2 G^2_{\mu\nu} \ln\left(\frac{M_R^2}{m^2}\right) + \frac{2}{45}g^3 G_{\mu\nu}G_{\nu\gamma}G_{\gamma\mu}\frac{1}{m^2} \right.$$
$$\left. + \frac{g^4}{18}\left[(G_{\mu\nu}G_{\mu\nu})^2 - \frac{7}{10}\{G_{\mu\alpha}, G_{\alpha\nu}\}_+^2 - \frac{29}{70}[G_{\mu\alpha}, G_{\alpha\nu}]_-^2 + \frac{8}{35}[G_{\mu\nu}, G_{\alpha\beta}]_-^2 \right]\frac{1}{m^4} \right\}. $$
$$(8.17)$$

The logarithm in this expression is the usual logarithm leading to charge renormalization and plays no role in our further discussion. We are only interested in those terms which are of fourth order in the fields, as those terms include the leading contribution to an effective coupling between Abelian and non-Abelian fields (photons and gluons).

Eq. (8.17) is very useful in this context, as one can easily use this expression for any gauge group. For pure QED, in particular, it agrees with the famous one-loop Euler-Heisenberg result [186]. In order to show this equivalence, we replace $G_{\mu\nu}$ with the electromagnetic field strength tensor $f_{\mu\nu}$ and substitute $g = q$, where q is the charge of the particle. Furthermore, we omit the trace and all commutator terms, as we deal with an Abelian field strength tensor. The remaining fourth-order terms in Eq. (8.17) can be expressed in the electric and magnetic fields $\mathbf{e}$ and $\mathbf{b}$. A little algebra shows

$$(f_{\mu\nu}f_{\mu\nu})^2 = 4(\mathbf{e}^2 + \mathbf{b}^2)^2, \qquad (8.18)$$

$$\{f_{\mu\alpha}, f_{\alpha\nu}\}_+^2 = 8(\mathbf{e}^2 + \mathbf{b}^2)^2 - 16(\mathbf{eb})^2. \qquad (8.19)$$

Therefore, one gets for the fourth-order effective action

$$S_{eff}^{(4)} = \frac{q^4}{576\pi^2 m^4} \int d^4x \left[(f_{\mu\nu}f_{\mu\nu})^2 - \tfrac{7}{10}\{f_{\mu\alpha}, f_{\alpha\nu}\}_+^2 \right]$$

$$= \frac{q^4}{576\pi^2 m^4} \int d^4x \left[4(\mathbf{e}^2 + \mathbf{b}^2)^2 - \tfrac{7}{10}(8(\mathbf{e}^2 + \mathbf{b}^2)^2 - 16(\mathbf{e}\cdot\mathbf{b})^2) \right]$$

$$= -\frac{q^4}{360\pi^2 m^4} \int d^4x \left[(\mathbf{e}^2 + \mathbf{b}^2)^2 - 7(\mathbf{e}\cdot\mathbf{b})^2 \right] = S_{\text{EH}}^{1-\text{loop}}. \qquad (8.20)$$

This is exactly the Euclidean 1-loop Euler-Heisenberg action for QED.

As a next step we want to derive a similar expression for the case of an interfering QED-QCD effective action. This is also included in Eq. (8.17) if we replace

$$gG_{\mu\nu} \to gF_{\mu\nu} + qf_{\mu\nu}. \qquad (8.21)$$

The substitution introduces at first sight terms $\propto f$ and $\propto f^3$, which are forbidden as they would violate $U(1)$ gauge-invariance. These terms would not appear if one did the derivation of Eq. (8.17) from scratch by evaluating the corresponding functional determinant as shown in Ref. [185]. For this reason we introduce selection rules and consider only the contributions $\propto f^2F^2$, $\propto f^4$ and $\propto F^4$. The latter two are the individual fourth-order Euler-Heisenberg terms for QED and QCD, respectively.

The expressions of fourth order in $G_{\mu\nu}$ can be derived by simple index manipulations and by keeping in mind that $[f, F] = 0$ and $\text{tr}_C\{ff[F, F]\} = ff\,\text{tr}_C\{[F, F]\} = 0$:

$$\text{tr}(G_{\mu\nu}G_{\mu\nu})^2 = \text{tr}\{(F_{\mu\nu}F_{\mu\nu})^2 + (f_{\mu\nu}f_{\mu\nu})^2 + 4(f_{\mu\nu}F_{\mu\nu})^2 + 2f_{\mu\nu}f_{\mu\nu}F_{\alpha\beta}F_{\alpha\beta}\} \quad (8.22)$$

$$\text{tr}\{G_{\mu\alpha}, G_{\alpha\nu}\}_+^2 = 4\,\text{tr}\{(F_{\mu\alpha}F_{\alpha\nu})^2 + (f_{\mu\alpha}f_{\alpha\nu})^2 + 4(f_{\mu\alpha}F_{\alpha\nu})^2$$
$$+ 2(f_{\mu\alpha}f_{\alpha\nu})(F_{\mu\alpha}F_{\alpha\nu})\} - 2\,\text{tr}\{F_{\mu\alpha}F_{\alpha\nu}[F_{\mu\beta}, F_{\beta\nu}]_-\} \quad (8.23)$$

$$\text{tr}[G_{\mu\alpha}, G_{\alpha\nu}]_-^2 = 2\,\text{tr}\{G_{\mu\alpha}G_{\alpha\nu}[G_{\mu\alpha}, G_{\alpha\nu}]_-\} = 2\,\text{tr}\{F_{\mu\alpha}F_{\alpha\nu}[F_{\mu\beta}, F_{\beta\nu}]_-\} \quad (8.24)$$

$$\text{tr}[G_{\mu\nu}, G_{\alpha\beta}]_-^2 = 2\,\text{tr}\{G_{\mu\nu}G_{\alpha\beta}[G_{\mu\nu}, G_{\alpha\beta}]_-\} = 2\,\text{tr}\{F_{\mu\nu}F_{\alpha\beta}[F_{\mu\nu}, F_{\alpha\beta}]_-\}. \quad (8.25)$$

We are only interested in the interference terms, which contain both f and F. This leads to the one loop-effective action

$$S_{QECD}^{(4)} = \frac{q^2 g^2}{576\pi^2 m^4} \int d^4x\,\text{tr}\left\{ 4(f_{\mu\nu}F_{\mu\nu})^2 + 2(f_{\mu\nu}f_{\mu\nu})(F_{\alpha\beta}F_{\alpha\beta}) \right.$$

$$\left. - \frac{7\cdot 4}{10} \left[4(f_{\mu\alpha}F_{\alpha\nu})^2 + 2(f_{\mu\alpha}f_{\alpha\nu})(F_{\mu\beta}F_{\beta\nu}) \right] \right\}. \quad (8.26)$$

Of course, this can be rewritten in terms of the fields $\mathbf{E}, \mathbf{B}, \mathbf{e}$ and $\mathbf{b}$ using identities analogous to Eq. (8.18) and Eq. (8.19) yielding

$$S_{QECD}^{(4)} = -\frac{q^2 g^2}{180\pi^2 m^4} \int d^4x\,\text{tr}\left\{ (\mathbf{e}^2 + \mathbf{b}^2)(\mathbf{E}^2 + \mathbf{B}^2) + 2(\mathbf{e}\mathbf{E} + \mathbf{b}\mathbf{B})^2 \right.$$

$$\left. - \tfrac{7}{2}(\mathbf{e}\mathbf{B} + \mathbf{b}\mathbf{E})^2 - 7(\mathbf{e}\mathbf{b})(\mathbf{E}\mathbf{B}) \right\}. \quad (8.27)$$

This is the mixing part of the 1-loop Euler-Heisenberg action of QED and QCD expressed in terms of (chromo)electric and (chromo)magnetic fields.

In our simulation we specified the external field according to $\mathbf{e} = 0$ and $\mathbf{b} = b \cdot \hat{e}_z$. Furthermore, one can split the chromoelectromagnetic fields in components that are parallel or perpendicular to the external field:

$$\mathbf{bE} = bE_\parallel, \quad \mathbf{bB} = bB_\parallel, \quad \mathbf{B^2} = B_\parallel^2 + B_\perp^2 \quad \text{and} \quad \mathbf{E^2} = E_\parallel^2 + E_\perp^2. \tag{8.28}$$

Substituting these expressions in Eq. (8.27), we get for a single quark flavor

$$S_{QECD}^{(4)} = -\frac{q^2 g^2}{180\pi^2 m^4} b^2 \int d^4x \, \text{tr} \left\{ E_\perp^2 + B_\perp^2 + 3B_\parallel^2 - \frac{5}{2} E_\parallel^2 \right\}, \tag{8.29}$$

and finally for the complete effective action

$$S_{QECD}^{eff} = \frac{g^2}{32\pi^2} \int d^4x \, \text{tr} \left\{ \frac{4}{3} (E_\perp^2 + B_\perp^2 + E_\parallel^2 + B_\parallel^2) \ln \left(\frac{M_R^2}{m^2} \right) \right.$$
$$\left. - \frac{45}{2} \frac{q^2 b^2}{m^4} (E_\perp^2 + B_\perp^2 + 3B_\parallel^2 - \frac{5}{2} E_\parallel^2) \right\}. \tag{8.30}$$

From the form of the action one can immediately draw some conclusions for the chromoelectric and chromomagnetic components. If the external field b is increased, then $E_\perp^2$ and $B_\perp^2$ are decreased in the effective action and, consequently, their expectation values increase. Different coefficients for $B_\parallel^2$ and $E_\parallel^2$ lead to an anisotropy of the parallel components. The parallel chromomagnetic field is enhanced, while the parallel chromoelectric field is suppressed. This yields the correct tendency of Δ_E and Δ_B as measured in the lattice simulations, although these analytic results were derived under the assumption that $G \ll m^2$, which is certainly not the case for very strong magnetic fields.

Furthermore, the topological charge density $q(x) \propto \text{tr} \, \mathbf{EB}$ couples only to $\mathbf{eb}$. Other combinations are not allowed by CP-invariance.[3] A modification of the topological charge density with just an external magnetic field $\mathbf{b}$ and no external electric field, $\mathbf{e} = 0$ is not possible at this order in G/m^2. This is compatible with our numerical findings.

---

[3]$\text{tr} \, \mathbf{EB}$ and $\mathbf{eb}$ are both CP-odd.

9

Conclusion

This thesis is devoted to the topological structure of gauge fields as seen in Lattice QCD configurations. In our work we went beyond the quenched approximation and investigated the impact of dynamical fermions on the QCD vacuum. We studied how the topological structures depend on the lattice discretization including fermions with an exact chiral symmetry. We further analyzed the effect of an external (Abelian) magnetic field and finite temperature. The main results of this thesis are summarized as follows.

In order to control the ambiguities of the filtering methods used to extract topological excitations from lattice configurations, we performed a comparative study of the local topological structure resulting from APE smearing, stout smearing and Laplace filtering. An almost one-to-one correspondence of the topological charge densities for the two smearing methods has been found. As a consequence, they suffer from the same artifacts and an independent method like Laplace filtering is needed as a crosscheck. In accordance with the quenched $SU(2)$ results [137], a high correlation between the results from smearing and Laplace filtering has been found. This allows for a matching of their filtering parameters to obtain results with reduced ambiguities.

This matching of parameters was applied to the analysis of topological clusters revealed by various methods. We have analyzed the power-law behavior of topological charge clusters seen by the individual methods and common to both methods with parameters matched accordingly. This analysis shows clearly a larger exponent in the presence of dynamical quarks compared to its quenched counterpart, i.e., configurations with the same gauge action and the same lattice spacing. In order to interpret this observation, one can relate the cluster exponent to the exponent of the size distribution of topological objects in corresponding models $d(\rho) \sim \rho^\beta$. Our findings give a

larger coefficient β in the dynamical case, hence, very small topological objects become suppressed. Moreover, the total number of clusters for a constant total cluster volume is substantially higher for dynamical configurations. Thus, the topological structure of the vacuum is much more fragmented in the presence of fermions if one compares dynamical configurations with their quenched counterpart.

Next, we showed results for the topological structures in dynamical overlap configurations, which possess an exact chiral symmetry in contrast to other lattice discretizations. As such simulations are notoriously expensive and tend to have huge autocorrelations, we analyzed how the topological structures evolve in a Monte Carlo history. We concluded that enough independent configurations are available to obtain first physics results. The lattice size and spacing differ from that of state-of-the-art lattice simulations with cheaper actions, but one can use results for similar parameters as a benchmark for other actions.

We have investigated the topological charge density for various lattice actions with dynamical fermions, including these new dynamical overlap simulations. This quantity was chosen because of the intimate connection between topology and chiral symmetry. Different fermion actions do generate different topological landscapes which can be seen in visualizations of the topological densities and which has been quantified through the topological charge correlator. The change in the topological observables turns out to be not very large. The radius of the positive core of the topological correlator r_c approaches zero with the same slope C for all actions. In next-to-leading order r_c differs, but the spread is below 10% and even quenched simulations do not produce markedly different results. In particular, simulations with exact overlap fermions give results which are quite similar to those obtained with topology-fixed overlap fermions, which can be simulated at competitive lattice spacings and volumes. The differences between quenched and dynamical simulations are not larger than those between different dynamical fermion actions. Also, the topological charge density seems to be little affected by changes in pion mass. In contrast, the effects for $\langle q(0)^2 \rangle$ are large but unsystematic. These results are very sensitive to the lattice spacing a, implying that one should be very careful not to jump to conclusions when comparing topological properties of different configurations.

If we use our dynamical overlap results as benchmark for the quality of the other actions with respect to chirality we can conclude that all of them are reasonable successful and none of them seems to be clearly superior. The differences between results for dynamical overlap fermions and topology-fixed overlap fermions are especially small, as one might have expected.

Finally, we analyzed the response of gluonic observables of the QCD vacuum to an external (Abelian) magnetic field. As gluons do not carry electric charge, they are only affected through their coupling to quarks. We used lattice configurations with dynamical quarks at the physical quark mass and a wide range of lattice spacings, lattice volumes and external field strengths. We have found that the external field induces an anisotropy of the chromoelelectric and chromomagnetic fields which persists even above

the phase transition. Furthermore, the gluonic contribution to the trace anomaly has been found to depend on the external field. A completely different behavior below and above the phase transition has been observed. At low temperature the action increases with an increasing external field, but at high temperature it decreases. In the phase transition region it is non-monotonic. This behavior is very similar to that of the quark condensates and reflects the strong relation between the gluonic degrees of freedom and the fermionic condensates.

The topological charge density does not show an effect if we increase the external field. This was quantified by the topological charge density correlation function which can be split in components parallel and perpendicular to the external field.

In order to get a qualitative explanation of these observations we employed a one-loop Euler-Heisenberg action for QED and QCD together. This analysis shows that there is, on the one hand, no coupling of the external field to terms which contribute to the topological charge density and, on the other hand, that there is a asymmetric coupling to the electric and magnetic components of the gluon field strength tensor whose tendency is in accord with our numerical simulations.

In conclusion, we touched three different aspects of the topological structure in the QCD vacuum

- Technical aspect: We explored methods to extract the topological content of Lattice QCD configurations and showed ways to control the ambiguities of the filtering process.

- Practical aspect: We showed that the violation of chiral symmetry is not as harmful on observables related to topology as one might expect.

- Phenomenological aspect: We made a cluster analysis of the topological charge density, which can be used to test models of the QCD vacuum and and we provided input for the phenomenology of the QCD vacuum in the presence of an external magnetic field.

A
Appendix

A.1. Euclidean geometry

Lattice QCD is formulated in Euclidean space. To this end, an analytic continuation from the physical Minkowski space, called Wick rotation,has to be performed. In doing so, one replaces the time coordinate

$$x_0 \to ix_0 \equiv x_4. \tag{A.1}$$

Therefore, the metric is replaced by

$$g_{\mu\nu} \to \delta_{\mu\nu} = \text{diag}(1, 1, 1, 1) \tag{A.2}$$

and, accordingly, one does not have to distinguish between co- and contravariant indices. The scalar product of two four vectors is simply

$$a \cdot b = a_\mu b^\mu = a_\mu b_\mu = \sum_{\mu=1}^{4} a_\mu b_\mu. \tag{A.3}$$

The most important consequence of this Wick rotation is that the exponent in the path integral is replace by

$$iS_M \to -S_E. \tag{A.4}$$

Hence, it is possible to interpret the exponential factor in the path integral as a probability distribution and one can apply importance sampling.

Euclidean correlation functions are completely different from those in Minkowski space and a continuation from Minkowski to Euclidean space (or vice versa) is in general

---

not possible. Under certain circumstances[1] one can obtain results which are valid in both spaces. This is, for instance, the case for the hadron mass spectrum.

A.2. Gamma matrices

The Euclidean gamma matrices are a set of matrices that obey the anticommutation relation

$$\{\gamma_\mu, \gamma_\nu\} = \gamma_\mu\gamma_\nu + \gamma_\nu\gamma_\mu = 2\delta_{\mu\nu}. \tag{A.5}$$

Depending on the physical problem, one can choose different representations of these matrices. We use the so-called *chiral representation*

$$\gamma_1 = \begin{pmatrix} 0 & -i\sigma_x \\ i\sigma_x & 0 \end{pmatrix} \gamma_2 = \begin{pmatrix} 0 & -i\sigma_y \\ i\sigma_y & 0 \end{pmatrix} \gamma_3 = \begin{pmatrix} 0 & -i\sigma_z \\ i\sigma_z & 0 \end{pmatrix} \gamma_4 = \begin{pmatrix} 0 & \mathbb{1} \\ \mathbb{1} & 0 \end{pmatrix} \tag{A.6}$$

These four matrices define a fifth matrix

$$\gamma_5 = \gamma_1\gamma_2\gamma_3\gamma_4 = \begin{pmatrix} \mathbb{1} & 0 \\ 0 & -\mathbb{1} \end{pmatrix}. \tag{A.7}$$

which anticommutes with each of the four gamma matrices. This matrix plays a central role for chiral symmetry in Chap. 1.

The anticommutation relation and respectively the γ-matrices define a special mathematical structure — a so-called *Clifford algebra* (sometimes Dirac algebra), which consists in four dimensions of 16 matricies

$$\Gamma^k \in \left\{ \mathbb{1}, \gamma_\mu, \gamma_5, \gamma_\mu\gamma_5, \sigma_{\mu\nu} = \frac{i}{2}[\gamma_\mu, \gamma_\nu] \right\} \tag{A.8}$$

which are linearly independent in the sense, that

$$\mathrm{tr}\{\Gamma_k, \Gamma_j\} = 4\delta_{ij}. \tag{A.9}$$

For for a short introduction, see e.g Ref. [15].

Furthermore, we want to introduce the Feynman slash notation for a contraction of a four vector with the gamma matrices:

$$\rlap{/}{a} \equiv \gamma_\mu a^\mu. \tag{A.10}$$

A.3. Grassmann algebra

In order to obey Fermi statistics one has to introduce a new type of variables for the fermion fields. These are the so called *Grassmann numbers*. Their main property is that two Grassmann numbers θ_i anticommute:

$$\theta_i\theta_j = -\theta_j\theta_i \tag{A.11}$$

---

[1] There are no poles of the correlation function in the first and the third sector of the complex plane of the time coordinate.

and hence

$$(\theta_i)^2 = 0. \tag{A.12}$$

Furthermore, Grassmann numbers commute with regular numbers $a \in \mathbb{C}$:

$$\theta_i a = a \theta_i \tag{A.13}$$

and any Taylor expansion of a function of Grassmann numbers

$$f(\{\theta_i\}) = c + c_i \theta_i + c_{ij} \theta_i \theta_j + \cdots + c_{ijk} \theta_i \theta_j \theta_k + \ldots \tag{A.14}$$

(with complex and completely antisymmetric coefficients $c, c_{ij} = -c_{ji}$) does not contain terms that are quadratic (or higher order) in any of the variables θ_i.

One can further specify the integration measure:

$$d^N \theta = d\theta_N d\theta_{N-1} \ldots d\theta_1 \,, \tag{A.15}$$
$$d\theta_i d\theta_j = -d\theta_j d\theta_i \,, \tag{A.16}$$
$$d\theta_i \theta_j = -\theta_j d\theta_i. \tag{A.17}$$

The integral over a Grassmann number is normalized

$$\int d\theta \, \theta = 1, \tag{A.18}$$

while the integral over a usual c-number vanishes

$$\int d\theta \, a = 0. \tag{A.19}$$

These rules are all ingredients to derive the master formulas for path integrals. Their derivation can be found in any introduction on Grassmann numbers and we just give the result. Let $\eta_j = (\theta_j + i\phi_j)/\sqrt{2}$ be complex Grassmann numbers and M_{mn} be a $N \times N$ matrix, then:

$$\int [d\eta^*][d\eta] \exp\left[-\sum_{i,j}^N \eta_i^* M_{ij} \eta_j \right] = \det M \tag{A.20}$$

and

$$\int [d\eta^*][d\eta] \, \eta_m \eta_n^* \exp\left[-\eta^\dagger M \eta \right] = M_{mn}^{-1} \det M. \tag{A.21}$$

To make contact to the fermion fields and Lattice QCD we have to take i as a multi index that contains space-time position, color and flavor. Hence, we have to make the following identification:

$$\eta_m \rightarrow \Psi_{x,\alpha,i} \qquad \text{and} \qquad \eta_n^* \rightarrow \bar{\Psi}_{y,\beta,j} \tag{A.22}$$

and for the matrix M_{mn}

$$M_{mn} \rightarrow D_{x,y,i,j}^{\alpha,\beta}. \tag{A.23}$$

A.4. Fujikawa Method

A very elegant way of deriving the chiral anomaly is the Fujikawa method [20, 21, 19]. This method is conceptually quite elaborate, but there are some very important lessons to learn about the relation of chiral symmetry, fermions and the gauge fields. The gist of this method is that the chiral anomaly arises from the non-invariance of the fermion measure. If we consider the Euclidean path integral

$$Z[\bar{\psi}, \psi, \mathrm{A}] = \int \mathcal{D}\psi\, \mathcal{D}\overline{\psi}\, \mathcal{D}\mathrm{A}\, e^{-(S_G[\mathrm{A}] + S_F[\bar{\psi}, \psi])}, \tag{A.24}$$

we immediately see that the integrand is invariant under chiral transformation $\psi \to e^{i\theta(x)\gamma_5}\psi\ \bar{\psi} \to \bar{\psi}e^{i\theta(x)\gamma_5}$. Accordingly, one gets for an infinitesimal transformation

$$S_F[\bar{\psi}, \psi] = \int d^4x \bar{\psi}(\not{D})\psi \to \int d^4x \bar{\psi}(\not{D})\psi + \theta(x)\partial_\mu\big(\underbrace{\bar{\psi}\gamma^\mu\gamma_5\bar{\psi}}_{\equiv J_5^\mu}\big). \tag{A.25}$$

The invariance of the action leads to the classical conservation law $\partial_\mu J_5^\mu = 0$, but in the path integral formalism one also has to transform the measure. This requires, however, some extra work. We first need a careful definition of the measure. To this end we expand the fields ψ and $\bar{\psi}$

$$\psi = \sum_i \phi_i a^i \qquad \text{and} \qquad \bar{\psi} = \sum_i \phi_i^\dagger b^i, \tag{A.26}$$

where $\{\phi_i\}$ is a complete set of c-number eigenfunctions of the Dirac operator

$$\not{D}\phi_i = \lambda_i \phi_i \tag{A.27}$$

and a_i, b_i are Grassmann-valued coefficients. An infinitesimal chiral transformation of ψ

$$\psi' = \sum_n a'_n \phi_n = \sum_n a_n \left(1 + i\theta(x)\gamma_5\right)\phi_n \tag{A.28}$$

yields the transformation of the coefficients

$$a'_m = \sum_n \left(\delta_{m,n} + i\theta(x)\phi_m^\dagger(x)\gamma_5\phi_n(x)\right)a_n. \tag{A.29}$$

The Jacobian of this transformation is then

$$\mathcal{J} = \det\left(\frac{\delta a}{\delta a'}\right) = \det\left(\mathbb{1} + i\int d^4x\theta(x)\sum_n \phi_n^\dagger(x)\gamma_5\phi_n(x)\right)\left[= \det\left(\frac{\delta b}{\delta b'}\right)\right], \quad \text{(A.30)}$$

which reduces with the aid of the well known matrix identity $\det(1+A) = \exp\{\mathrm{Tr}\log(1+A)\}$ and the expansion of the logarithm to

$$\mathcal{J} = \exp\left\{i\int d^4x\theta(x)\sum_n \phi_n^\dagger(x)\gamma_5\phi_n(x)\right\}. \tag{A.31}$$

The fermion measure transforms as follows

$$\mathcal{D}\,\bar{\psi}'\,\mathcal{D}\,\psi' = \prod_m da'_m db'_m = \mathcal{J}^{-2} \prod_m da_m db_m \tag{A.32}$$

$$= \exp\Big\{-2i\int d^4x\,\theta(x)\sum_n \phi_n^\dagger(x)\gamma_5\phi_n(x)\Big\}\mathcal{D}\,\bar{\psi}\,\mathcal{D}\,\psi. \tag{A.33}$$

The negative exponent of the Jacobian is a consequence of the Grassmann algebra. Before we evaluate the integral expression, we consider a global chiral transformation ($\theta(x) = \text{const}$). The remaining integral is entirely determined by the zero modes of the Dirac operator. Non-zero eigenvalues come in pairs $\{\lambda_n, -\lambda_n\}$ with the eigenfunctions $\{\phi_n, \gamma_5\phi_n\}$. Hermiticity of D then implies, that ϕ_n and $\gamma_5\phi_N$ are orthogonal and $\int d^4x\,\phi_n^\dagger\gamma_5\phi = 0$.

For zero modes we find $\gamma_5\phi_n = \pm\phi_n$, where the sign corresponds to the chirality of the eigenfunction and, hence,

$$\int d^4x \sum_n \phi_n^\dagger(x)\gamma_5\phi_n(x) = n_R - n_L \equiv -index(D), \tag{A.34}$$

where n_L and n_R denote the number of left- and right-handed zero modes, respectively.

For a local chiral transformation we have to do some additional work. The exponent of the Jacobian is ill-defined and has to be regularized. Fujikawa [20, 21, 19, 16] has chosen a covariant damping of high-frequency modes by the factor $e^{-(\lambda_n^2/M^2)}$.

$$\sum_n \phi_n^\dagger(x)\gamma_5\phi_n(x) = \lim_{M\to\infty}\sum_n \phi_n^\dagger(x)\gamma_5 e^{-(\lambda_n^2/M^2)}\phi_n(x). \tag{A.35}$$

This operator is well defined and allows to change the basis vectors $\{\phi_n(x)\}$ to plane-waves $\{e^{ikx}\}$:

$$\lim_{M\to\infty}\sum_n \phi_n^\dagger(x)\gamma_5 e^{-(\lambda_n^2/M^2)}\phi_n(x) \tag{A.36}$$

$$= \lim_{M\to\infty}\text{tr}\Big\{\int \frac{d^4k}{(2\pi)^4}e^{-ikx}\gamma_5 e^{-(\slashed{D}^2/M^2)}e^{ikx}\Big\} \tag{A.37}$$

$$= \lim_{M\to\infty}\text{tr}\Big\{\int \frac{d^4k}{(2\pi)^4}e^{-ikx}\gamma_5 \exp\Big\{\big(-D^\mu D_\mu - \frac{1}{4}[\gamma^\mu,\gamma^\nu]F_{\mu\nu}\big)/M^2\Big\}e^{ikx}\Big\}. \tag{A.38}$$

In the last line we used that $\slashed{D}^2 = D^\mu D_\mu + \frac{1}{4}[\gamma^\mu,\gamma^\nu]F_{\mu\nu}$. With $e^{-ikx}f(D_\mu)e^{ikx} = f(D_\mu + ik_\mu)$ one gets

$$(A.38) = \lim_{M\to\infty}\text{tr}\Big\{\int \frac{d^4k}{(2\pi)^4}\gamma_5 \exp\Big\{\frac{-1}{M^2}\Big((D_\mu + ik_\mu)^2 + \frac{1}{4}[\gamma^\mu,\gamma^\nu]F_{\mu\nu}\Big)\Big\}\Big\}$$

$$\overset{ik=M\cdot k'}{=} \lim_{M\to\infty}\text{tr}\Big\{M^4\cdot\int \frac{d^4k'}{(2\pi)^4}\gamma_5 \exp\Big\{-k'_\mu k'^\mu - \frac{2k'D}{M} - \frac{D^\mu D_\mu + \frac{1}{4}[\gamma^\mu,\gamma^\nu]F_{\mu\nu}}{M^2}\Big\}\Big\}$$

$$= \frac{1}{2!} \left(\frac{1}{4} \right)^2 \text{tr} \left\{ \gamma_5 [\gamma^\mu, \gamma^\nu][\gamma^\rho, \gamma^\sigma] F_{\mu\nu} F_{\rho\sigma} \right\} \underbrace{\int \frac{d^4 k}{(2\pi)^4} e^{-k^\mu k_\mu}}_{=1/16\pi^2} .$$

The last expression results from an expansion of the exponent in powers of $[\gamma^\mu, \gamma^\nu] F_{\mu\nu}$. Additionally, we drop all contributions in the expansion which are not $\propto 1/M^4$. Terms proportional to $1/M^\alpha$ for $\alpha > 4$ disappear for $M \to \infty$ and the other terms cancel due to γ-matrix identities. The final regularized expression reads[2]

$$\sum_n \phi_n^\dagger(x) \gamma_5 \phi_n(x) = -\frac{1}{32\pi^2} \epsilon^{\mu\nu\rho\sigma} \text{tr}\{F_{\mu\nu} F_{\rho\sigma}\} = -\frac{1}{16\pi^2} \text{tr}\{F_{\mu\nu} \tilde{F}^{\mu\nu}\} \tag{A.39}$$

This immediately leads to the well known anomaly of the axial current:

$$\partial_\mu J_5^\mu = -\frac{1}{8\pi^2} \text{tr}\{F_{\mu\nu} \tilde{F}^{\mu\nu}\}. \tag{A.40}$$

A.5. Computer programs

The following section is devoted to some of the programs and computer resources which have been used in this thesis. We gratefully acknowledge all contributors and hope that they continue improving their programs.

A.5.1. Chroma

The main results of this thesis were obtained using the *Chroma Software System for Lattice Field Theory* (short: Chroma) [187] which is designed as a portable, flexible and highly efficient Lattice QCD toolbox written in C++ with a high degree of object-orientation. Chroma is widely used in the Lattice QCD community and many different institution contribute to this project.

The software can be used in various ways. One can either take it as a black box and use predefined code or one can write own code modifying chroma. Both options have been used in this thesis. The quenched lattice configurations from Chap. 7 have been generated using built-in Chroma routines. For all other measurements, we used self-written code or customized existing code.

A.5.2. International Lattice Data Grid – ILDG

The numerical effort for Lattice QCD simulations has grown a lot in the last years, as we are aiming to larger volumes, smaller lattice spacings and lighter pion masses. We have already entered the era of peta-scale supercomputing and, tied to this, the costs for simulations have grown.

For this reason, the International Lattice Data Grid (ILDG) [188, 189, 190, 191] was founded. The ILDG is an international organization which offers tools and standards for

---

[2]Using $\gamma_5 \gamma^\mu \gamma^\nu \gamma^\rho \gamma^\sigma = -4\epsilon^{\mu\nu\rho\sigma}$
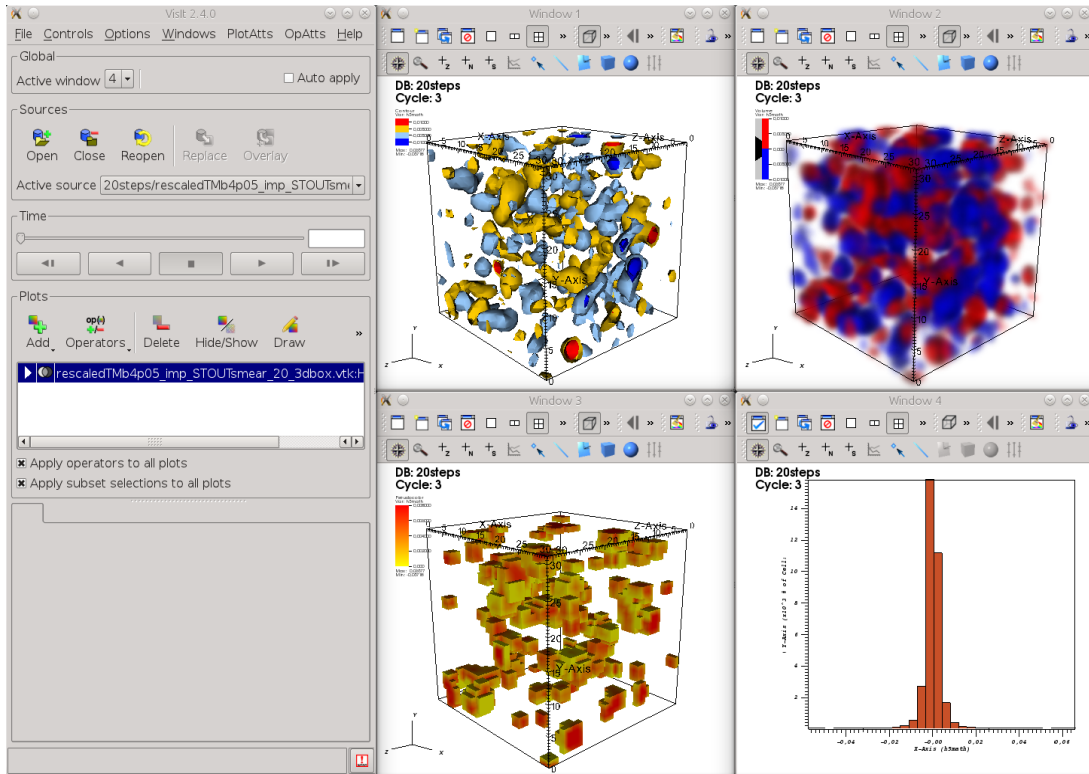
Fig. A.1: Example of the graphical user interface for a VisIt session. There are plenty of ways to visualize data, like volume and isosurface plots.

interchanging Lattice QCD data and providing access to the ensembles of local Grids. The members of the ILDG are the Australian CSSM, the European LDG, UKQCD from the United Kingdom, the American USQCD and the Japanese JLDG. They offer hundreds of state-of-the art lattice configurations from different actions, volumes and lattice spacings.

A.5.3. VisIt

VisIt [192] is a free, open source visualization tool, developed by the Department of Energy (DOE) Advanced Simulation and Computing Initiative (ASCI). It was designed to handle, visualize and analyze tera-scale data, but it can also be used with small-scale data from ordinary desktop computers.

The large functionality makes Visit a powerful tool. There are many capabilities to visualize data like isosurface, volume and vector field plots. Furthermore, two- and three-dimensional data are handled equally well and even animations of time series can be produced. There are also over twenty input formats and around ten output formats including *jpg, png* and *mpeg*. Visit also ships with many data analysis tools like threshold operations or histograms and due to an intuitive graphical user interface (see Fig. A.1) one can easily explore the data and apply the analysis tools on-the-fly.

This is the reason why we used VisIt to visualize the topological charge densities, for qualitative measurements and animations of filtering methods. For further reading, examples and frequently asked questions we recommend [193].

Bibliography

[1] F. Bruckmann, N. Cundy, F. Gruber, T. Lippert, and A. Schäfer, *Topology of dynamical lattice configurations including results from dynamical overlap fermions*, Phys.Lett. B707 (2012) 278–285, `arXiv:1107.0897`.

[2] F. Bruckmann, F. Gruber, and A. Schäfer, *Filtered topological structure of the QCD vacuum: Effects of dynamical quarks*, Phys. Lett. B687 (2010) 92–97, `arXiv:0910.4335`.

[3] F. Bruckmann, F. Gruber, K. Jansen, M. Marinkovic, C. Urbach, and M. Wagner, *Comparing topological charge definitions using topology fixing actions*, Eur.Phys.J. A43 (2010) 303–311, `arXiv:0905.2849`.

[4] F. Bruckmann, N. Cundy, F. Gruber, T. Lippert, and A. Schäfer, *Topology of dynamical lattice configurations including results from dynamical overlap fermions*, PoS LATTICE2011 (2011) 258, `arXiv:1111.2437`.

[5] F. Bruckmann, F. Gruber, and A. Schäfer, *Comparing the vacuum structure of quenched and dynamical configurations*, PoS LAT2009 (2009) 224, `arXiv:0910.5826`.

[6] F. Bruckmann, F. Gruber, C. B. Lang, M. Limmer, T. Maurer, A. Schäfer, and S. Solbrig, *Comparison of filtering methods in SU(3) lattice gauge theory*, PoS Confinement8 (2009) 045, `arXiv:0901.2286`.

[7] CMS Collaboration, S. Chatrchyan et al., *Observation of a new boson at a mass of 125 GeV with the CMS experiment at the LHC*, submitted to Phys.Lett.B `arXiv:1207.7235`.

[8] ATLAS Collaboration, G. Aad et al., *Observation of a new particle in the search for the Standard Model Higgs boson with the ATLAS detector at the LHC*, `arXiv:1207.7214`.

[9] ATLAS Collaboration, G. Aad et al., *Combined search for the Standard Model Higgs boson in pp collisions at $\sqrt{s} = 7\,TeV$ with the ATLAS detector*, `arXiv:1207.0319`.

[10] P. W. Higgs, *Broken Symmetries and the Masses of Gauge Bosons*, Phys.Rev.Lett. 13 (1964) 508–509.

[11] P. W. Higgs, *Broken symmetries, massless particles and gauge fields*, *Phys.Lett.* 12 (1964) 132–133.

[12] F. Englert and R. Brout, *Broken symmetry and the mass of gauge vector mesons*, *Phys. Rev. Lett.* 13 (1964) 321–323.

[13] G. S. Guralnik, C. R. Hagen, and T. W. B. Kibble, *Global conservation laws and massless particles*, *Phys. Rev. Lett.* 13 (1964) 585–587.

[14] Particle Data Group Collaboration, K. Nakamura et al., *Review of particle physics*, *J.Phys.G* G37 (2010) 075021.

[15] M. Kaku, *Quantum field theory: A Modern introduction*. Oxford Univ. Pr, New York, USA: Oxford Univ. Pr., 1993.

[16] M. E. Peskin and D. V. Schroeder, *An Introduction to quantum field theory*. Addison-Wesley, Reading, USA, 1995.

[17] F. Halzen and A. D. Martin, *Quarks and Leptons: An Introductory course in modern particle physics*. Wiley, 1984.

[18] C. Gattringer, *Quarks & Gluonen im Superrechner: Quantenchromodynamik auf dem Gitter*, *Phys. Unserer Zeit* 35 (2004) 227–233.

[19] K. Fujikawa and H. Suzuki, *Path integrals and quantum anomalies*. Clarendon Press, Oxford, UK: Clarendon, 2004.

[20] K. Fujikawa, *Path-Integral Measure for Gauge-Invariant Fermion Theories*, *Phys. Rev. Lett.* 42 (1979), no. 18 1195–1198.

[21] K. Fujikawa, *Path Integral for Gauge Theories with Fermions*, *Phys. Rev.* D21 (1980) 2848.

[22] M. F. Atiyah and I. M. Singer, *The Index of elliptic operators. 4*, *Annals Math.* 93 (1971) 119–138.

[23] G. 't Hooft, *Monopoles, instantons and confinement*, `hep-th/0010225`.

[24] F. Bruckmann, *Topological objects in QCD*, *Eur. Phys. J. ST* 152 (2007) 61–88, `arXiv:0706.2269`.

[25] A. A. Belavin et al., *Pseudoparticle solutions of the Yang-Mills equations*, *Phys. Lett.* B59 (1975) 85–87.

[26] G. 't Hooft, *Computation of the quantum effects due to a four- dimensional pseudoparticle*, *Phys. Rev.* D14 (1976) 3432–3450.

[27] D. Diakonov, *Chiral-symmetry breaking by instantons*, `hep-ph/9602375`.

[28] S. Vandoren and P. van Nieuwenhuizen, *Lectures on instantons*, `arXiv:0802.1862`.

[29] T. Banks and A. Casher, *Chiral Symmetry Breaking in Confining Theories*, *Nucl. Phys.* B169 (1980) 103.

[30] T. Schäfer and E. V. Shuryak, *Instantons in QCD, Rev. Mod. Phys.* 70 (1998) 323–426, `hep-ph/9610451`.

[31] D. Diakonov, *Instantons at work, Prog. Part. Nucl. Phys.* 51 (2003) 173–222, `hep-ph/0212026`.

[32] D. Diakonov and V. Y. Petrov, *Instanton Based Vacuum from Feynman Variational Principle*, *Nucl. Phys.* B245 (1984) 259.

[33] M. Creutz, *Quarks, Gluons and Lattices.* Cambridge Monographs on Mathematical Physics. Cambridge University Press, 1985.

[34] I. Montvay and G. Münster, *Quantum fields on a lattice.* University Press, Cambridge, UK, 1994.

[35] H. Rothe, *Lattice gauge theories: An Introduction*, *World Sci.Lect.Notes Phys.* 74 (2005) 1–605.

[36] T. DeGrand and C. DeTar, *Lattice Methods for Quantum Chromodynamics.* World Scientific, 2006.

[37] C. Gattringer and C. B. Lang, *Quantum chromodynamics on the lattice.* Springer, 2010.

[38] K. G. Wilson, *Confinement of Quarks, Phys. Rev.* D10 (1974) 2445–2459.

[39] F. Niedermayer, *Exact chiral symmetry, topological charge and related topics*, *Nucl. Phys. Proc. Suppl.* 73 (1999) 105–119, `hep-lat/9810026`.

[40] S. Chandrasekharan and U. J. Wiese, *An introduction to chiral symmetry on the lattice, Prog. Part. Nucl. Phys.* 53 (2004) 373–418, `hep-lat/0405024`.

[41] R. Gupta, *Introduction to lattice QCD, Lectures given at the LXVIII Les Houches Summer School* (1997) 83–219, `hep-lat/9807028`.

[42] K. Symanzik, *Continuum Limit and Improved Action in Lattice Theories. 1. Principles and φ^4-Theory*, *Nucl. Phys.* B226 (1983) 187.

[43] K. Symanzik, *Continuum Limit and Improved Action in Lattice Theories. 2. O(N) Nonlinear Sigma Model in Perturbation Theory*, *Nucl. Phys.* B226 (1983) 205.

[44] P. Weisz, *Continuum Limit Improved Lattice Action for Pure Yang-Mills Theory. 1.*, *Nucl.Phys.* B212 (1983) 1.

[45] P. Weisz and R. Wohlert, *Continuum Limit Improved Lattice Action for Pure Yang-Mills Theory. 2.*, Nucl.Phys. B236 (1984) 397.

[46] Y. Iwasaki, *Renormalization Group Analysis of Lattice Theories and Improved Lattice Action: Two-Dimensional Nonlinear O(N) Sigma Model*, Nucl.Phys. B258 (1985) 141–156.

[47] Y. Iwasaki, *Renormalization Group Analysis of Lattice Theories and Improved Lattice Action. II – four-dimensional non-abelian SU(N) gauge model*, `arXiv:1111.7054`.

[48] M. Lüscher and P. Weisz, *On-Shell Improved Lattice Gauge Theories*, Commun. Math. Phys. 97 (1985) 59.

[49] M. Lüscher and P. Weisz, *O(a) improvement of the axial current in lattice QCD to one loop order of perturbation theory*, Nucl.Phys. B479 (1996) 429–458, `hep-lat/9606016`.

[50] G. P. Lepage and P. B. Mackenzie, *On the viability of lattice perturbation theory*, Phys.Rev. D48 (1993) 2250–2264, `hep-lat/9209022`.

[51] G. P. Lepage, *Lattice QCD for Novices*, `hep-lat/0506036`.

[52] M. G. Alford, T. Klassen, and G. Lepage, *Improving lattice quark actions*, Nucl.Phys. B496 (1997) 377–407, `hep-lat/9611010`.

[53] H. B. Nielsen and M. Ninomiya, *No Go Theorem for Regularizing Chiral Fermions*, Phys. Lett. B105 (1981) 219.

[54] P. H. Ginsparg and K. G. Wilson, *A Remnant of Chiral Symmetry on the Lattice*, Phys. Rev. D25 (1982) 2649.

[55] M. Lüscher, *Exact chiral symmetry on the lattice and the Ginsparg-Wilson relation*, Phys. Lett. B428 (1998) 342–345, `hep-lat/9802011`.

[56] H. Neuberger, *Exactly massless quarks on the lattice*, Phys. Lett. B417 (1998) 141–144, `hep-lat/9707022`.

[57] H. Neuberger, *More about exactly massless quarks on the lattice*, Phys. Lett. B427 (1998) 353–355, `hep-lat/9801031`.

[58] B. Sheikholeslami and R. Wohlert, *Improved Continuum Limit Lattice Action for QCD with Wilson Fermions*, Nucl.Phys. B259 (1985) 572.

[59] M. Lüscher, S. Sint, R. Sommer, P. Weisz, and U. Wolff, *Nonperturbative O(a) improvement of lattice QCD*, Nucl.Phys. B491 (1997) 323–343, `hep-lat/9609035`.

[60] Alpha Collaboration, R. Frezzotti, P. A. Grassi, S. Sint, and P. Weisz, *Lattice QCD with a chirally twisted mass term*, *JHEP* 0108 (2001) 058, `hep-lat/0101001`.

[61] R. Frezzotti, P. A. Grassi, S. Sint, and P. Weisz, *A Local formulation of lattice QCD without unphysical fermion zero modes*, *Nucl.Phys.Proc.Suppl.* 83 (2000) 941–946, `hep-lat/9909003`.

[62] ALPHA Collaboration, R. Frezzotti, S. Sint, and P. Weisz, *O(a) improved twisted mass lattice QCD*, *JHEP* 0107 (2001) 048, `hep-lat/0104014`.

[63] R. Frezzotti and G. Rossi, *Chirally improving Wilson fermions. 1. O(a) improvement*, *JHEP* 0408 (2004) 007, `hep-lat/0306014`.

[64] J. B. Kogut and L. Susskind, *Hamiltonian Formulation of Wilson's Lattice Gauge Theories*, *Phys.Rev.* D11 (1975) 395.

[65] A. Bazavov, D. Toussaint, C. Bernard, J. Laiho, C. DeTar, et al., *Nonperturbative QCD simulations with 2+1 flavors of improved staggered quarks*, *Rev.Mod.Phys.* 82 (2010) 1349–1417, `arXiv:0903.3598`.

[66] M. Creutz, *Diseases with rooted staggered quarks*, *PoS* LAT2006 (2006) 208, `hep-lat/0608020`.

[67] C. Bernard, M. Golterman, and Y. Shamir, *Observations on staggered fermions at non-zero lattice spacing*, *Phys.Rev.* D73 (2006) 114511, `hep-lat/0604017`.

[68] C. Bernard, M. Golterman, and Y. Shamir, *Regularizing QCD with staggered fermions and the fourth root trick*, *PoS* LAT2006 (2006) 205, `hep-lat/0610003`.

[69] M. Creutz, *Chiral anomalies and rooted staggered fermions*, *Phys.Lett.* B649 (2007) 230–234, `hep-lat/0701018`.

[70] C. Bernard, M. Golterman, Y. Shamir, and S. R. Sharpe, *Comment on 'Chiral anomalies and rooted staggered fermions'*, *Phys.Lett.* B649 (2007) 235–240, `hep-lat/0603027`.

[71] M. Creutz, *Reply to: 'Comment on: 'Chiral anomalies and rooted staggered fermions'*, *Phys.Lett.* B649 (2007) 241–242, `arXiv:0704.2016`.

[72] M. Creutz, *Why rooting fails*, *PoS* LAT2007 (2007) 007, `arXiv:0708.1295`.

[73] M. Creutz, *The 't Hooft vertex revisited*, *Annals Phys.* 323 (2008) 2349–2365, `arXiv:0711.2640`.

[74] M. Creutz, *Comments on staggered fermions: Panel discussion*, *PoS* Confinement8 (2008) 016, `arXiv:0810.4526`.

[75] C. Bernard, M. Golterman, Y. Shamir, and S. R. Sharpe, *'t Hooft vertices, partial quenching, and rooted staggered QCD*, Phys.Rev. D77 (2008) 114504, `arXiv:0711.0696`.

[76] M. Creutz, *Comment on "'t Hooft vertices, partial quenching, and rooted staggered QCD"*, Phys.Rev. D78 (2008) 078501, `arXiv:0805.1350`.

[77] C. Bernard, M. Golterman, Y. Shamir, and S. R. Sharpe, *Reply to: 'Comment on: "t Hooft vertices, partial quenching, and rooted staggered QCD"*, Phys.Rev. D78 (2008) 078502, `arXiv:0808.2056`.

[78] C. Bernard, M. Golterman, and Y. Shamir, *Effective field theories for QCD with rooted staggered fermions*, Phys.Rev. D77 (2008) 074505, `arXiv:0712.2560`.

[79] C. Gattringer, I. Hip, and C. B. Lang, *Approximate Ginsparg-Wilson fermions: A first test*, Nucl. Phys. B597 (2001) 451–474, `hep-lat/0007042`.

[80] N. Metropolis, A. Rosenbluth, M. Rosenbluth, A. Teller, and E. Teller, *Equation of state calculations by fast computing machines*, J.Chem.Phys. 21 (1953) 1087–1092.

[81] S. Duane and J. B. Kogut, *Hybrid Stochastic Differential Equations Applied to Quantum Chromodynamics*, Phys.Rev.Lett. 55 (1985) 2774.

[82] S. Duane and J. Kogut, *The theory of hybrid stochastic algorithms*, Nucl.Phys. B275 (1986) 398.

[83] S. Duane, A. Kennedy, B. Pendleton, and D. Roweth, *Hybrid Monte Carlo*, Phys.Lett. B195 (1987) 216–222.

[84] S. O. Bilson-Thompson et al., *Highly-improved lattice field-strength tensor*, Ann. Phys. 304 (2003) 1–21, `hep-lat/0203008`.

[85] P. J. Moran, D. B. Leinweber, and J. Zhang, *Wilson mass dependence of the overlap topological charge density*, Phys.Lett. B695 (2011) 337–342, `arXiv:1007.0854`.

[86] P. J. Moran, D. B. Leinweber, and J. Zhang, *Role of the Wilson mass parameter in the overlap Dirac topological charge density*, PoS LAT2009 (2009) 076, `arXiv:0910.2780`.

[87] ALPHA Collaboration, S. Schaefer, R. Sommer, and F. Virotta, *Critical slowing down and error analysis in lattice QCD simulations*, Nucl.Phys. B845 (2011) 93–119, `arXiv:1009.5228`.

[88] S. Aoki et al., *Finite volume QCD at fixed topological charge*, Phys. Rev. D76 (2007) 054508, `arXiv:0707.0396`.

[89] R. Brower et al., *QCD at fixed topology*, *Phys. Lett.* B560 (2003) 64–74, `hep-lat/0302005`.

[90] H. Fukaya et al., *Topology conserving gauge action and the overlap-Dirac operator*, *Phys. Rev.* D73 (2006) 014503, `hep-lat/0510116`.

[91] W. Bietenholz et al., *Exploring topology conserving gauge actions for lattice QCD*, *JHEP* 03 (2006) 017, `hep-lat/0511016`.

[92] S. Shcheredin et al., *Testing a topology conserving gauge action in QCD*, *Nucl. Phys. Proc. Suppl.* 140 (2005) 779–781, `hep-lat/0409073`.

[93] JLQCD Collaboration, H. Fukaya et al., *Lattice gauge action suppressing near-zero modes of H(W)*, *Phys. Rev.* D74 (2006) 094505, `hep-lat/0607020`.

[94] E. Shintani, S. Aoki, H. Fukaya, S. Hashimoto, T. Kaneko, et al., *Strong coupling constant from vacuum polarization functions in three-flavor lattice QCD with dynamical overlap fermions*, *Phys.Rev.* D82 (2010) 074505, `arXiv:1002.0371`.

[95] JLQCD Collaboration, S. Aoki et al., *Two-flavor QCD simulation with exact chiral symmetry*, *Phys.Rev.* D78 (2008) 014508, `arXiv:0803.3197`.

[96] S. Borsanyi, Y. Delgado, S. Durr, Z. Fodor, S. Katz, et al., *QCD thermodynamics with dynamical overlap fermions*, `arXiv:1204.4089`.

[97] E. Witten, *Current Algebra Theorems for the U(1) Goldstone Boson*, *Nucl. Phys.* B156 (1979) 269.

[98] G. Veneziano, *U(1) Without Instantons*, *Nucl. Phys.* B159 (1979) 213–224.

[99] S. Durr et al., *Precision study of the SU(3) topological susceptibility in the continuum*, *JHEP* 04 (2007) 055, `hep-lat/0612021`.

[100] L. Del Debbio et al., *Topological susceptibility in the SU(3) gauge theory*, *Phys. Rev. Lett.* 94 (2005) 032003, `hep-th/0407052`.

[101] CP-PACS Collaboration, A. Ali Khan et al., *Topological Susceptibility in Lattice QCD with Two Flavors of Dynamical Quarks*, *Phys. Rev.* D64 (2001) 114501, `hep-lat/0106010`.

[102] UKQCD Collaboration, D. A. Smith and M. J. Teper, *Topological structure of the SU(3) vacuum*, *Phys. Rev.* D58 (1998) 014505, `hep-lat/9801008`.

[103] E. Seiler, *Some more remarks on the Witten-Veneziano formula for the eta-prime mass*, *Phys.Lett.* B525 (2002) 355–359, `hep-th/0111125`.

[104] E. Seiler and I. O. Stamatescu, *Some remarks on the Witten-Veneziano formula for the eta-prime mass*, .

[105] K. Osterwalder and R. Schrader, *Axioms for Euclidean Green's Functions*, *Commun.Math.Phys.* 31 (1973) 83–112.

[106] K. Osterwalder and R. Schrader, *Axioms for Euclidean Green's Functions. 2.*, *Commun.Math.Phys.* 42 (1975) 281.

[107] P. de Forcrand, *Localization properties of fermions and bosons*, *AIP Conf. Proc.* 892 (2007) 29–35, `hep-lat/0611034`.

[108] M. Teper, *Instantons in the Quantized SU(2) Vacuum: A Lattice Monte Carlo Investigation*, *Phys. Lett.* B162 (1985) 357.

[109] M. J. Teper, *Physics from the lattice: Glueballs in QCD, topology, SU(N) for all N*, `hep-lat/9711011`.

[110] M. Garcia Perez, A. Gonzalez-Arroyo, J. R. Snippe, and P. van Baal, *Instantons from over - improved cooling*, *Nucl.Phys.* B413 (1994) 535–552, `hep-lat/9309009`.

[111] F. Bruckmann, E. Ilgenfritz, B. Martemyanov, and P. van Baal, *Probing for instanton quarks with epsilon-cooling*, *Phys.Rev.* D70 (2004) 105013, `hep-lat/0408004`.

[112] M. Falcioni et al., *Again on SU(3) glueball mass*, *Nucl. Phys.* B251 (1985) 624–632.

[113] APE Collaboration, M. Albanese et al., *Glueball Masses and String Tension in Lattice QCD*, *Phys. Lett.* B192 (1987) 163.

[114] A. Hasenfratz and C. Nieter, *Instanton content of the SU(3) vacuum*, *Phys. Lett.* B439 (1998) 366–372, `hep-lat/9806026`.

[115] T. A. DeGrand et al., *Topological structure in the SU(2) vacuum*, *Nucl. Phys.* B505 (1997) 417–441, `hep-lat/9705009`.

[116] T. A. DeGrand et al., *Revealing topological structure in the SU(2) vacuum*, *Nucl. Phys.* B520 (1998) 301–322, `hep-lat/9711032`.

[117] C. Morningstar and M. J. Peardon, *Analytic smearing of SU(3) link variables in lattice QCD*, *Phys. Rev.* D69 (2004) 054501, `hep-lat/0311018`.

[118] M. Peardon, *QCD and Numerical Analysis III*, vol. 47 of *Lecture Notes in Computational Science and Engineering*, ch. Monte Carlo Simulations of Lattice QCD, pp. 41–54. Spriger, Berlin Heidelberg, 2005.

[119] C. W. Bernard and T. A. DeGrand, *Perturbation theory for fat-link fermion actions*, *Nucl. Phys. Proc. Suppl.* 83 (2000) 845–847, `hep-lat/9909083`.

[120] M. Lüscher, *Properties and uses of the Wilson flow in lattice QCD*, *JHEP* 1008 (2010) 071, `arXiv:1006.4518`.

[121] M. Lüscher, *Topology, the Wilson flow and the HMC algorithm*, *PoS* LATTICE2010 (2010) 015, `arXiv:1009.5877`.

[122] M. Lüscher, *Trivializing maps, the Wilson flow and the HMC algorithm*, *Commun.Math.Phys.* 293 (2010) 899–919, `arXiv:0907.5491`.

[123] S. Borsanyi, S. Durr, Z. Fodor, C. Hoelbling, S. D. Katz, et al., *High-precision scale setting in lattice QCD*, `arXiv:1203.4469`.

[124] P. J. Moran and D. B. Leinweber, *Over-Improved Stout-Link Smearing*, *Phys. Rev.* D77 (2008) 094501, `arXiv:0801.1165`.

[125] E.-M. Ilgenfritz et al., *Vacuum structure revealed by over-improved stout-link smearing compared with the overlap analysis for quenched QCD*, *Phys. Rev.* D77 (2008) 074502, `arXiv:0801.1725`.

[126] F. Bruckmann and E.-M. Ilgenfritz, *Laplacian modes probing gauge fields*, *Phys. Rev.* D72 (2005) 114502, `hep-lat/0509020`.

[127] F. Bruckmann and E.-M. Ilgenfritz, *Laplacian modes for calorons and as a filter*, *PoS* LAT2005 (2006) 305, `hep-lat/0509087`.

[128] F. Bruckmann and E.-M. Ilgenfritz, *Laplacian modes as a filter*, *Nucl. Phys. Proc. Suppl.* 153 (2006) 33–40, `hep-lat/0511030`.

[129] J. Greensite et al., *Localized eigenmodes of covariant Laplacians in the Yang-Mills vacuum*, *Phys. Rev.* D71 (2005) 114507, `hep-lat/0504008`.

[130] J. Greensite et al., *Localized eigenmodes of the covariant lattice Laplacian*, *PoS* LAT2005 (2006) 325, `hep-lat/0509070`.

[131] J. Greensite et al., *Eigenmodes of covariant Laplacian in SU(2) Yang-Mills vacuum: Higher representations*, *PoS* LAT2005 (2006) 326, `hep-lat/0510097`.

[132] C. Gattringer, *Testing the self-duality of topological lumps in SU(3) lattice gauge theory*, *Phys. Rev. Lett.* 88 (2002) 221601, `hep-lat/0202002`.

[133] C. Gattringer and S. Solbrig, *Remnant index theorem and low-lying eigenmodes for twisted mass fermions*, *Phys. Lett.* B621 (2005) 195–200, `hep-lat/0503004`.

[134] C. Gattringer and R. Pullirsch, *Topological lumps and Dirac zero modes in SU(3) lattice gauge theory on the torus*, *Phys. Rev.* D69 (2004) 094510, `hep-lat/0402008`.

[135] I. Horváth et al., *Low-dimensional long-range topological charge structure in the QCD vacuum*, *Phys. Rev.* D68 (2003) 114505, `hep-lat/0302009`.

[136] I. Horváth et al., *On the local structure of topological charge fluctuations in QCD*, *Phys. Rev.* D67 (2003) 011501, `hep-lat/0203027`.

[137] F. Bruckmann et al., *Quantitative comparison of filtering methods in lattice QCD*, *Eur. Phys. J.* A33 (2007) 333–338, `hep-lat/0612024`.

[138] C. Gattringer et al., *Hadron Spectroscopy with Dynamical Chirally Improved Fermions*, *Phys. Rev.* D79 (2009) 054501, `arXiv:0812.1681`.

[139] S. Capitani et al., *Rationale for UV-filtered clover fermions*, *JHEP* 11 (2006) 028, `hep-lat/0607006`.

[140] S. Solbrig, *Topology in SU(2) lattice gauge theory and parallelization of functional magnetic resonance imaging.* PhD thesis, Universität Regensburg, 2008.

[141] P. Buividovich, T. Kalaydzhyan, and M. Polikarpov, *Fractal dimension of the topological charge density distribution in SU(2) lattice gluodynamics*, `arXiv:1111.6733`.

[142] P. J. Moran and D. B. Leinweber, *Impact of Dynamical Fermions on QCD Vacuum Structure*, *Phys. Rev.* D78 (2008) 054506, `arXiv:0801.2016`.

[143] JLQCD Collaboration, S. Aoki et al., *Two-flavor QCD simulation with exact chiral symmetry*, *Phys. Rev.* D78 (2008) 014508, `arXiv:0803.3197`.

[144] Z. Fodor, S. D. Katz, and K. K. Szabo, *Dynamical overlap fermions, results with hybrid Monte- Carlo algorithm*, *JHEP* 08 (2004) 003, `hep-lat/0311010`.

[145] T. A. DeGrand and S. Schaefer, *Physics issues in simulations with dynamical overlap fermions*, *Phys. Rev.* D71 (2005) 034507, `hep-lat/0412005`.

[146] S. Schaefer and T. A. DeGrand, *Dynamical overlap fermions: Techniques and results. Simulations and physics results*, *PoS* LAT2005 (2006) 140, `hep-lat/0508025`.

[147] N. Cundy et al., *Numerical methods for the QCD overlap operator. IV: Hybrid Monte Carlo*, *Comput. Phys. Commun.* 180 (2009) 26–54, `hep-lat/0502007`.

[148] N. Cundy, S. Krieg, and T. Lippert, *Improving the dynamical overlap algorithm*, *PoS* LAT2005 (2006) 107, `hep-lat/0511044`.

[149] N. Cundy, *Current status of dynamical overlap project*, *Nucl. Phys. Proc. Suppl.* 153 (2006) 54–61, `hep-lat/0511047`.

[150] N. Cundy, S. Krieg, T. Lippert, and A. Schäfer, *Topological tunneling with Dynamical overlap fermions*, *Comput. Phys. Commun.* 180 (2009) 201–208, `arXiv:0803.0294`.

[151] N. Cundy, *Small Wilson Dirac operator eigenvector mixing in dynamical overlap hybrid Monte-Carlo*, *Comput. Phys. Commun.* 180 (2009) 180–191, `arXiv:0706.1971`.

[152] W. Bietenholz et al., *Tuning the strange quark mass in lattice simulations*, *Phys. Lett.* B690 (2010) 436–441, `arXiv:1003.1114`.

[153] S. Schaefer and F. Virotta, *Autocorrelations in Hybrid Monte Carlo Simulations*, *PoS* LATTICE2010 (2010) 042, `arXiv:1011.5151`.

[154] M. Creutz, T. Kimura, and T. Misumi, *Index Theorem and Overlap Formalism with Naive and Minimally Doubled Fermions*, *JHEP* 1012 (2010) 041, `arXiv:1011.0761`.

[155] HPQCD and UKQCD Collaboration, E. Follana, A. Hart, and C. Davies, *The Index theorem and universality properties of the low-lying eigenvalues of improved staggered quarks*, *Phys.Rev.Lett.* 93 (2004) 241601, `hep-lat/0406010`.

[156] J. Zhang, S. Bilson-Thompson, F. Bonnet, D. Leinweber, A. G. Williams, et al., *Numerical study of lattice index theorem using improved cooling and overlap fermions*, *Phys.Rev.* D65 (2002) 074510, `hep-lat/0111060`.

[157] K. Jansen, *Lattice QCD: A Critical status report*, *PoS* LATTICE2008 (2008) 010, `arXiv:0810.5634`.

[158] T. Maurer, T. Burch, L. Y. Glozman, C. Lang, D. Mohler, et al., *Axial charges of excited nucleons from CI-fermions*, `arXiv:1202.2834`.

[159] "International lattice data grid." http://ildg.sasr.edu.au.

[160] ETM Collaboration, R. Baron et al., *Light Meson Physics from Maximally Twisted Mass Lattice QCD*, *JHEP* 08 (2010) 097, `arXiv:0911.5061`.

[161] QCDSF Collaboration, M. Göckeler et al., *Determination of light and strange quark masses from full lattice QCD*, *Phys. Lett.* B639 (2006) 307–311, `hep-ph/0409312`.

[162] C. Bernard et al., *Status of the MILC light pseudoscalar meson project*, *PoS* LAT2007 (2007) 090, `arXiv:0710.1118`.

[163] S. Necco, *Universality and scaling behavior of RG gauge actions*, *Nucl.Phys.* B683 (2004) 137–167, `hep-lat/0309017`.

[164] S. Necco and R. Sommer, *The N(f) = 0 heavy quark potential from short to intermediate distances*, *Nucl.Phys.* B622 (2002) 328–346, `hep-lat/0108008`.

[165] N. Cundy, *Multi-grid HMC for Ginsparg-Wilson fermions*, *PoS* LAT2009 (2009) 030, `arXiv:0910.3878`.

[166] I. Horváth et al., *The negativity of the overlap-based topological charge density correlator in pure-glue QCD and the non-integrable nature of its contact part*, *Phys. Lett.* B617 (2005) 49–59, `hep-lat/0504005`.

[167] T. Vachaspati, *Magnetic fields from cosmological phase transitions*, *Physics Letters B* **265** (1991) 258–261.

[168] R. C. Duncan and C. Thompson, *Formation of very strongly magnetized neutron stars - Implications for gamma-ray bursts*, *Atrophys. J.* **392** (1992) L9–L13.

[169] V. Skokov, A. Y. Illarionov, and V. Toneev, *Estimate of the magnetic field strength in heavy-ion collisions*, *Int.J.Mod.Phys.* **A24** (2009) 5925–5932, `arXiv:0907.1396`.

[170] P. Buividovich, M. Chernodub, E. Luschevskaya, and M. Polikarpov, *Lattice QCD in strong magnetic fields*, `arXiv:0909.1808`.

[171] A. Yamamoto, *Lattice QCD simulation at finite chiral chemical potential*, *PoS* LATTICE2011 (2011) 220, `arXiv:1108.0937`.

[172] A. Yamamoto, *Lattice study of the chiral magnetic effect in a chirally imbalanced matter*, *Phys.Rev.* **D84** (2011) 114504, `arXiv:1111.4681`.

[173] F. Bruckmann and G. Endrodi, *Dressed Wilson loops as dual condensates in response to magnetic and electric fields*, *Phys.Rev.* **D84** (2011) 074506, `arXiv:1104.5664`.

[174] M. D'Elia, S. Mukherjee, and F. Sanfilippo, *QCD Phase Transition in a Strong Magnetic Background*, *Phys.Rev.* **D82** (2010) 051501, `arXiv:1005.5365`.

[175] E.-M. Ilgenfritz, M. Kalinowski, M. Muller-Preussker, B. Petersson, and A. Schreiber, *Two-color QCD with staggered fermions at finite temperature under the influence of a magnetic field*, `arXiv:1203.3360`.

[176] G. Bali, F. Bruckmann, G. Endrodi, Z. Fodor, S. Katz, et al., *The QCD phase diagram for external magnetic fields*, *JHEP* **1202** (2012) 044, `arXiv:1111.4956`.

[177] Z. Fodor and S. Katz, *The Phase diagram of quantum chromodynamics*, *SpringerMaterials - The Landolt-Börnstein Database* **23** (2010) `arXiv:0908.3341`.

[178] G. 't Hooft, *A property of electric and magnetic flux in non-abelian gauge theories*, *Nuclear Physics B* **153** (1979), no. 0 141 – 160.

[179] M. Al-Hashimi and U.-J. Wiese, *Discrete Accidental Symmetry for a Particle in a Constant Magnetic Field on a Torus*, *Annals Phys.* **324** (2009) 343–360, `arXiv:0807.0630`.

[180] G. Bali, F. Bruckmann, G. Endrodi, Z. Fodor, S. Katz, et al., *The finite temperature QCD transition in external magnetic fields*, `arXiv:1111.5155`.

[181] Y. Aoki, G. Endrodi, Z. Fodor, S. Katz, and K. Szabo, *The Order of the quantum chromodynamics transition predicted by the standard model of particle physics*, *Nature* **443** (2006) 675–678, `hep-lat/0611014`.

[182] S. Borsanyi, G. Endrodi, Z. Fodor, A. Jakovac, S. D. Katz, et al., *The QCD equation of state with dynamical quarks*, *JHEP* 1011 (2010) 077, `arXiv:1007.2580`.

[183] M. D'Elia, A. Di Giacomo, and E. Meggiolaro, *Gauge invariant field strength correlators in pure Yang-Mills and full QCD at finite temperature*, *Phys.Rev.* D67 (2003) 114504, `hep-lat/0205018`.

[184] G. Bali, F. Bruckmann, G. Endrodi, Z. Fodor, S. Katz, et al., *QCD quark condensate in external magnetic fields*, `arXiv:1206.4205`.

[185] V. Novikov, M. A. Shifman, A. Vainshtein, and V. I. Zakharov, *Calculations in External Fields in Quantum Chromodynamics. Technical Review*, *Fortsch.Phys.* 32 (1984) 585.

[186] W. Heisenberg and H. Euler, *Consequences of Dirac's theory of positrons*, *Z.Phys.* 98 (1936) 714–732, `physics/0605038`.

[187] SciDAC, LHPC and UKQCD Collaboration, R. G. Edwards and B. Joo, *The Chroma software system for lattice QCD*, *Nucl.Phys.Proc.Suppl.* 140 (2005) 832, `hep-lat/0409003`.

[188] M. G. Beckett, B. Joo, C. M. Maynard, D. Pleiter, O. Tatebe, et al., *Building the International Lattice Data Grid*, *Comput.Phys.Commun.* 182 (2011) 1208–1214, `arXiv:0910.1692`.

[189] P. Coddington, B. Joo, C. Maynard, D. Pleiter, and T. Yoshie, *Marking up lattice QCD configurations and ensembles*, *PoS* LAT2007 (2007) 048, `arXiv:0710.0230`.

[190] ILDG Middleware Working Group Collaboration, P. Coddington et al., *Towards an interoperable international lattice datagrid*, *PoS* LAT2007 (2007) 044, `arXiv:0711.4852`.

[191] T. Yoshie, *Making use of the International Lattice Data Grid*, *PoS* LATTICE2008 (2008) 019, `arXiv:0812.0849`.

[192] "Visit homepage." https://wci.llnl.gov/codes/visit/.

[193] "www.visitusers.org."

Acknowledgements

Zuerst will ich mich bei meinem Doktorvater Prof. Dr. Andreas Schäfer für seine hervorragende Betreuung bedanken. Es war vor allem sein Verdienst, dass ich stets die optimalen Rahmenbedingungen vorgefunden habe, um diese Dissertation anzufertigen.

Darüber hinaus danke ich allen Kollegen, mit denen ich in den letzten Jahren zusammenarbeiten durfte. Besonders hervorheben möchte ich dabei Dr. Falk Bruckmann, der mich seit meiner Diplomarbeit begleitet hat und dem ich so viel Wissen über das QCD Vakuum verdanke wie keinem Zweiten.

Um eine Dissertation fertig zu stellen, braucht man nicht nur Durchhaltevermögen und Disziplin, sondern auch ein tragfähiges soziales Umfeld. Darum danke ich Clemens Bauer, Melanie Pfeuffer, Simon Heybrock, Matthias Aicher und Jan Bundesmann, dass sie in jeder Phase dieser Arbeit ein offenes Ohr für mich gehabt haben und mich nach jedem Rückschlag wieder neu motivieren konnten, mein Bestes zu geben.

Ich danke meinen Eltern und meiner Familie, dass sie immer für mich da sind und mir stets den nötigen Halt im Leben geben. Das Gefühl von Sicherheit, das sie mir vermitteln, ist durch nichts zu ersetzten.

Der größte Dank gilt jedoch meiner Frau Johanna. Ihr Anteil an dieser Arbeit lässt sich nicht messen und ich weiß sicher, dass ich ohne ihre moralische Unterstützung nie so weit gekommen wäre. Ich bewundere die grenzenlose Geduld, die sie in den letzten Jahren aufgebracht hat und freue mich auf jeden Tag, den ich mit ihr verbringen darf.